Performance Parameters of Micromechanical Resonators

by

Lynn Khine

A dissertation submitted in partial fulfillment of the
requirements for the degree of

Doctor of Philosophy

Department of Electrical and Computer Engineering

National University of Singapore

Committee in charge:
Prof. Moorthi Palaniapan, Advisor
Prof. Francis Tay Eng Hock
Prof. Vincent Lee Chengkuo
Prof. Liwei Lin

Performance Parameters of Micromechanical Resonators

by

Lynn Khine

Abstract

Performance Parameters of Micromechanical Resonators

by

Lynn Khine

Doctor of Philosophy in Electrical Engineering, National University of Singapore

In this work, performance parameters of various flexural-mode and bulk-acoustic-mode micromechanical resonators are presented. Investigated parameters are quality factor (Q), pressure stability, power handling, nonlinearity, and temperature stability. Resonators studied in this work are electrostatically driven-and-sensed, and they are fabricated in SOIMUMPs process provided by MEMSCAP.

The bulk of this work has focused on the study of quality factor. Tested flexural-mode beam resonators can provide Q values in tens of thousands range, but much higher quality factors above one million have been measured for bulk-acoustic-mode resonators. One of the main vibration energy losses for bulk-mode resonators is the losses through the anchor support. The dependence of Q on structural geometry, as well as on the shape of anchor design, is explored in detail for Lamé-mode square resonators. Measured results suggest that T-shaped anchor design can improve the Q performance with lower motional resistance compared to straight-beam anchor for supporting bulk-mode resonators.

At pressure levels below 100Pa, the quality factor of bulk-mode resonators is measured to be relatively independent of pressure, which can be considered as the

threshold pressure. On the other hand for the beam resonators, this threshold pressure is roughly 10Pa. Given the same amount of air damping, bulk-mode resonators with orders of magnitude higher mechanical stiffness can uphold their maximum Q better at higher pressures compared to the beam resonators.

Bulk-mode resonators studied in this work are able to handle higher power levels before their vibrations become nonlinear compared to beam resonators, mainly due to orders of magnitude higher energy storage capability. High power handling of bulk-mode resonators is beneficial for oscillator implementation because the combined effect of ultra-high Q and high energy storage capacity can improve both close-to-carrier phase noise and the noise floor of the oscillator.

The resonant frequency notably drifts with temperature for silicon resonators. Large amount of resonant frequency shifts with temperature is useful for temperature sensing, but undesirable for frequency references. Hence, a temperature compensation method is required for resonator oscillators. A new idea of temperature compensation is demonstrated with experimental verifications in this work, which is based on frequency mixing of two oscillation signals, and this method has the potential to compensate the frequency shifts in bulk-mode resonators as well.

Keywords: Micromechanical resonators, flexural beam, bulk acoustic mode, extensional, Lamé-mode square, wine glass disk, oscillators, and temperature compensation

This thesis is dedicated to my loving parents.

Acknowledgements

Firstly, I would like to express my deep appreciation to my advisor Prof. Moorthi Palaniapan for his support, exemplary guidance and advice throughout my graduate studies at National University of Singapore (NUS). Without his keen insight and sincere encouragements, this thesis would not have been possible. I would also like to thank Prof. Wong Wai-Kin for his strong support and help with some technical details. In addition, I'm grateful to the dissertation Committee Members and honored for their valuable time, genuine inputs and advice they have given during the review process.

Many thanks to my colleagues at NUS: Shao Lichun, Wong Chee Leong and Niu Tianfang for their collaboration and fruitful discussions that helped progress my research. I'm thankful to the staff at Signal Processing & VLSI Laboratory, Center for Integrated Circuit Failure Analysis & Reliability (CICFAR), and PCB Fabrication Laboratory, especially Mr. Abdul Jalil bin Din and Mr. Teo Seow Miang, for their help with the tools and equipments necessary for measurement. Many thanks also go to MEMSCAP Inc. for device fabrication and to NUS for the financial support.

Last but not least, my special thanks go to my loving parents and sisters, and my wife for all of their love and support. My deepest gratitude goes to my father and my mother for their eternal love, for always believing in me, for their wisdom, and for helping me face tough challenges in life; this thesis is dedicated to them.

Table of Contents

List of Figures

List of Tables

Chapter 1

Introduction

MicroElectroMechanical Systems (MEMS) typically have interacting components that are assembled for diverse applications such as inertial sensors, mass sensors, charge sensors, microfluidics, oscillators and filters. Amongst the vast systems that are generally termed as MEMS, *micromechanical resonators* have been studied extensively. Given the current trend for miniaturization of components in communication systems, large demand is placed on high-performance devices with small size, potential for integration with CMOS electronics, and low-cost batch fabrication. Therefore, much research has been reported on the replacement of off-chip bulky components with IC-compatible micromechanical resonators.

Quartz crystals have long been used as resonators, which are still one of the best choices available. Quartz crystals at MHz range with quality factors (Q) in the order of 10^6 are widely used for oscillators. Besides having high Q, they also have good power handling and excellent temperature stability. For example, recently reported quartz crystal at 10MHz has a Q of 1.3 million [1]. Given their high-Q performance, crystal oscillators are well known to provide good phase noise. However, a major drawback for crystal resonators is that their fabrication process is not compatible with IC fabrication such as CMOS process.

Advances in *bulk micromachining* and *surface micromachining* technologies have enabled batch fabrication of a variety of single crystal silicon (SCS) resonators and polysilicon resonators with sub-micron capacitive transducer gaps. High quality factors provided by silicon resonators are catching up to that of bulky quartz crystals with Q values in millions [2, 3]. As the operating frequency is increased, the Q value of resonator normally comes down. Hence, the product of resonant frequency and quality factor ($f_o \times Q$) serves as a figure of merit when comparing different type of resonators. Given the ease of monolithic integration with CMOS electronics, along with good long-term stability, silicon is an attractive structural material for micromechanical resonators.

For transduction mechanism, *capacitive* drive-and-sense is considered very effective for micromechanical resonators since it could provide large vibrations without direct physical contact between the resonating proof-mass and the electrodes. If the resonator design is carefully optimized by reducing the vibration energy losses through anchor supports, high performance devices could be achieved for diverse applications.

1.1 What is a micromechanical resonator?

A micromechanical resonator is a mechanical structure equipped with some transduction mechanism that is capable of exciting the resonator to vibrate at its resonant frequency. The resonator is usually excited at its fundamental resonance mode. However, excitations at its higher-order modes are also possible. The resonant frequency is dependent on the type of structural material used for vibrating parts and on the geometric dimensions of the resonator. Piezoelectric materials such as quartz or lead zirconate titanate (PZT) could be used as an excitation source through piezoelectric actuation and sensing techniques. Although piezoelectric resonators have their advantages, their major drawback is the process limitation for integration with CMOS electronics, with the exception of AlN-based resonators. Furthermore, the drive and sense electrodes of piezoelectric resonators are in direct physical contact with the resonating body, resulting in higher energy loss and degradation in quality factor.

For a two-port capacitively driven-and-sensed resonator with parallel-plate electrodes, as shown in Figure 1.1, an electrostatic force is generated between the drive

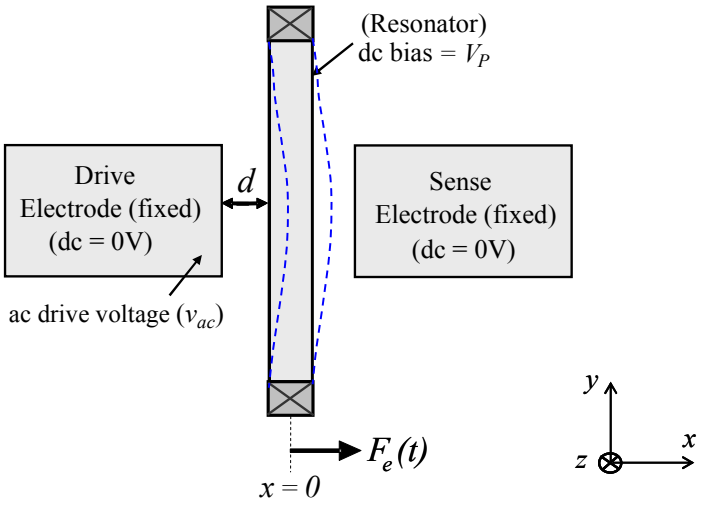

Figure 1.1: Schematic of capacitively driven-and-sensed parallel-plate resonator.

electrode and DC-biased vibrating resonator. When the frequency of drive signal is at resonant frequency of the resonator, it is set into resonance and varying capacitance changes induce current at the sense electrode. Sense current is usually detected by a current-to-voltage converter such as a transimpedance amplifier. Instead of parallel-plate gaps, comb-finger electrode gaps have also been used for transduction, usually for low frequency ranges, but the overall concept of actuation and detection is the same.

1.2 Micromechanical resonator applications

There are a wide range of applications where micromechanical resonators can be used for sensing different physical phenomena, such as sensors based on the shift in resonant frequency due to changes in stiffness, mass, or temperature. Reported applications based on the resonant frequency shift include resonant accelerometers [4-6], vibratory gyroscopes [7-11], mass sensors [12-14], biological and chemical sensors [15-17], as well as temperature sensors [18]. On the other hand, there are applications that require stable resonant frequency such as for timing and frequency reference applications. In communications, resonators are typically implemented in devices for frequency generation (reference oscillators) and for frequency selection (filters).

Reference oscillators are normally designed to operate in high HF and low VHF frequency ranges. For such frequency ranges, bulk acoustic mode resonators provide better performance than flexural type of resonators. A 60-MHz disk resonator reported in [19] provides Q in the order of 145,000 in 20-mtorr vacuum. When this disk resonator is inserted in an oscillator feedback circuit loop with a sustaining amplifier, a phase

noise of -100dBc/Hz at 1 kHz offset from carrier, and -130dBc/Hz at far-from-carrier offsets could be achieved. A 13.1 MHz single-crystal silicon resonator excited in a bulk square-extensional mode has been demonstrated in [20] with a high Q of 130,000, and it exhibits very good measured phase noise of -138dBc/Hz at 1 kHz offset, and far-from-carrier noise floor is -150dBc/Hz, which satisfies the GSM specifications. Low phase noise is the vital performance parameter for an oscillator and usually it is optimized further with other signal processing circuit techniques, such as automatic amplitude level control reported in [21].

Every wireless communication device such as a mobile phone requires highly selective filters. The filter at the RF front-end must be able to select the correct receiver band, so that only the desired band is amplified for subsequent signal processing. The frequency bands allocated for mobile phones, for example, range from 800MHz to 2.2GHz, while the bandwidth is typically around 20MHz to 75MHz [22]. The transmitter band for these systems is usually at only about 20MHz below the receiver band. Some communication systems such as CDMA and 3G, antennas are used to receive and transmit signals simultaneously. Therefore these kind of systems demand highly selective filters for both receiver and transmitter bands. Since they demand low insertion loss, steep roll-off and good stop-band rejection, high quality factor for the filter is generally desired. Nevertheless for bandwidth requirement, quality factor cannot be too high because of trade-off between Q and the *coupling* of multiple resonators.

The types of RF filters used today in wireless communications are Surface-Acoustic-Wave (SAW) filters, ceramic filters, quartz crystals, Bulk-Acoustic-Wave (BAW) filters, and Film-Bulk-Acoustic-Resonator (FBAR) filters. Ceramic filters, SAW filters and quartz crystals are bulky off-chip components that require dedicated

fabrication process and interfacing circuitry for signal processing. Filters developed from electromechanically driven resonators on the other hand are usually fabricated with surface or bulk micromachining techniques and hence, they could be more easily integrated with IC processes for a fully monolithic solution. The capacitive resonators require a DC bias voltage for proper operation, which can be an advantage as the DC bias can be used to tune the resonant frequency with the possibility of tunable filters. However, low level of DC bias is important for integration with low-power IC. Hence, the electrode-to-resonator gap must be small in sub-micron range.

The micromechanical resonators that are coupled to form a filter must scale down in size in order to operate in GHz range, as well as with sub-micron electrode gap so that insertion loss is kept low. Fabrication issues of creating *nm*-sized gap must be addressed. Moreover, bulk acoustic mode of resonance should be the preferred choice over the flexural mode. Bulk mode disk resonators have been shown to operate in GHz range with very high Q (Q ~ 10,100 @ 1.5GHz, in air) [23]. Several resonators must be *coupled* in some form to create a highly selective band-pass filter, for which, different mechanical and electrical coupling mechanisms could be realized as outlined in [24]. Mechanically, resonators can be coupled through a mechanical spring or through their clamped anchor support. For electrical coupling approach, three possible methods are capacitive coupling, electrical-cascading, and electrostatic coupling.

1.3 Performance parameters of resonator

The performance of a micromechanical resonator varies under different physical conditions, such as varying pressure or varying temperature, which interfere with the natural vibration at resonance and degrade the performance of resonator. One of the key parameters for a resonator is its *quality factor*, which is influenced by multiple loss mechanisms, particularly the loss of vibration energy through anchor support. Therefore, design and placement of anchor points will either improve or degrade the eventual measured Q of the resonator. For capacitive resonators their Q is inversely proportional to the motional resistance. The motional resistance of resonator is usually desired to be low value for easier impedance matching with other IC electronics.

Another parameter of interest is *pressure stability*, that is, how stable the resonant frequency and Q are maintained under varying pressure. The performance of resonators with capacitive air gaps eventually deteriorate at high pressures due to air damping. More collisions with air molecules will make the resonator harder to vibrate. So from a practical standpoint, pressure stability of resonator is important especially for vacuum packaging. Therefore, clear understanding of how different resonators behave under high pressure is valuable information.

Another criterion for resonator is *power handling*, that is, how much power the resonator can withstand before it deviates from normal operation, and the resonator vibrates in nonlinear regime. *Nonlinearity* of a resonator is largely associated with the geometry and the type of resonator. Two types of nonlinearity govern the overall nonlinear dynamics of micromechanical resonators: mechanical nonlinearity and electrical nonlinearity.

Changes in temperature result in corresponding changes in the elastic properties of the resonator, which eventually leads to resonant frequency drift. *Temperature stability* is important for oscillator applications that require stable reference frequency. Therefore, a method of temperature compensation is necessary for reference oscillators. Large amount of resonant frequency drift with temperature on the other hand is useful for some applications such as for temperature sensors.

1.4 Original contribution in this work

This thesis explores the performance of flexural-mode resonators and bulk-acoustic-mode resonators. Their performance is examined with regard to the following key parameters: quality factor, pressure stability, power handling, nonlinearity, and temperature stability. The overall performance of a resonator is heavily influenced by the geometry of resonator. Whether the resonator is used for sensors, oscillators or filters, it is desirable to attain a resonator design with optimized geometry for high performance under various pressures and temperatures.

During this work we have reported ultra-high quality factor values over one million in literature for the first time for micromechanical resonators in MHz frequency range. Majority of this work is on quality factor and we observed that losses through anchor supports are the main energy losses especially for bulk-mode resonators. Performance comparisons are presented for different anchor and device geometry designs. This work also presents pressure stability, power handling, nonlinearity and temperature stability of various flexural-mode and bulk-mode micromechanical

resonators. Moreover, a new idea for temperature compensation of oscillators is proposed and verified with experimental results using a composite resonator design.

1.5 Organization of the thesis

Chapter 2 presents the design of micromechanical resonators that are fabricated and used in this work, and also describes different characterization techniques used to measure their performance. Chapter 3 begins with the investigation on how quality factor of resonators are affected by different energy loss mechanisms, and subsequently energy losses through anchor support are examined with experimental results for different types of resonators. Measurements reveal that bulk-mode resonators generally have orders of magnitude higher Q than flexural type of resonators. In Chapter 4, the pressure stability of beam resonators and bulk-mode resonators are compared as the pressure is varied from high vacuum towards atmospheric pressure. Chapter 5 describes what is meant by power handling, and then followed by nonlinear behavior of flexural beam resonators, bulk-mode square resonators and disk resonators. Chapter 6 presents the resonant frequency shift with temperature, along with the proposed temperature compensation method in detail. Our method utilizes different resonant frequency characteristics with temperature of a flexural beam resonator and Lamé-mode square resonators. Chapter 7 concludes the thesis with suggestions for future works, especially in the design of micromechanical resonators for diverse applications, such as for mass sensing and wireless communications.

Chapter 2

Design and Characterization of Resonators

In this chapter, the design and electrical characterization methods are presented for different types of resonators investigated in this work, along with the fabrication process used to make these resonators. The different resonators explored in this thesis include Clamped-Clamped beams, Free-Free beams (single-ended and differential drive), length-extensional rectangular resonators, Lamé-mode square resonators, and wine glass mode disk resonators.

2.1 Simulation tools for resonator design

Initial device modeling for micromechanical resonators is usually done with Finite Element Method (FEM) and Boundary Element Method (BEM) tools such as ANSYS or Abaqus, which is used to predict the resonant frequency and analyze the mode shape. Although numerical simulation of mechanical and electrostatic interactions can be performed with these tools, system-level simulation of the mechanical device along with the transistor-level IC electronic circuits cannot be performed. System-level simulation is usually desired by the designer for accurate optimization and reduction in design

cycle. Currently, some of the available tools for circuit-level behavioural representation of MEMS are MEMSPro, MEMSMaster, NODAS, and SUGAR. The general strategy with these tools is to break up the MEMS structure into smaller elements and represent them as behavioural models, realized in Analog Hardware Description Language (AHDL), which can then be simulated in a standard electronics circuit simulator.

A modeling approach has already been presented in [25] where FEM model is transformed into AHDL model after which it is included in a system level simulation, and is demonstrated for low frequency (~ 36.5kHz) comb resonators and filters. In another behavioral modeling strategy reported by MEMSCAP in [26], a superior method has been demonstrated for a behavioural model of a 10-MHz clamped-clamped beam resonator embedded within a Pierce oscillator circuit, which was presented as a test case of the work previously reported in [27]. This behavioral modelling method for micromechanical resonator uses MemsModeler from MEMSPro, which enables simulation of MEMS resonator model in AHDL format, and has been verified in system-level simulation in Spectre of Cadence [28]. However, the modelling works well for Clamped-Clamped beam and Free-Free beam resonators and in agreement with theory, it was found to be ineffective for more complex bulk-mode square resonators.

2.2 Different types of micromechanical resonators

Early research on micromechanical resonators has been on comb finger type of resonators with low frequency of operation. Subsequently, research interests have shifted to flexural beam resonators with parallel-plate electrode gap [19, 21, 23], such as

Clamped-Clamped beam and Free-Free beam resonators that could operate in MHz frequency range. Recent research interests have focused on Bulk Acoustic Wave (BAW) micromechanical resonators suitable for oscillator and filter applications [2, 3, 19, 20, 29-34]. Bulk-mode micromechanical resonators have been shown to provide higher Q values and better power handling capabilities compared to flexural type of beam resonators [19]. The benefits of differential drive and sense of square resonator in Lamé mode have been reported in [34], where differentially driven-and-sensed 173MHz Poly-SiC square provided a Q of 9,300 in air. Furthermore, an optical characterization of square-extensional mode and Lamé mode of a square resonator has been shown to give Q values of 87,000 and 37,000 respectively in vacuum, [35]. For micromechanical resonators targeted towards VHF or UHF frequency ranges, bulk-mode square resonators or contour-mode and wine glass disk resonators have been shown to perform well due to their high stiffness. High-Q resonators are desirable for RF communication applications, provided that their motional resistance is reasonably low for good interface with other RF electronics.

The following sub-sections will briefly describe different types of resonator that are presented in this thesis, and their key performance parameters are explored in the following chapters.

2.2.1 Clamped-Clamped beam resonator

Clamped-Clamped beam resonator presented in the thesis is designed for lateral vibration in two-port drive and sense arrangement as shown in Figure 2.1. When an ac source is applied to drive electrode and dc voltage V_P is biased to moving resonator,

time-varying force is generated and as the ac drive frequency matches the natural resonant frequency of the beam, the resonator is set into vibration. The capacitive current appears at the sense electrode and it can be detected by a transresistance amplifier.

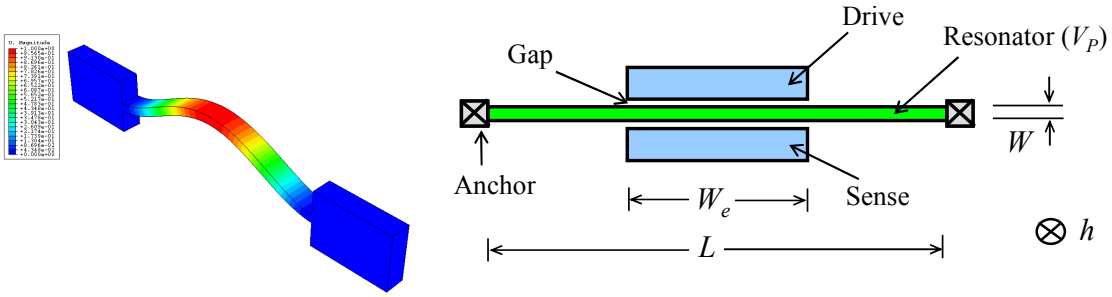

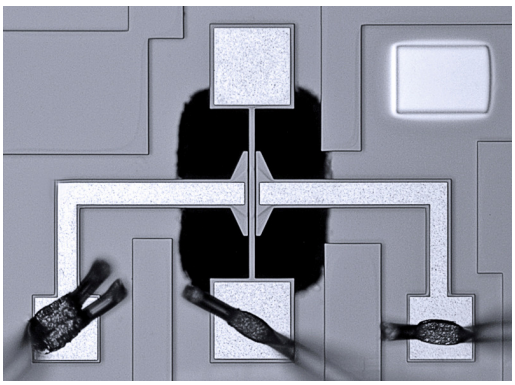

Resonance frequency, f_o	920kHz
CC beam length, L	300μm
CC beam width, W	10μm
Electrode width, W_e	150μm
Structural thickness, h	25μm
Electrode-to-resonator gap, d	2μm

Figure 2.1: Schematic of Clamped-Clamped beam resonator, micrograph and its mode shape.

An expression for resonant frequency (f_n) of Clamped-Clamped beam [36] is written as

$$f_n = 1.03 \frac{W}{L^2} \sqrt{\frac{E}{\rho}}, \tag{2.1}$$

where E and ρ are Young's modulus and density of structural material. For E = 170GPa (Si <110>) and ρ = 2330 kg/m^3 for silicon with the geometric dimensions given in Figure 2.1, the value f_n is about 977.6kHz. The resonant frequency f_n is based on mechanical vibrations and does not take into account of the electromechanical coupling, the effect of which will be discussed further in Section 2.3.1.

2.2.2 Free-Free beam resonator

A Free-Free beam resonator is designed to operate in lateral flexural mode, while its nodal locations are held in place by four flexural support tethers as shown in Figure 2.2. The support tether beams are then attached to four anchors. The combination of two support tether beams, fixed from anchor to anchor, form one large Clamped-Clamped (CC) beam designed to resonate at the *second* mode, and its resonant frequency designed to equal the *fundamental* resonance mode of the middle Free-Free (FF) beam. This arrangement of matching the resonant frequencies is important to reduce the energy losses from the middle Free-Free beam to supporting CC beams and subsequently through the anchors. The Free-Free beam is attached to nodal points of the Clamped-Clamped beams so that energy dissipated by the entire structure is at minimum, so that a high Q value could be achieved [37].

From the mode shape of the resonator structure simulated with ANSYS, as shown in Figure 2.2, the displacement of the nodal points is verified to be close to zero. In the absence of the electromechanical coupling, the resonant frequency of the Free-Free beam can be approximated, according to [38], with Euler-Bernoulli equation,

$$f_n = 1.028\sqrt{\frac{E}{\rho}}\frac{W_r}{{L_r}^2}, \tag{2.2}$$

where E is Young's modulus, ρ the density of the structural material, and W_r is the width and L_r the length of middle Free-Free beam. For the support CC beams the length L_s is taken as the length from anchor to anchor and W_s as the width and h as the thickness of the structure.

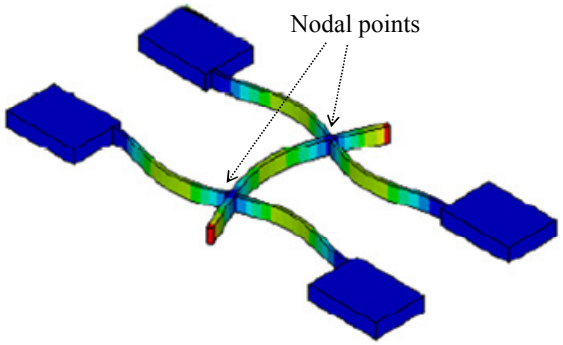

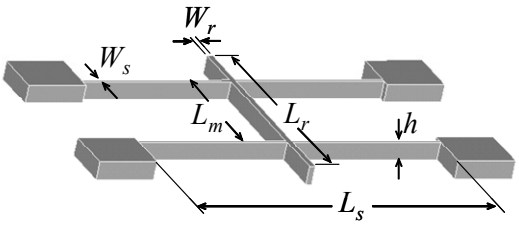

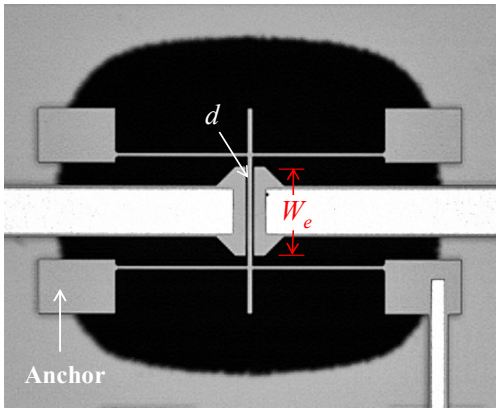

Resonance frequency, f_o	654kHz
FF beam length, L_r	320μm
FF beam width, W_r	8μm
Support beam length, L_s	420μm
Support beam width, W_s	5μm
Support beam separation, L_m	170μm
Electrode width, W_e	140μm
Structural thickness, h	25μm
Electrode-to-resonator gap, d	2μm

Figure 2.2: Schematic view of lateral Free-Free beam resonator, micrograph, its dimensions, and ANSYS simulation of its resonance mode.

For the case of large L_s–to–W_s and L_s–to–h ratios, the second mode of vibration can also be approximated by *second order* form of Euler-Bernoulli equation. After rearranging the terms, the length L_s needs to satisfy

$$L_s = 1.6833\left(\sqrt{\frac{E}{\rho}}\frac{W_s}{f_n}\right)^{1/2}, \tag{2.3}$$

where f_n is the resonant frequency of middle Free-Free beam. The measured resonant frequency of Free-Free beam resonator centers around 654kHz and it agrees well with ANSYS simulation result of 660.9kHz. Free-Free beam resonator can also be excited at its higher-order resonance modes, such as exciting at second-mode or third-mode. A general expression for the resonant frequency of Free-Free beam according to Euler-Bernoulli equation [39] is

$$f_n = \frac{1}{2\pi\sqrt{12}}(\beta_i L_r)^2 \sqrt{\frac{E}{\rho}} \frac{W_r}{L_r^2}, \tag{2.4}$$

where W_r = width of the FF beam resonator, L_r = length of the FF beam resonator. The term β_i is the mode coefficient for the i^{th} vibration mode of a FF beam obtained by solving the i^{th} root of the equation [40] given by

$$\cos(\beta_i L_r) \cdot \cosh(\beta_i L_r) = 1. \tag{2.5}$$

For the fundamental, second and third modes of vibration, $\beta_1 L_r = 4.73$, $\beta_2 L_r = 7.853$, and $\beta_3 L_r = 10.996$, respectively. The above equation is valid for FF beam resonators with large L_r–to–W_r and L_r–to–h ratios. Once L_r is scaled for higher frequencies and becomes in the order of W_r or h, more complex calculations based on Timoshenko's theory are required. A schematic view of second-mode Free-Free beam is shown in Figure 2.3.

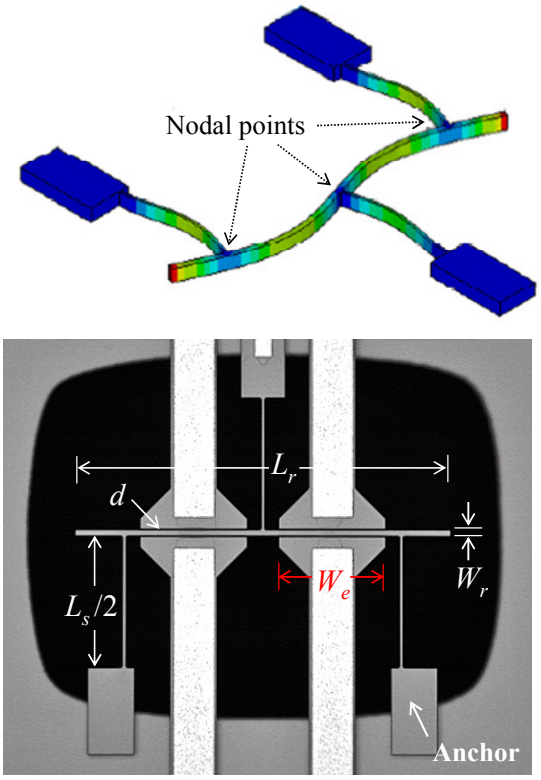

Resonance frequency, f_o	530kHz
FF beam length, L_r	650μm
FF beam width, W_r	10μm
Support beam length, L_s	470μm
Support beam width, W_s	5μm
Support beam separation, L_m	235μm
Electrode width, W_e	185μm
Structural thickness, h	25μm
Electrode-to-resonator gap, d	2μm

Figure 2.3: Micrograph of second-mode Free-Free beam, its mode shape and dimensions.

2.2.3 Length-extensional rectangular resonator

Bulk acoustic extensional mode of resonance for a rectangular block can be excited along its *length* or *width*, as well as along its *thickness*. For length-extensional resonator with length L, its middle region moves with close to zero longitudinal displacement, where anchor support is normally placed. The standing wave condition occurs at the resonant frequency (f_n) of the length-extensional mode [41], given by

$$f_n = \frac{v_s}{\lambda} = m\frac{v_s}{2L} = \frac{m}{2L}\sqrt{\frac{E}{\rho}}, \tag{2.6}$$

where v_s is the speed of sound, λ is the wavelength, m is the integer mode number, E is the Young's modulus and ρ is the density. Figure 2.4 shows the mode shape of the length-extensional resonator.

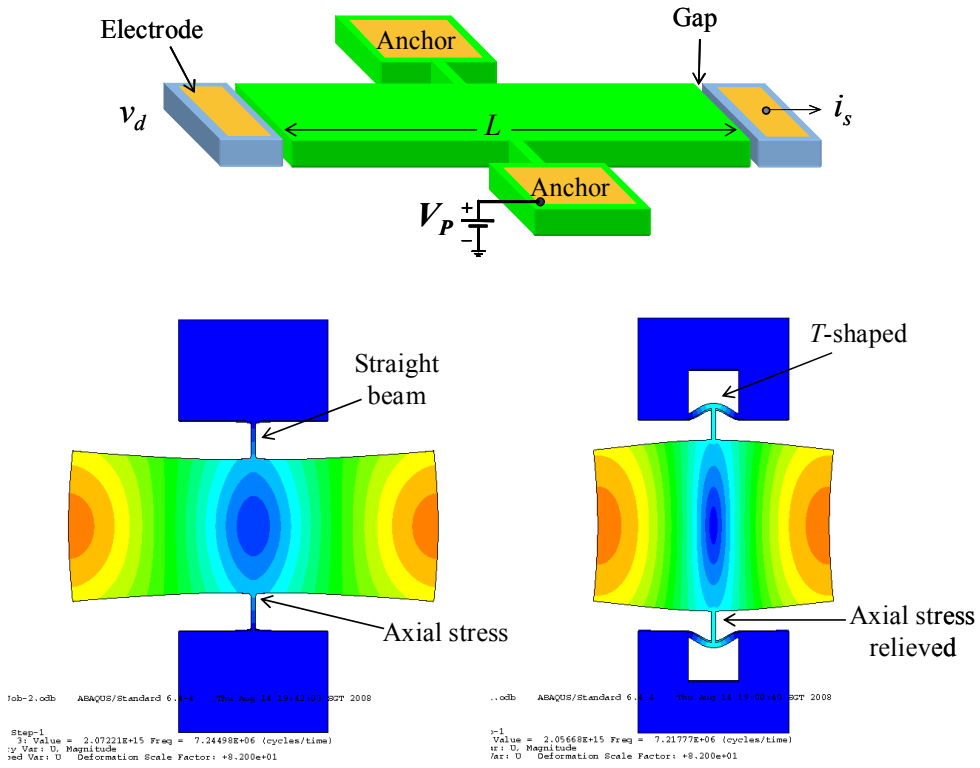

Figure 2.4: Perspective view of length-extensional resonator and mode shape. Compared to straight-beam anchor, *T*-shaped anchor allows lateral movement at the middle.

If the width of the rectangular structure is not considerably smaller than its length, then there are in-plane lateral movements that are orthogonal to the direction of longitudinal wave propagation at the middle of resonator, as shown in Figure 2.4. These in-plane lateral movements effectively impose axial stress on the straight-beam tethers that are normally placed at the middle, between the resonator and anchor support. By replacing the straight-beam tether with *T*-shaped anchor, these stresses at resonance could be relieved, as suggested by modal simulations shown in Figure 2.4.

When two length-extensional resonators are coupled in a pair with a beam, as shown in Figure 2.5, there are two resonance modes: one where both resonators vibrate in-sync and the other one with both resonators out-of-sync. The major benefit of compact two-resonator pair design is the possibility of differential drive and sense by exciting the out-of-sync mode, which will be discussed in Section 2.3.3.

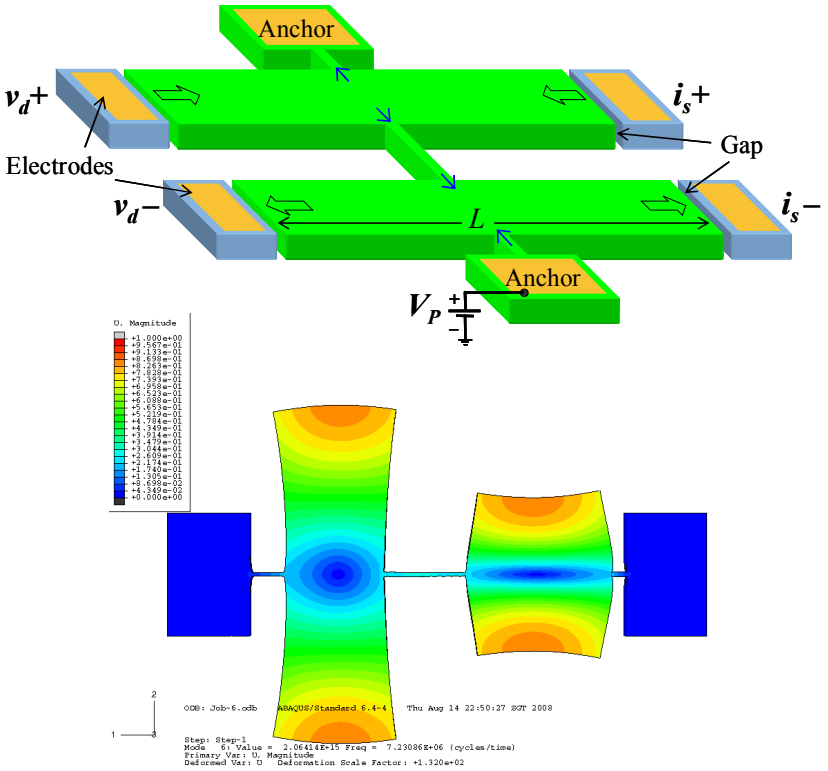

Figure 2.5: Perspective view of two length-extensional resonators in a pair and its mode shape.

2.2.4 Lamé-mode square resonator

Two bulk acoustic vibration modes are possible for square resonators, namely square-extensional mode and Lamé mode (sometimes referred as "wine glass" mode). The results presented in this thesis are based on Lamé-mode square resonators where the square vibrates with in-plane orthogonal movements. Its mode shape simulated with finite element software, Abaqus, is shown in Figure 2.6.

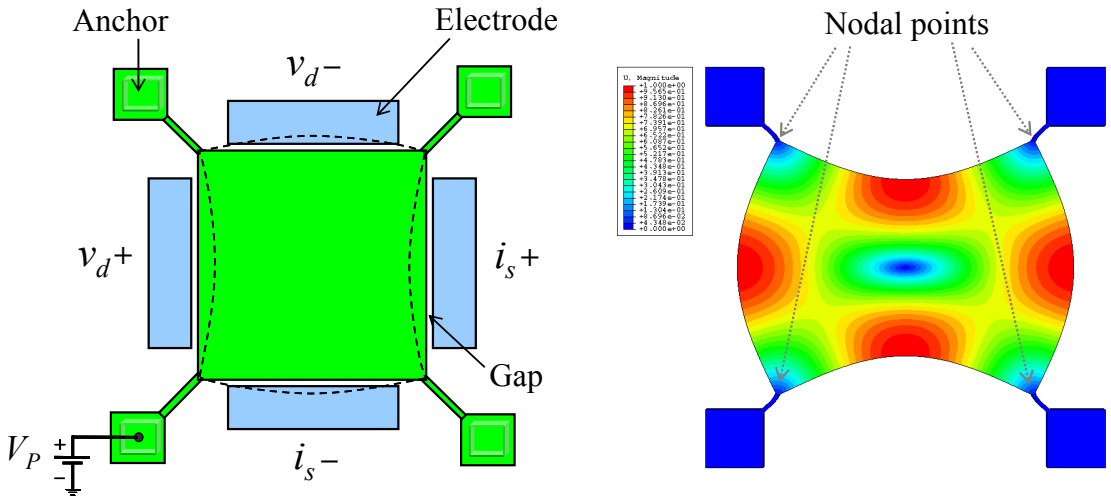

Figure 2.6: Schematic view of Lamé-mode square resonator and its mode shape simulation.

In this mode, adjacent edges of square plate bend in anti-phase while the plate volume is preserved. Nodal points of resonance are located at four corners of the square and at the centre of the plate, where anchor tether beams can be placed. Placing anchor at the centre node is possible in surface micromachining process. From analytical model for a free-standing square plate, if the side length of square L is much larger than its thickness, the square resonator can be assumed as a thin plate subjected to in-plane strain. Resonant frequency f_n can be calculated, as outlined in [33], for Lamé-mode as

$$f_n = \frac{r_m}{\sqrt{2}L}\sqrt{\frac{C_{44}}{\rho}}, \tag{2.7}$$

where r_m is the integer value for resonance mode order, and ρ is the density. The stiffness constant C_{44}, sometimes represented as G, is the shear modulus.

If the material of the square plate is assumed to be homogeneous and isotropic, then the shear modulus term G can also be expressed as

$$G = \frac{E}{2(1+\nu)}, \tag{2.8}$$

where E is the Young's modulus and ν is the Poisson's ratio coefficient.

2.2.5 Wine glass mode disk resonator

The wine glass disk resonator is supported at the four corners by tether beams attached at the quasi-nodal points of the disk, as shown in Figure 2.7, and a similar design is previously reported in [42]. As can be seen from the mode shape, the disk is squeezed or contracted in one axis while it expands in the orthogonal axis, vibrating along the plane of the disk. The vibration mode resembles a wine glass and hence it is termed with the name. The resonant frequency (f_o) of the wine glass disk resonator can be derived by solving the mode frequency equation reported in [43], given by

$$\left[\Psi_n\left(\frac{\zeta}{\xi}\right) - n - q\right] \cdot \left[\Psi_n(\zeta) - n - q\right] = (nq - n)^2, \tag{2.9}$$

where $\Psi_n(x) = \frac{xJ_{n-1}(x)}{J_n(x)}$,

$$q = \frac{\zeta^2}{2n^2 - 2},$$

$$\zeta = 2\pi f_o R\sqrt{\frac{\rho(2+2\nu)}{E}},$$

$$\xi = \sqrt{\frac{2}{1-\nu}},$$

and $n = 2$ for wine glass mode. $J_n(x)$ is the Bessel function of first kind of order n, R is radius of the disk, f_o is the resonant frequency, ν is Poisson's ratio, E is Young's modulus, and ρ is density of structural material. Above equations can be solved to derive a simplified equation for resonant frequency as presented in [44] as

$$f_o = \frac{1.6002}{2\pi R}\sqrt{\frac{E}{\rho}}, \tag{2.10}$$

which is dependent mainly on the disk radius and structural properties.

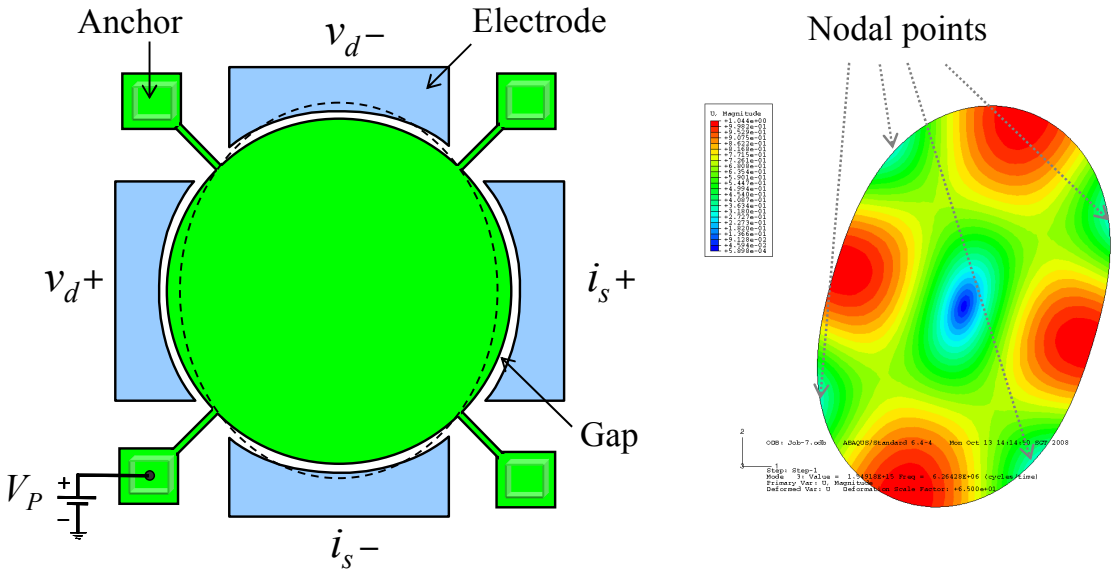

Figure 2.7: Schematic view of wine glass disk resonator and its mode simulation result.

2.3 Electrical characterization of capacitive resonators

For the purpose of evaluating the performance a micromechanical resonator, there are a number of techniques available to actuate and sense the motion of resonator. The most common approach is the electrostatic drive and sense method using electronics. Other methods used to characterize the resonator include piezoelectric approach [12, 13], optical detection techniques using laser-based photodetectors to detect the vibration amplitude [45, 46], measurement based on acoustic phonon detection [47], and using the stroboscopic scanning electron microscopy (SEM) [48]. The electrostatic excitation of micromechanical resonators with capacitive gap is typically done with an AC source along with polarization DC bias, and resulting motional current is sensed with current-to-voltage converter (transresistance amplifier). This section will present how the mechanical resonator is modeled with electrical circuit components, and describe different measurement techniques that are used to characterize the resonance.

2.3.1 Equivalent circuit model

The response of a micromechanical resonator under electrical excitation can be modeled with the classical mass-spring-damper system that is under periodic excitation force $F(t)$ as depicted in Figure 2.8. Using Newton's Second Law of motion, the dynamic response of the system can be derived to give 2nd order ordinary differential equation,

$$m\frac{\partial^2 x}{\partial t^2} + \delta\frac{\partial x}{\partial t} + kx = F(t), \tag{2.11}$$

where m is the effective mass of resonator, δ is the damping coefficient, x is the displacement along the x-axis, and k is the effective linear spring constant of the resonator.

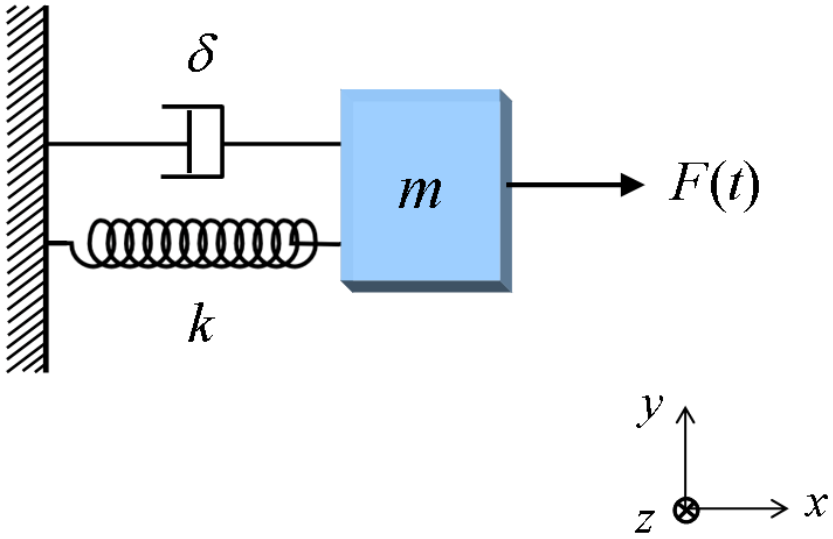

Figure 2.8: Mass-spring-damper system model for micromechanical resonator.

Given a harmonic driving force of $F(t) = F\cos(\omega t) = F\cos(2\pi ft)$, after solving the equation (2.11), an expression for the transfer function of displacement to driving force of resonator in phasor form is

$$\frac{X(j\omega)}{F(j\omega)} = \frac{k^{-1}}{\left(1-(\omega/\omega_o)^2\right)+\left(j(\omega/\omega_o)/Q\right)}, \tag{2.12}$$

where ω_o is the natural resonant frequency in radian and Q is the quality factor of the system. The vibration amplitude of resonator in time domain is then

$$|x| = \frac{F/m}{4\pi^2\sqrt{\left(f^2-f_o^2\right)^2+\left(f\cdot f_o/Q\right)^2}}, \tag{2.13}$$

where the resonant frequency f_o is

$$f_o = \frac{1}{2\pi}\sqrt{\frac{k}{m}}, \tag{2.14}$$

and the quality factor is

$$Q = \frac{\sqrt{k \cdot m}}{\delta}. \tag{2.15}$$

In Figure 2.9, when the amplitude of vibration is plotted against frequency, near the region of resonant frequency (f_o) the amplitude response is enhanced by the quality factor Q, that is, $|x| = Q \cdot F / k$ at resonance from equation (2.12).

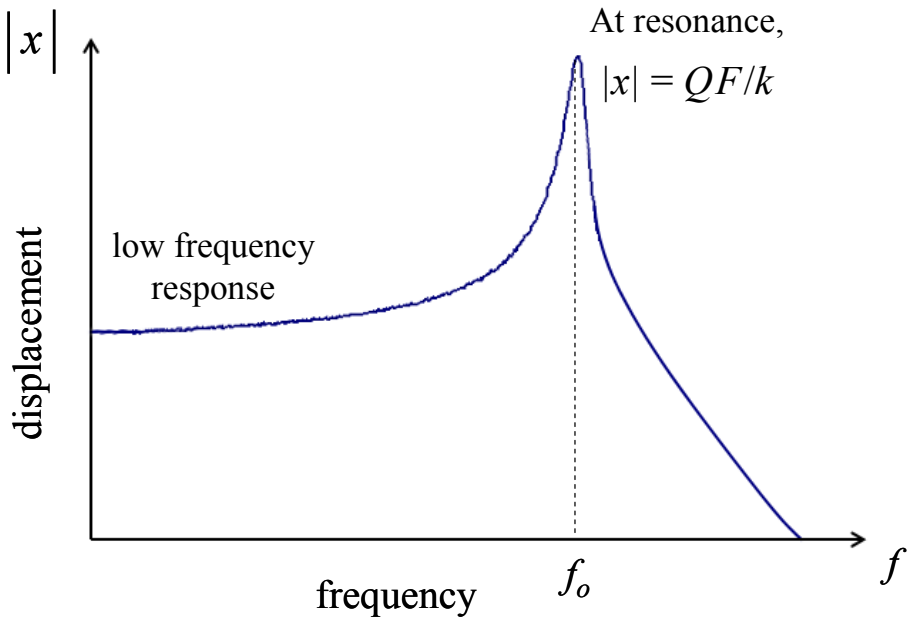

Figure 2.9: Vibration amplitude vs. frequency plot of a typical resonator.

The force that is applied for parallel plate resonators is the electrostatic force and for the combined voltage of ac drive (v_{ac}) plus the dc-bias (V_P),

$$F = \frac{1}{2}\frac{\partial C}{\partial x} \cdot \left(V_P + v_{ac}\right)^2, \tag{2.16}$$

where the term $\frac{\partial C}{\partial x}$ is the change in electrode-to-resonator capacitance per unit displacement. When the equation (2.16) is further expanded,

$$F = \frac{1}{2}\frac{\partial C}{\partial x}\left[V_P^2 + 2 \cdot V_P v_{ac} \cos(\omega t) + v_{ac}^2 \cos^2(\omega t)\right]. \tag{2.17}$$

By ignoring the dc term and much smaller squared term, the magnitude of the force is

$$F = \left(\frac{\partial C}{\partial x}\right) \cdot V_P v_{ac}. \tag{2.18}$$

The capacitance between parallel plate electrode and resonator with electrode area (A_e),

$$C = \varepsilon_o \varepsilon_r \frac{A_e}{(d-x)}. \tag{2.19}$$

Taking the partial derivative $\frac{\partial C}{\partial x}$ of equation (2.19) and substitute into equation (2.18),

$$F = \left(\varepsilon_o \varepsilon_r \frac{A_e}{(d-x)^2}\right) \cdot V_P v_{ac}, \tag{2.20}$$

where the term $1/(d-x)^2$ complicates things as it introduces *nonlinear* components once expanded out as a Taylor series. If assumption is made that $x << d$, then

$$F = \left(\varepsilon_o \varepsilon_r \frac{A_e}{d^2}\right) \cdot V_P v_{ac}. \tag{2.21}$$

If a term is defined as *electromechanical coupling factor* (η), then the force becomes

$$F = \eta \cdot v_{ac}, \tag{2.22}$$

where the term, $\eta = V_P \frac{\partial C}{\partial x} = \varepsilon_o \varepsilon_r \frac{V_P A_e}{d^2}$.

The total current through the resonator from drive port to sense port is

$$i = \frac{\partial(CV)}{\partial t} = C\frac{\partial V}{\partial t} + V\frac{\partial C}{\partial t} = C_o \frac{\partial v_{ac}}{\partial t} + V_P \frac{\partial C}{\partial x}\frac{\partial x}{\partial t}, \tag{2.23}$$

where the second term of the last part of equation (2.23) is actually termed as the motional current (i_m) at the output electrode of resonator, and also relate to η as below

$$i_m = V_P \frac{\partial C}{\partial x}\frac{\partial x}{\partial t} = \eta \frac{\partial x}{\partial t} \tag{2.24}$$

The equation (2.24) can be rearranged to give $\left(\frac{\partial x}{\partial t} = \frac{i_m}{\eta}\right)$ and substituted into equation (2.11) in order to relate the series R–L–C dynamic system to the mass-spring-damper system. Also taking into account of the $f(t)$ as the electrostatic force of equation (2.22),

$$\frac{m}{\eta^2}\frac{\partial i_m}{\partial t} + \frac{\delta}{\eta^2} i_m + \frac{k}{\eta^2}\int i_m dt = v_{ac}\,. \tag{2.25}$$

After defining the following terms for motional resistance, inductance, and capacitance,

$$R_m = \frac{\delta}{\eta^2} = \frac{\sqrt{km}}{Q\eta^2}, \qquad L_m = \frac{m}{\eta^2}, \qquad C_m = \frac{\eta^2}{k}, \tag{2.26}$$

Then, the equation (2.25) becomes

$$L_m \frac{\partial i_m}{\partial t} + R_m \cdot i_m + \frac{1}{C_m}\int i_m dt = v_{ac}\,. \tag{2.27}$$

The above equation (2.27) is actually Kirchhoff's Voltage Law (KVL) for RLC system where time-varying voltages of inductor, resistor and capacitor are summed to equal ac drive v_{ac}. Given the current and charge relationship of $i_m(t) = \frac{\partial q}{\partial t}$, the dynamic system can also be derived as second-order differential equation below

$$L_m \frac{\partial^2 q}{\partial t^2} + R_m \frac{\partial q}{\partial t} + \frac{1}{C_m} q(t) = v_{ac}\,, \tag{2.28}$$

and the Q and resonant frequency ω_o of this electrical dynamic system are

$$Q = \frac{1}{R_m}\sqrt{\frac{L_m}{C_m}}, \qquad \text{and} \qquad \omega_o = \frac{1}{\sqrt{L_m C_m}}\,. \tag{2.29}$$

Therefore, with the RLC series circuit model shown in Figure 2.10, equivalent representation of the mass is *inductor*, spring is *capacitor*, and damper is *resistance*.

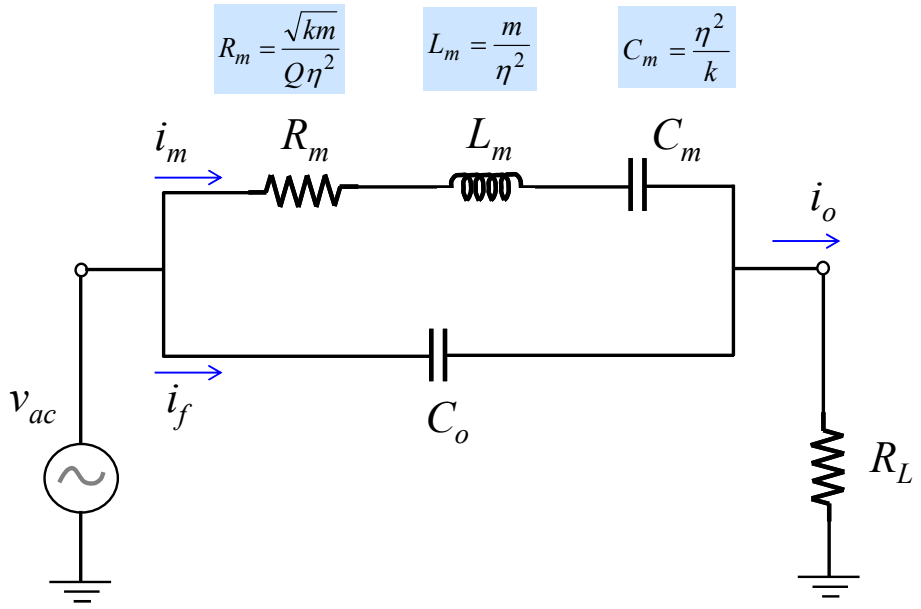

Figure 2.10: R-L-C series equivalent circuit to represent the micromechanical resonator.

Among the assumptions made to derive the basic RLC circuit model, one of the most important is that the resonator vibrates in linear region, with linear spring constant. The capacitance (C_o) in the RLC model represents the feedthrough capacitance across the input and output of the resonator. If the value of C_o is significant with large feedthrough current that could mask the sense current, it could lead to serious problems in detecting the response of the resonator. Various ways to suppress this parasitic capacitance is discussed further in Sections 2.3.3 and 2.3.4.

The RLC model can now be used in simulation with other IC circuits to analyze the behavior of resonator, such as simulation in PSpice and Cadence. However, the coupling factor η is dependent directly on dc-bias V_P, and hence the values of R_m, L_m

and C_m must be calculated for each case of the V_P values, which is rather inconvenient and does not predict the dynamic response of the resonator. Therefore, there have been research efforts to model the resonator with reduced-order behavioral modeling for better system-level simulation method with other drive and sense electronics.

2.3.2 Single-ended one-port and two-port architecture

One-port measurement method is the simplest to implement, as it requires only two electrodes, one single input electrode and the resonator itself. In this configuration shown in Figure 2.11, the equivalent circuit model to represents the resonator is the basic series RLC circuit models the motional behavior. The capacitor C_o represents the static overlap capacitance between the drive electrode and the structure of the resonator.

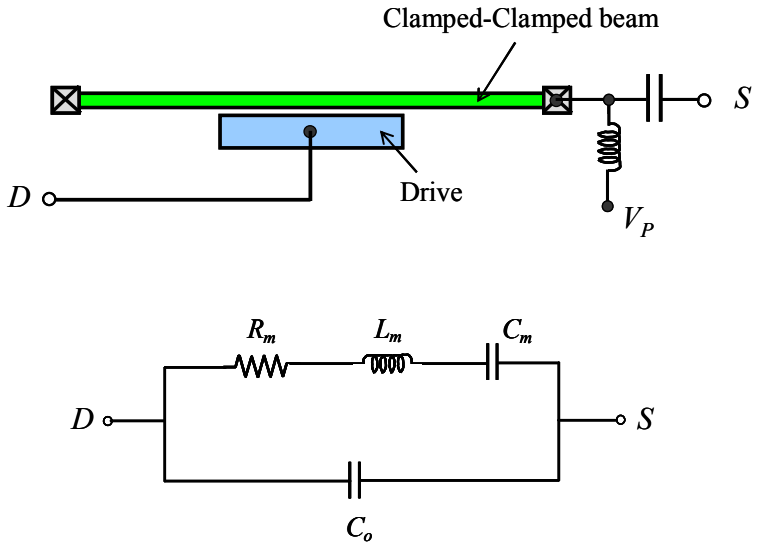

Figure 2.11: Example of one-port measurement of a beam and equivalent circuit model.

The value of C_o could become considerably large relative to R_m, so that this capacitance term will dominate; resulting in a feedthrough current that effectively masks the

motional current coming from R_m. Furthermore, C_o creates a parallel-resonance with frequency f_p, [49] given by

$$f_p = \frac{\sqrt{C_o + C_m}}{2\pi\sqrt{C_o C_m L_m}}. \tag{2.30}$$

And usually this frequency f_p is close to the resonant frequency, $f_o = \frac{1}{2\pi\sqrt{L_m C_m}}$. The parasitic feedthrough capacitance can distort the measured signal, shift the resonant peak level, and the peak usually is too small to accurately measure the Q. In order to boost the resonance response, the electromechanical coupling coefficient term η from equation (2.22) will have to be increased. This can be done by either increasing the V_P or decreasing d, the electrode-to-resonator gap.

For two-port measurement, at least three conductors are required: two electrodes and the resonator, as shown in Figure 2.12. The dc-bias V_P is applied to the resonator.

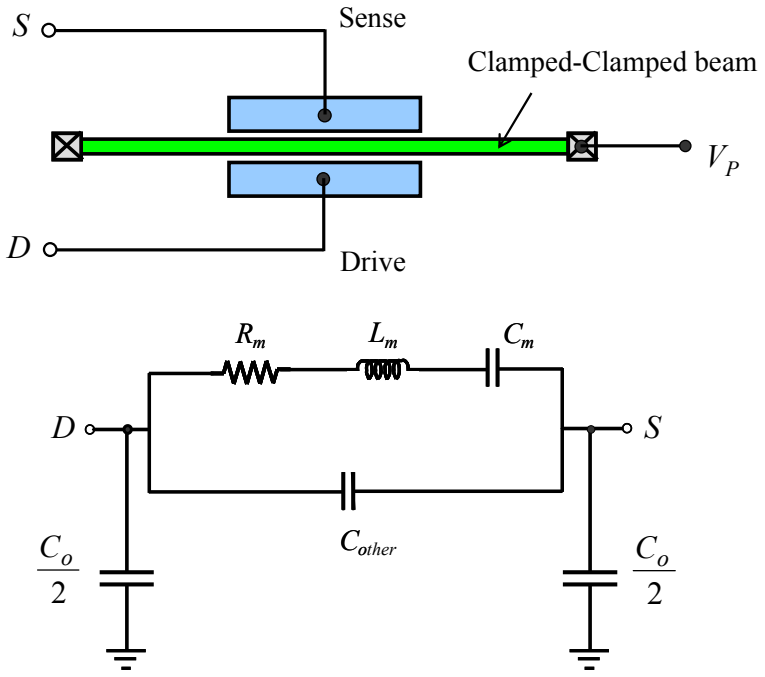

Figure 2.12: Two-port measurement of Clamped-Clamped beam and equivalent circuit model.

The AC drive input is applied to one of the electrodes, and motional current from the other one is detected. This arrangement can overcome the problem of feedthrough capacitance better than one-port method. In the equivalent circuit model, the overlap static capacitance between drive and sense is split into half and tied to ground. Other remaining capacitances still exist but much smaller and modeled as C_{other}. The strong parasitic effect of C_o is alleviated by shunting it to ground.

Two-port configuration was used to test the Clamped-Clamped beam and Free-Free beam resonators of this work. Both the resonator and a transresistance amplifier are placed inside a vacuum chamber as illustrated in Figure 2.13. Commonly, network analyzer is used for characterizing the resonance, which gives a S_{21} response plot as a ratio of output voltage from resonator to input drive levels. DC-bias voltage V_P is applied directly to the resonator proof-mass and AC signal v_{ac} from network analyzer is applied to the drive port of the device.

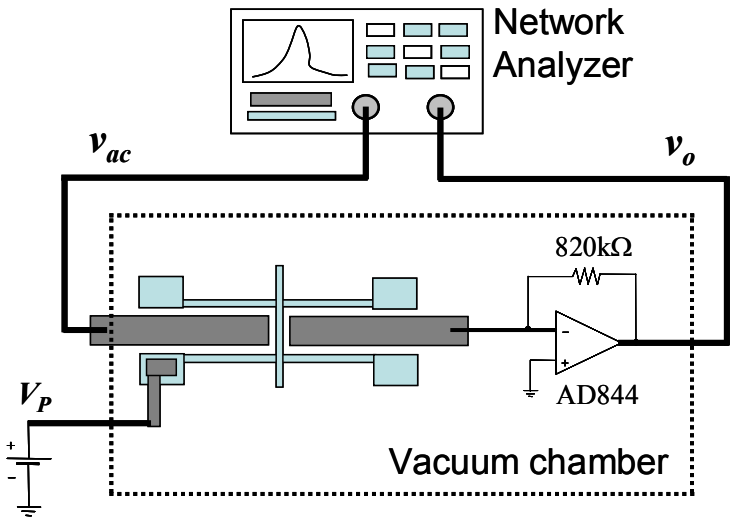

Figure 2.13. Test setup of two-port measurement in vacuum chamber.

The die containing the device is wire-bonded on the customized PCB board design and the sense electrode kept close to the input of transresistance amplifier. The SOI substrate

is grounded to reduce the parasitics caused by the feed-through capacitance. On the PCB board, the wire tracks from drive electrode are separated far apart from those of sense electrode as to reduce the coupling between drive and sense nodes. The pressure of the vacuum chamber is maintained around 37.5μTorr for all the measurements.

There is also another method of mixed signal technique, in which the resonator is excited with another drive input frequency other than the resonant frequency, and it can extract out the motional current from other parasitic currents [49, 50]. However, this technique requires more complicated measurement setup so usually used as the last resort for cases where only one-port or two-port measurement is possible with very strong parasitics.

2.3.3 Differential drive and sense architecture

If the resonator vibrates with movement in orthogonal axes with anti-phase manner, differential drive signals can be applied to excite it. There are several methods for exciting Lamé-mode square resonators differentially [34], and two main schemes shown in Figure 2.14 are demonstrated to be effective with suppressed parasitic feedthrough capacitance. The method of Figure 2.14(a) has the two orthogonal drives at adjacent electrodes while sense current can be detected from one or both of the fixed electrodes, and the resonator body is biased with V_P that serves as virtual ground in ac analysis. In Figure 2.14(b), orthogonal (dc + ac) differential drive is applied to four fixed electrodes as shown and the sense current is detected from the vibrating resonator body as common-mode sensing, and this scheme has been reported to suppress spurious

resonance modes even for extensional wine glass ring resonator [51]. Moreover, with the latter approach mode excitation is done from all four electrodes instead of two; so it increases the detected motional current. The drawback is that multiple ac and dc sources need to be coupled/decoupled using inductors and capacitors (namely the Bias-T setup).

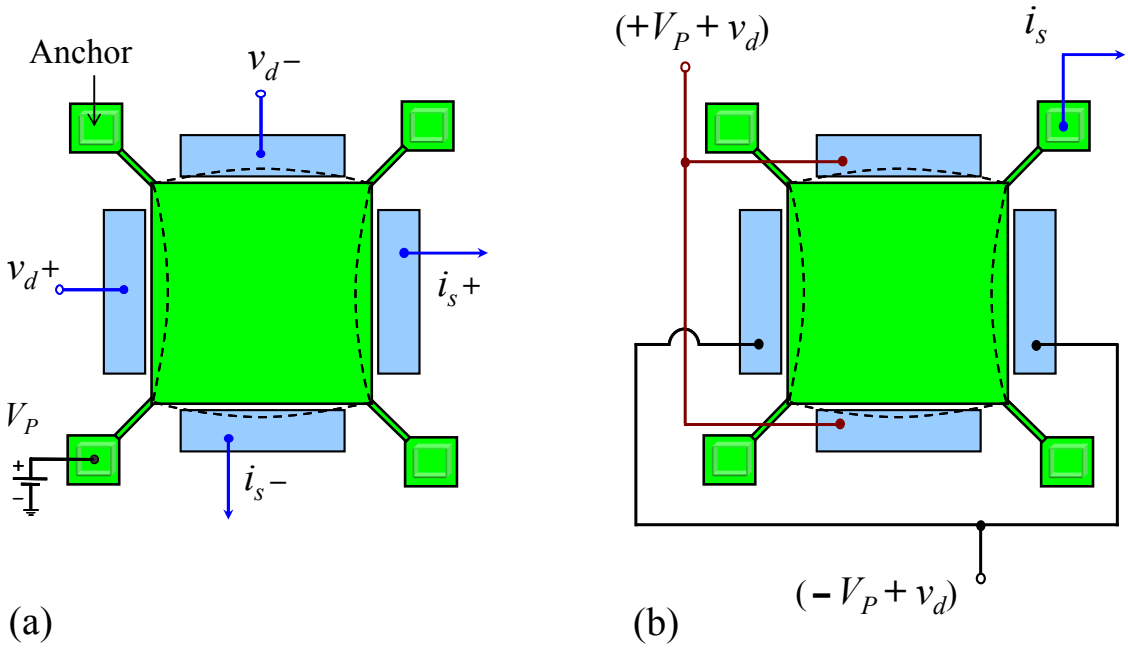

Figure 2.14: Two possible differential electrode configurations for Lamé-mode square resonator.

Figure 2.15 shows *fully differential* drive and sense measurement setup implemented. The 180° out of phase nature of the adjacent sides of the square resonator is very useful in driving the resonator differentially. Resonator's output current sensing may be done using a differential transresistance amplifier setup. Resonator die is wire-bonded to a PCB along with mounted transresistance amplifier setup, and the whole PCB is placed inside vacuum chamber. The polarization voltage V_P is applied directly to the resonator. An ac drive signal is split into positive and negative signals through a single-to-differential conversion circuit. Drive and sense are kept far apart and the SOI substrate is also grounded to reduce the parasitics caused by feedthrough capacitances.

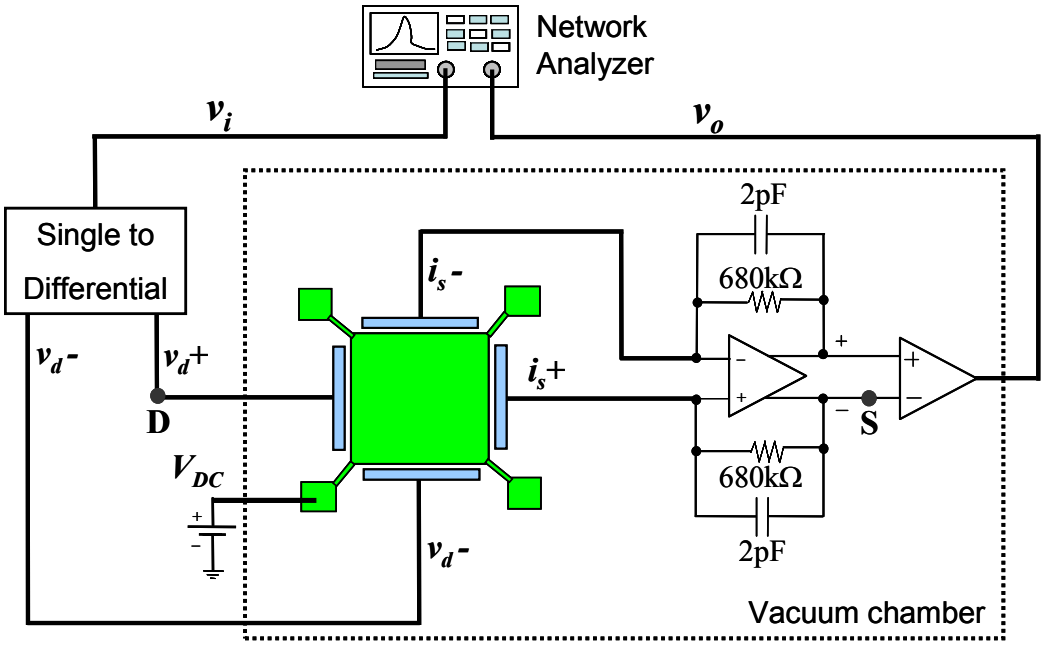

Figure 2.15: Differential drive and sense measurement setup for Lamé-mode square resonator.

A simpler alternative to fully differential sensing method is to obtain frequency response S_{21} transmission from one drive electrode (noted as D in Fig. 4), to corresponding sense electrode point (shown as S). That is, S_{21} plot is obtained for point S with respect to point D, while the two AC drives (v_d+ and v_d–) are simultaneously applied. This simplified sensing setup is sufficient to acquire a good response for characterization of Lamé-mode square resonators.

Normally, length-extensional resonator is driven and sensed in one-port or two-port electrical configuration. Such single-ended drive and sense configuration has unavoidable feedthrough capacitances, and resonance peak becomes small such that measurement of precise Q is difficult. In our approach, anti-phase mode of the two adjoining resonators (mode shape in Figure 2.5) are used where differential drive signals are applied as shown in Figure 2.16, and S_{21} response can be obtained from either one of the sense electrodes.

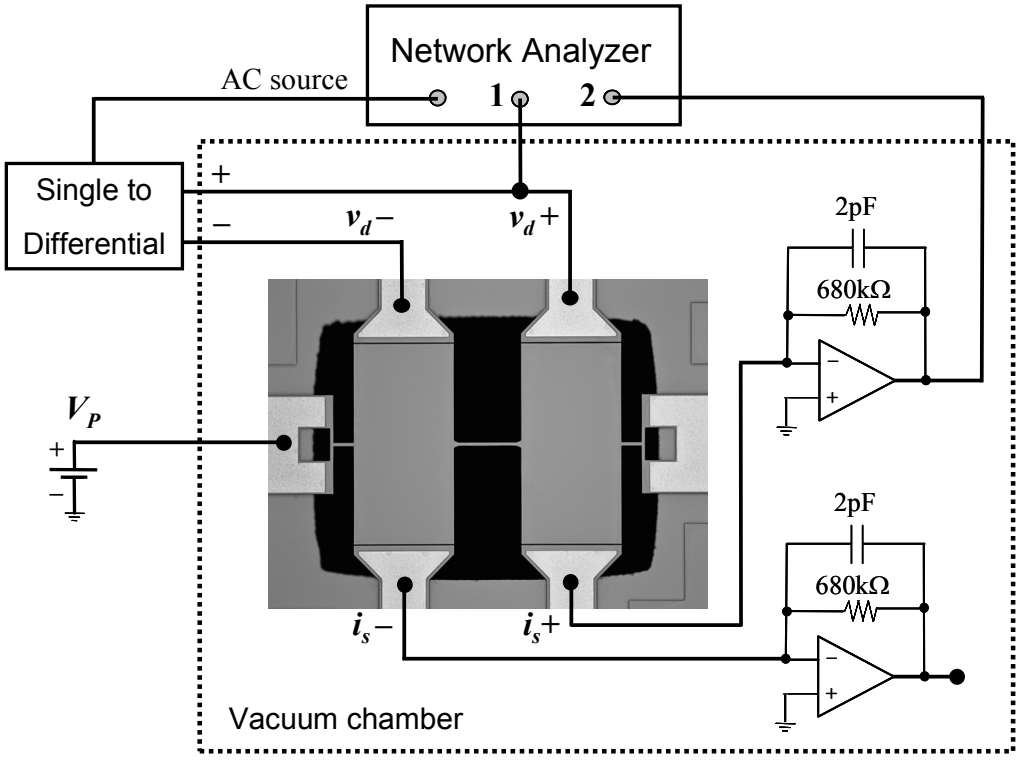

Figure 2.16: Setup for differential drive of two adjoining length-extensional resonators.

For characterization of resonant frequency, sense signal from one of the resonators is sent to input of transresistance amplifier setup. With this method, less than 1dB drowned S_{21} signal within parasitics can be improved to peak heights above 20dB. The whole resonator mass is biased with single dc bias voltage (V_P).The major benefit of this beam-coupled two-resonator pair design is the possibility of differential drive and sense. There is also no need to use external tuning capacitor that is required for negative capacitance cancellation described in Section 2.3.4 below.

2.3.4 Negative-capacitance feedthrough cancellation

The electrical equivalent model for resonator includes unavoidable feedthrough parasitic capacitance (C_o) as shown previously in Figure 2.10. A method to remove this electrical feedthrough parasitic has been demonstrated in [52], which is done through system-level circuit implementation. This is achieved by using differential outputs from a single-to-differential amplifier block with one of the differential signals is placed at the driven input of the resonator as shown in Figure 2.17. The other anti-phase output from single-to-differential is sent to a tuning capacitor (C_{tune}) placed parallel to the resonator, as a way to compensate the feedthrough capacitance that is also parallel to the resonator. With properly compensated C_{tune}, significant cancellation of the unwanted feedthrough capacitance C_o can be achieved.

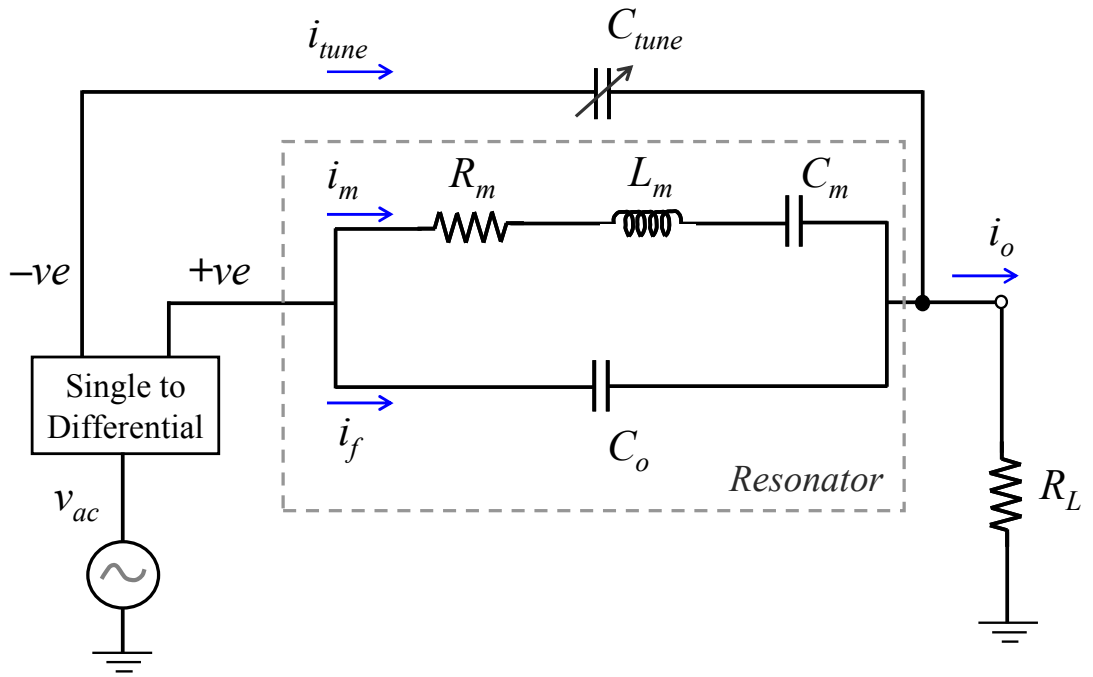

Figure 2.17: Circuit schematic for negative capacitance feedthrough cancellation method.

Moreover, instead of an external capacitor C_{tune}, another separate identical resonator to the resonator under test can also be used for negative cancellation of feedthrough capacitance, as an on-chip self-compensation scheme [53], as shown in Figure 2.18. Both resonators can be on the same chip at close proximity, and if the device layout is identical, both resonators should have almost identical capacitance across drive and sense electrodes.

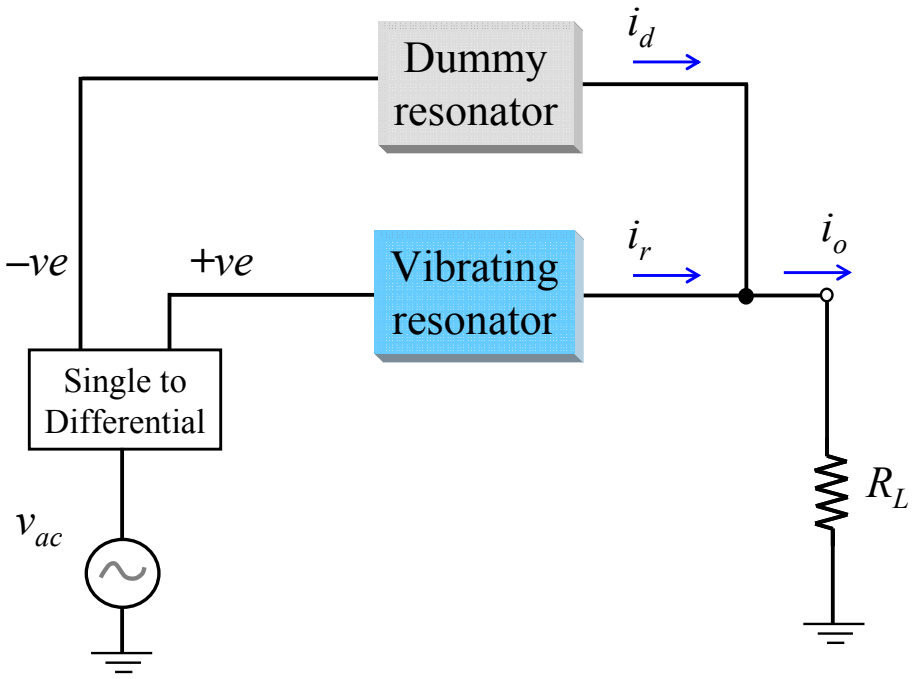

Figure 2.18: Feedthrough capacitance cancellation method with another dummy resonator.

In this setup, the dummy resonator is static and not excited at all, that is, no dc-bias is applied. Once again, one of the outputs from the single-to-differential amplifier is used to drive the resonator under test, while the other differential output is applied to the drive electrode of the dummy. Since the dummy one is static, it does not contribute with motional current and only has feedthrough current, so it acts as a capacitive element in anti-phase that compensates the feedthrough capacitance C_o of vibrating resonator.

2.4 Device fabrication process

The composite resonator die was fabricated using a commercial MEMS process, SOIMUMPs provided by MEMSCAP [54]. It is a 4-mask level SOI patterning and etching process and cross-sectional view of the layers is shown in Figure 2.19. The top structural Silicon layer is N-type doped and customers have a choice for its thickness as either 10μm or 25μm. The bottom Silicon substrate is 400μm thick, and the oxide layer between top Silicon and substrate is either 1μm thick (10μm top Si) or 2μm thick (25μm top Si).

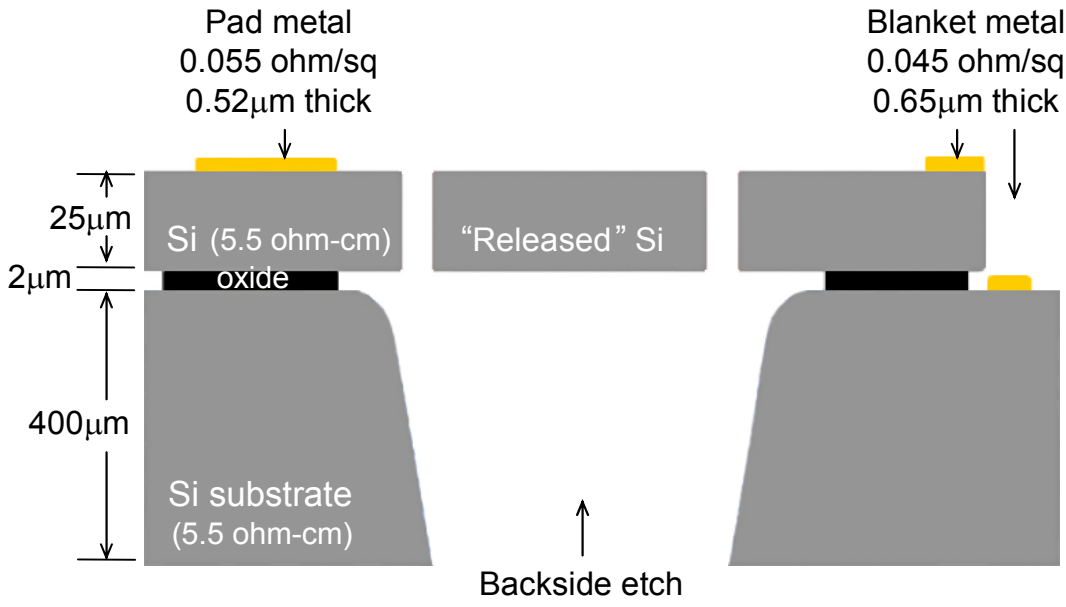

Figure 2.19: Cross-sectional view showing all layers of SOIMUMPs process by MEMSCAP.

The overall process is outlined below:

1) The "pad metal" layer with 0.52μm in thickness is first patterned on the top Silicon layer for ohmic contact through liftoff process,

2) Movable structures and anchor regions are lithographically patterned on the top Silicon layer and subsequently etched with Deep Reactive Ion Etching (DRIE),
3) Frontside protection layer is applied to protect the top Silicon layer, and the substrate Silicon is lithographically patterned from backside using the third mask,
4) DRIE of substrate is done to create deep trenches up to the buried oxide layer,
5) A wet etch process is then used to remove this oxide layer in the trench regions, and along with a dry etch process to strip away the frontside protection, Silicon structures are "released" as movable mechanical parts,
6) Then, 0.65μm thick "blanket metal" layer is deposited and patterned using a shadow masking technique.

By using this backside etch release method, frontside release process with small etch holes can be avoided and large solid movable structures can be fabricated. For example, having fully-solid medium is important for better propagation of acoustic vibrations for bulk-mode resonators. The backside release also offers the advantage of reducing parasitic capacitances between device structures and grounded substrate, which is invaluable for extracting small motional currents at higher frequencies.

Of the two types of metal layers: pad metal is best for small electrode pads and for finer metal interconnects; while the blanket metal is good for bond pads, optical mirror surfaces, large electrical routings and contact point to the substrate. Low resistivities of the structural layer and the substrate are highlighted in Figure 2.19. As to minimize the quality factor reduction from ohmic losses, all the electrodes are coated with pad metal whose sheet resistance is as low as 0.055Ω/sq. The minimum feature size for top structural Silicon is 2μm, therefore the electrode gap is limited to 2μm as well.

2.5 Summary

The micromechanical resonators designed and fabricated can be classified into flexural mode and bulk acoustic mode resonators. Different resonator types investigated in this study for their performance are Clamped-Clamped beam, Free-Free beam (fundamental mode and second mode), Length-extensional rectangular resonators (single and two-resonator pair), Lamé-mode square resonators, and wine-glass mode disk resonators. Various electrical characterization techniques outlined in this chapter are one-port, two-port, mixed signal, differential architecture, and negative capacitance feedthrough parasitic cancellation. Presented techniques also apply to other types of capacitive resonators based on electrostatic excitation as well. Various performance parameters can be investigated using the measurement techniques described in this chapter. The following chapters will explore each of the main performance parameters of the resonators in detail to further understand their behavior under various pressure levels and temperature conditions.

Chapter 3

Quality Factor of Resonators

In this chapter, quality factor is evaluated for different types of resonators that have been presented in previous chapter. Comparison of quality factor is made for resonators with different geometry such as the type of anchors, number of anchor supports, and thickness of structural material. A brief description of different energy loss mechanisms that contribute to the quality factor is presented. Moreover, energy losses through anchor support are observed as one of the key factors that will limit the Q performance as the resonators are scaled to higher frequencies.

3.1 Definition of quality factor

The basic definition of quality factor for a resonator with mechanical vibration is the ratio of maximum energy stored per cycle ($E_{stored-max}$) to energy dissipated per cycle of vibration ($E_{dissipated}$) [55] as

$$Q = 2\pi \frac{E_{stored-\max}}{E_{dissipated}}. \tag{3.1}$$

Therefore, in order to achieve high quality factor, stored vibration energy must be optimized while energy dissipation should be kept at minimum. Another definition for

quality factor that is useful for resonance response obtained through electrical characterization is the ratio of resonant frequency (f_o) to the frequency bandwidth at 3dB below the resonance peak (Δf_{3dB}), expressed as

$$Q = \frac{f_o}{\Delta f_{3dB}}. \tag{3.2}$$

The energy dissipation and quality factor can also be expressed in the form of a complex-valued resonant frequency, which is useful in simulation tools that calculate the eigenfrequency (ω) of the resonance mode [56]. The real part gives the resonant frequency and the imaginary part corresponds to the damping as below

$$Q = \frac{1}{2}\frac{\mathrm{Re}(\omega)}{\mathrm{Im}(\omega)}. \tag{3.3}$$

A higher Q along with the associated lower motional impedance for a resonator translates to improved stability for oscillators, better frequency selectivity for filters, and enhanced sensitivity and resolution for a resonant sensor.

3.2 High-Q resonators in literature

Impressive frequency-Q products in the order of ~10^{13} have been demonstrated for electrostatically transduced bulk-mode resonators [30, 31, 2, 57]. One major challenge faced by micromechanical resonators is interfacing directly with RF electronic circuits, given their large series motional resistance (R_m). Thus, high-Q resonators are desirable for communication circuits, and their motional resistance must be reasonably low for good interface with IC electronics. Performance of 13.1MHz square-extensional mode

oscillator outlined in [20] has a Q value of 130,000 in vacuum, along with low phase noise that satisfies the GSM specification. Another possible bulk-mode excitation of square resonator is to operate in Lamé mode. The benefit of differential drive-and-sense of Lamé mode square resonator is reported in [34], where differentially driven-and-sensed 173MHz Poly-SiC square resonator had a Q of 9,300 in air.

Although a 92MHz free-free beam resonator has been shown to have a Q of 7450 at 50μTorr [38], and a 71.7MHz corner-support square plate resonator is reported to have a Q of 17,500 at 200μTorr [59], using bulk mode or contour mode disk resonators, Q could be enhanced to higher values, such as in the order of 145,000 for a 60MHz wine-glass disk resonator under 20-mTorr vacuum [42]. Other bulk-mode resonators have also been shown to provide high Q's > 100,000. A summary of selected high-Q resonators found in literature is listed in Table 3.1, and suggests that higher Q values are achievable when excited in bulk mode, whether the resonator is a square, a disk, a ring, a beam, or a rectangular block. Moreover, stiffer materials provide better Q values even in air, as in the case of 1.51GHz nanocrystalline diamond disk resonator [30] and 173MHz Poly-SiC square resonator [34].

A scaling product of resonant frequency and quality factor ($f_o \times Q$) is usually used as a performance measure, which is also listed in Table 3.1, and it highlights the superior performance of bulk-mode resonators. The f_o–Q products for bulk acoustic mode resonators presented in this thesis are in the order of ~10^{13}, and high quality factor is sustained at relatively high pressures. If the quality factor values from Table 3.1 are plotted against corresponding resonant frequency and shown in Figure 3.1, it show that Q is roughly proportional to the inverse of resonant frequency, and as the target frequency is increased the Q value will come down.

Table 3.1: Resonant frequency and quality factor of high-Q resonators reported in literature, along with ($f_o \times Q$) product at tested pressure.

Resonator Design	f_o	Q	($f_o \times Q$)	Pressure
a) Free- Free beam [38]	92MHz	7,450	6.85×10^{11}	50μTorr
b) Flexural square plate [59]	71.7MHz	17,500	1.25×10^{12}	200μTorr
c) Wine-glass disk [42]	60MHz	145,780	8.75×10^{12}	20mTorr
d) Diamond disk [30]	1.51GHz	10,100	1.53×10^{13}	Air
e) Hollow-disk ring [31]	1.2GHz	14,600	1.75×10^{13}	Vacuum
f) Elliptic bulk-mode disk [65]	149.3MHz	45,700	6.82×10^{12}	100mTorr
g) Width-extensional SiBAR [66]	100MHz	92,000	9.20×10^{12}	Vacuum
h) Length-extensional beam [32]	12MHz	180,000	2.16×10^{12}	0.01mbar
i) Extensional-mode square [20]	13.1MHz	130,000	1.70×10^{12}	0.01mbar
j) Poly-SiC Lamé-mode square [34]	173MHz	9,300	1.61×10^{12}	Air
k) SOI Lamé-mode square [35]	12.1MHz	37,000	4.48×10^{11}	1mbar
l) SOI Lamé-mode square [67] *	12.9MHz	800,000	1.03×10^{13}	36μTorr
m) Lamé-mode squares [68] *	6.35MHz	1,700,000	1.08×10^{13}	36μTorr
n) Wine glass disk resonator [57]	5.4MHz	2,000,000	1.08×10^{13}	Vacuum
o) Quartz crystal [1]	10MHz	1,300,000	1.30×10^{13}	Vacuum

* Resonators of this work

It can be seen from Figure 3.1 that the f_o–Q product of different resonators may be constant for a given mode shape with the same material. If there is a limit line representing the maximum achievable Q for a particular type of resonator, then it serves as a measure of how efficient the anchor design with minimum energy losses when measured quality factor is compared with the predicted Q limit value. From theory reported in [60] that for bulk-mode resonators Q value prediction based on physical properties of material is inversely proportional to the resonant frequency.

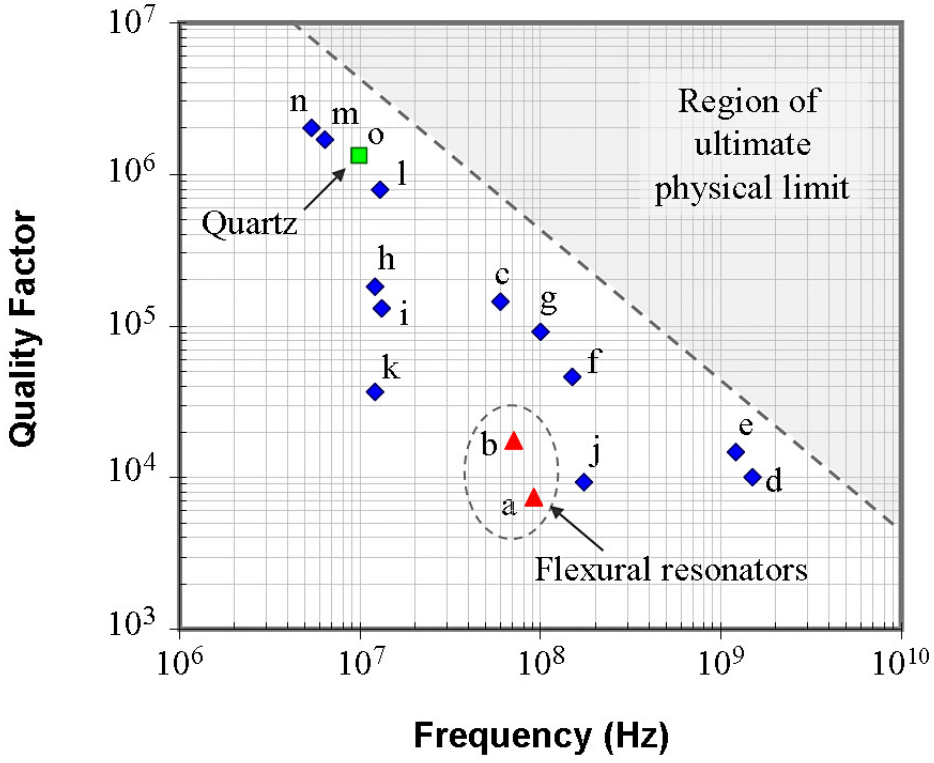

Figure 3.1: Q vs. frequency plot in log-log scale of reported resonators in literature with f_o–Q products as listed in Table 3.1.

The quality factor cannot be improved indefinitely, at some point it must hit the ultimate physical limit of the material. For bulk-mode micromechanical resonators with properly designed anchor support, the maximum achievable Q limit is imposed by the *thermoelastic* dissipation and/or *phonon* damping (termed *Akhieser* effect) that was originally described by A. Akhieser [61]. Two theories exist in literature to explain the acoustic attenuation in single crystal materials, one by Woodruff and Ehrenreich [62] and the other by Mason and Bateman [63]. More recently the study of acoustic attenuation in silicon is reported in [64], and overall, the attenuation is highly dependent on the temperature and the direction of wave propagation. Understanding the attenuation of acoustic waves due to interaction of acoustic phonons and thermal phonons would be very helpful in the analysis of measured quality factor for bulk-mode resonators.

3.3 Quality factor limitation by loss mechanisms

Simulation and prediction of accurate Q value for a resonator is not a straightforward task due to difficulty in modeling various loss mechanisms. In general, different energy dissipation mechanisms contribute to the quality factor. A value for quality factor is derived for each individual loss mechanism, and the inverse of the individual Q's are summed to give an overall expression,

$$\frac{1}{Q_{total}} = \sum \frac{1}{Q_{ind}}. \tag{3.4}$$

Depending on the designed geometry of the resonator, various energy losses that could reduce the Q may come from intrinsic material damping, air damping, thermoelastic dissipation (TED), anchor losses, and other surface loss mechanisms [69-71]. These various Q-limiting factors on the overall Q (Q_{total}) is usually expressed as below

$$\frac{1}{Q_{total}} = \frac{1}{Q_{anchor}} + \frac{1}{Q_{air}} + \frac{1}{Q_{TED}} + \frac{1}{Q_{surface}} + \frac{1}{Q_{others}}, \tag{3.5}$$

where each term represents the contribution to Q_{total} from corresponding energy loss mechanism. Therefore, Q with respect to a particular loss mechanism is calculated independently and summed into equation (3.5) as Q^{-1} term. So the mechanism with lowest Q is considered as the dominant loss mechanism. Losses due to air damping can basically be negligible by placing the resonator in vacuum.

The term Q_{air} is inversely proportional to the pressure above a certain pressure level, and this level is in the range of 0.1Pa to 1Pa for flexural tuning fork beam resonators reported in [70]. $Q_{surface}$ is relatively large for resonators with large surface-to-volume ratios, which is the case for large bulk-mode resonators.

As mentioned in [69], Q_{TED} is much larger than Q_{anchor} (Q due to support losses at anchors) for disk resonators in VHF and UHF range. Therefore, Q_{total} for square bulk-mode resonator is likely not limited by TED either. A detailed analysis of TED and simulation methods for Q of different beam resonators is reported in [71], in which theoretical simulations of Q_{TED} and experimental Q are highly correlated for flexural beams, and thus Q of flexural beam is limited by TED. It is also reported in [71] that Q_{TED} simulations for longitudinal or length-extensional bulk resonators is one or two orders of magnitude higher than measured Q, suggesting that TED does not contribute significantly to overall energy losses. For a square resonator in Lamé-mode at resonant frequency in HF and VHF range, there is little expansion in volume and TED is probable not the dominant loss mechanism.

Therefore, anchor losses could be the dominant Q-limiting factor for bulk-mode resonators. It is through the anchors that vibration energy of resonator is dissipated through elastic wave propagation. Analytical models for Q have been formulated in [69] for bulk-mode side-supported disk and centre-supported disk resonators, and shown to be correlated to measured Q values. The models are derived from physical phenomenon that deformations of the disk induce stress at the boundary region between the anchor beam and supporting substrate, and that this stress acts as an excitation source for elastic waves that propagate and lost through the substrate.

The same concept could be applied to Lamé-mode square resonator, where lateral rotational tilting motion of square corner at resonance introduces shear stress on the anchor support structure. Therefore, for Lamé-mode square resonators in vacuum with negligible air damping, anchor losses are probably the dominant loss mechanism governing the overall quality factor.

Depending on the design of the resonator the anchor losses could be the dominant Q limiting factor for bulk-mode resonators. It is through the anchors that vibration energy of resonator could be lost as elastic wave propagation. Anchor loss simulation method has been reported in [56], termed as a perfectly matched layer (PML) method that allows efficient modeling of energy losses through the substrate. This PML method was applied in the development of HiQLab, a finite element simulation tool that could simulate the effects of TED and anchor loss damping mechanisms.

For bulk acoustic wave (BAW) resonators operating in high vacuum, even if anchor losses are minimized such that they can be assumed no longer dominant, there is still elastic damping within structural material that will attenuate the acoustic vibrations. An expression for this elastic damping could be complicated due to its dependence on many factors such as temperature, the type and frequency of vibration, and so on. However at room temperature, the acoustic vibration losses within the material can be represented by a *viscous damping* component [72]. The overall relationship between stress and strain in tensor form can be represented as

$$\mathrm{T}_{ij} = \sum_{k=1}^{3}\sum_{l=1}^{3}\left(C_{ijkl}\Psi_{kl} + \gamma_{ijkl}\frac{\partial \Psi_{kl}}{\partial t}\right), \tag{3.6}$$

where T_{ij} is the stress field, Ψ_{kl} is the strain field, and C_{ijkl} is the second rank stiffness tensor. The second term of equation (3.6) is added to include the time derivatives of the strain $\left(\partial\Psi_{kl}/\partial t\right)$, where γ_{ijkl} serves as *viscosity tensor* that relates the time derivatives of strain tensor to the stress tensor T_{ij}.

The x-, y-, and z- axes are assigned with numbers 1, 2, and 3, respectively. The subscripts *ij* and *kl* represent the relation between the axes, for example, T*ij* = T_{12} refers

to shear stress between x-axis and y-axis. The notation can be further simplified using the symmetry nature of stress and strain tensors, that is, $T_{ij} = T_{ji}$, $\Psi_{ij} = \Psi_{ji}$, $C_{ijkl} = C_{jikl}$, and $C_{ijkl} = C_{ijlk}$. Then, the four-number notation *ijkl* can be simplified to two-number one, that is, 11 → 1, 22 → 2, 33 → 3, 23 or 32 → 4, 13 or 31 → 5, and 12 or 21 → 6. For example, T_{12} becomes T_6 and C_{2332} then becomes C_{44}.

Then, the viscosity tensor γ_{ijkl} can be represented by 6 × 6 matrix $[\gamma]$ of viscosity constants. Since the acoustic wave amplitude eventually decays in a lossy medium, an *attenuation factor* can be derived as a measure of acoustic attenuation. For longitudinal acoustic wave propagating in single crystal cubic material along the cube edge, the attenuation factor (α) can be expressed [72], in (dB/m) as

$$\alpha = 4.343\sqrt{\frac{\rho}{C_{11}}}\left(\frac{\gamma_{11}}{C_{11}}\right)(2\pi f)^2, \tag{3.7}$$

where C_{11} is a stiffness constant and γ_{11} is the corresponding viscous damping that relates strain Ψ_{kl} and stress T_{ij}, ρ is the density of material, and f is the vibration frequency. From equation (3.7), the acoustic attenuations at room temperature in single crystal materials, such as single crystal silicon, increase with the square of the frequency. The acoustic attenuation is measured by amplitude ratio over distance usually in units of *decibel* (dB) per meter. For silicon, stiffness constants of silicon reported in [73, 74] are C_{11} = 165.7GPa, C_{12} = 63.9GPa, C_{44} = 79.56GPa. Then, the viscous damping γ_{11} can be calculated in units of N.s/m^2. Therefore, for longitudinal acoustic waves propagating in single crystal silicon, a term called *acoustic quality factor* (Q_a) [72] can be defined as

$$Q_a = \frac{C_{11}}{2\pi f \gamma_{11}}. \tag{3.8}$$

The acoustic quality factor of equation (3.8) is actually based on wave attenuation *per wavelength* (λ), so if the bulk mode of resonator has acoustic standing wave over the length of $1/2\lambda$, such as the length-extensional resonators presented in Section 2.2.3, then the equivalent acoustic quality factor is ($2 \times Q_a$). This quality factor estimate indicates the best possible Q a length-extensional resonator can achieve if other energy losses such as anchor losses are at very minimum.

The acoustic quality factor formula is actually different for different type of waves such as longitudinal waves or shear waves, as well as the direction of propagation along crystal cube edge or along face diagonal. The attenuation factor and acoustic quality factor formulas in equations (3.7) and (3.8) can be modified for shear (or transverse) acoustic waves propagating along cube edge by replacing C_{11} and γ_{11} terms with shear modulus C_{44} and viscosity constant γ_{44} as

$$\alpha = 4.343\sqrt{\frac{\rho}{C_{44}}}\left(\frac{\gamma_{44}}{C_{44}}\right)(2\pi f)^2, \qquad Q_a = \frac{C_{44}}{2\pi f \gamma_{44}}. \tag{3.9}$$

The viscous damping described above is a general expression for acoustic attenuation that is contributed by *thermoelastic* damping and *Akhieser* damping. TED for longitudinal acoustic wave is mainly due to heat conduction from compression regions to rarefaction regions. Therefore, TED contributions for Lamé-mode square and wine glass disk resonators are at minimum because these modes are based mainly on shear waves that do not produce changes in volume of structural material. At a certain temperature, all materials have thermally-excited *phonons* (intrinsic acoustic waves) that are in equilibrium. When longitudinal or shear acoustic waves propagate through the material they disrupt this phonon equilibrium and induce phonon-based Akhieser

damping [72]. Therefore, viscous damping due to Akhieser effect applies to both longitudinal wave and shear wave propagation within the resonators.

The results reported in [72] indicate that the acoustic wave attenuation generally increases in single crystal materials in the order of *insulator* → *semiconductor* → *metal*. For example for copper and gold, the acoustic attenuation factor for longitudinal wave is 2.7dB/m and 2.0dB/m at 10MHz, respectively, which is more than 20 times the attenuation factor in single crystal silicon of roughly 0.1dB/m at 10MHz. Furthermore, acoustic attenuation within polycrystalline materials is usually much larger than that with single crystal materials, so bulk-mode resonators made from polysilicon should perform worse than the single crystal silicon bulk-mode resonator.

3.4 Flexural mode versus bulk acoustic mode

Mechanical vibrations of flexural-mode resonators are characterized by some type of out-of-plane deflection, for example, a beam with different boundary conditions, or a square with out-of-plane fluctuation. Bulk-mode resonators on the other hand are characterized by in-plane vibrations with the entire body extending or contracting due to coupled acoustic wave vibrations within the body of resonator.

From the perspective of high-Q performance for micromechanical resonators, bulk-acoustic-mode or contour-mode type of resonators provide better performance mainly due to their high stiffness and larger vibration energy storage capacity compared to flexural-mode resonators, as the dimensions are scaled for higher frequencies. When the dimensions for a flexural-type resonator become smaller for higher resonant

frequency, Q value usually goes down severely along with a decrease in power handling. Moreover, the increase in anchor losses for Clamped-Clamped beams become very large as frequencies get higher, to the point where at 70 MHz, Q drops to only 300 [58].

3.4.1 Flexural-mode beam resonators

A resonance plot of Clamped-Clamped beam design presented in Section 2.2.1, driven at 60V dc and 61mVpp ac, is shown in Figure 3.2. Measured quality factor using equation (3.2) is 4,059 at resonant frequency of 917.1kHz in vacuum, and the phase plot shows the typical 180° phase shift at resonance. The resonant frequency is measured in two-port setup and S_{21} plots from network analyzer are recorded.

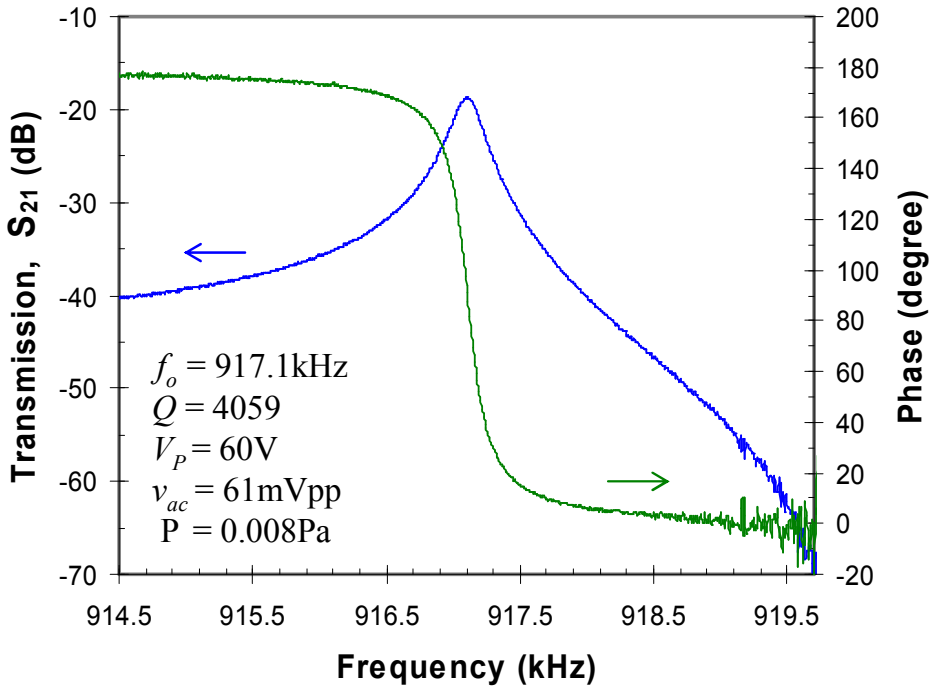

Figure 3.2: Measured S_{21} transmission of 917.1kHz Clamped-Clamped beam resonator.

As shown in Figure 3.3, measured resonant frequency depends on dc-bias V_P, and it shifts to lower frequency with increasing V_P. This well-known characteristic of capacitive micromechanical resonator is termed *negative electrostatic spring softening*. The resonant frequency predictions derived from mechanical vibration theories presented in Section 2.2 is incomplete for capacitive resonators.

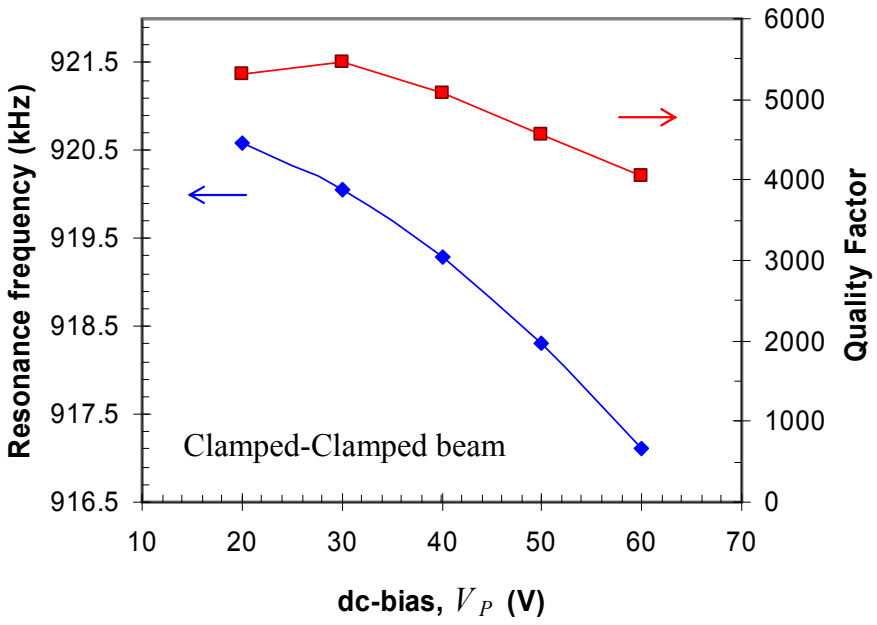

Figure 3.3: Plots of resonant frequency and Q vs. dc-bias voltage V_P for CC beam resonator.

A more accurate expression of resonant frequency taking into account of electromechanical coupling is given by

$$f_o = \frac{1}{2\pi}\sqrt{\frac{k_{eff}}{m_{eff}}} = \frac{1}{2\pi}\sqrt{\frac{k_m + k_e}{m_{eff}}}, \tag{3.10}$$

where k_{eff} and m_{eff} are effective spring constant and mass, k_m is the linear mechanical spring constant, and k_e is the linear electrical spring constant. Equation (3.10) can then be further derived to give

$$f_o = \frac{1}{2\pi}\sqrt{\frac{k_m}{m_{eff}}}\left[1+\left(\frac{k_e}{k_m}\right)\right]^{1/2} = f_n \cdot \left[1+\left(\frac{k_e}{k_m}\right)\right]^{1/2}, \tag{3.11}$$

where f_n is the nominal resonant frequency of ideal resonator without coupling that is derived from mechanical vibration theory. The exact value of linear electrical spring constant k_e depends on how exactly the resonator is driven in one-port, two-port, or differential drive architecture as described previously in Section 2.3. For the case of two-port capacitively driven-and-sensed resonator with parallel-plate electrodes as shown in Figure 2.12, the term k_e can be expressed as

$$k_e = -\frac{2\varepsilon_o A_e}{d^3} {V_P}^2, \tag{3.12}$$

where ε_o is permittivity of free space, A_e is the area of parallel-plate electrode overlap region on one side, and d is the electrode-to-resonator gap. The "negative" sign for k_e indicates that the electrostatic spring force acts in a direction opposite to the mechanical restoring force. Above k_e expression assumes that the resonator is in linear vibration mode. Further complications due to nonlinearities will be discussed in Chapter 4. So the overall expression for resonant frequency (f_o) becomes

$$f_o = f_n \cdot \left[1-\left(\frac{\frac{2\varepsilon_o A_e}{d^3}{V_P}^2}{k_m}\right)\right]^{1/2}. \tag{3.13}$$

The equation (3.13) indicates that resonant frequency is dependent on the dc-bias V_P. The ability to tune the resonant frequency with dc-bias can be very advantageous for micromechanical resonators and this phenomenon has been used for tunable filters and temperature compensation of resonator oscillators. From the plot of f_o vs. V_P in Figure

3.3 and using equations (3.10) and (3.12), linear mechanical stiffness k_m and effective mass m_{eff} for this CC beam is extracted as 3513.6 N/m and 1.05×10^{-10} kg, respectively.

From Figure 3.3, the quality factor of CC beam resonator is also dependent on dc-bias voltage, dropping from 5,500 to 4,000 over the measured V_P range. From the resonator model, the equation (2.15) indicates the dependence of Q on the effective spring constant (k_{eff}), that is, $Q = \frac{\sqrt{k_{eff} \cdot m_{eff}}}{\delta}$. Since the damping coefficient δ is inherently a mechanical property and not dependent on the electrical stiffness, measure quality factor can be expressed by

$$Q = Q_{nom}\left[1+\left(\frac{k_e}{k_m}\right)\right]^{1/2}, \tag{3.14}$$

where measured Q is the nominal quality factor (Q_{nom}) multiplied by a term that includes the electrical stiffness. Since the electrical stiffness is dependent on V_P, measured Q is also dependent on the dc-bias voltage. Also, the tuning effect of frequency and Q from equations (3.11) and (3.14) does not take into account of variations in actual gap d, W_e and h of electrode coming from fabrication process.

For Free-Free beam resonator design from Section 2.2.2, it is driven at the fundamental mode. Measured resonant frequency of FF beam resonator centers around 654kHz and it agrees well with Abaqus simulation result of 660.9kHz. The dependence of resonant frequency on V_P can be seen clearly from Figure 3.4. Measured Q of FF beam also varies with different V_P bias as in the case of CC beam resonator, and these data were measured at low v_{ac} to ensure linear mechanical motion. Figure 3.5 illustrates the Q plotted for different V_P, as well as the shift in f_o with V_P. The Q value dropped from 16,400 to 8,200 as V_P was increased from 20V to 80V, all measured in vacuum.

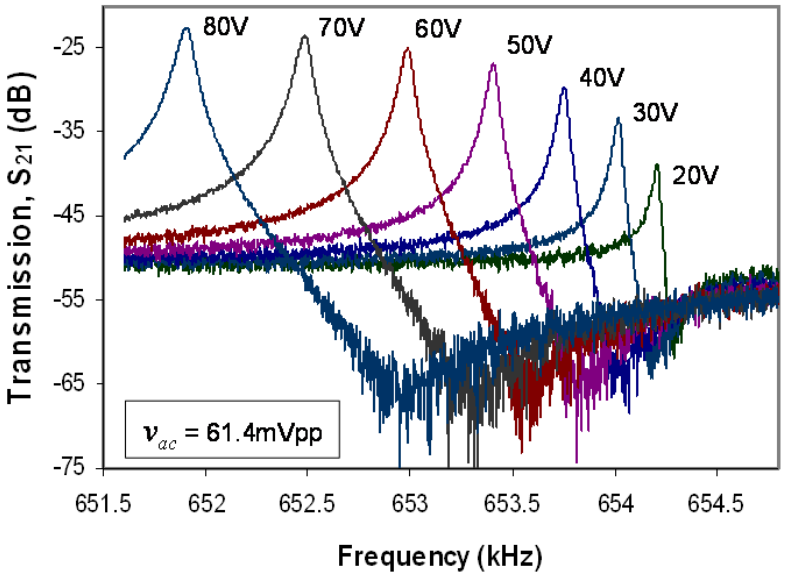

Figure 3.4: Measured transmission curves for different V_P bias at fixed v_{ac} of 61.4mVpp for fundamental-mode Free-Free beam resonator.

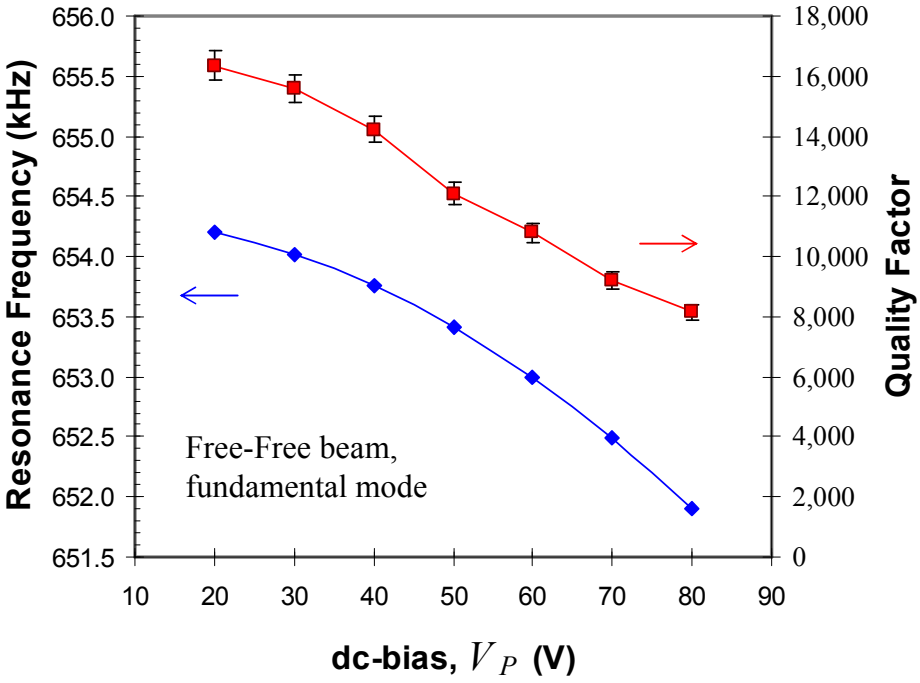

Figure 3.5: Plots of resonant frequency and Q vs. dc-bias V_P, showing their dependence on V_P for Free-Free beam resonator excited at fundamental mode.

Observed large reduction quality factor of about 50% cannot be explained only with Q variations due to dependence of electrical stiffness on V_P according to equation (3.14). The possible reason for this large decrease in Q, as suggested in [37], is likely due to enhanced energy transfer between middle beam and the support beams as the measured resonant frequency shifts from second-mode resonance of the supporting beams, eventually leading to larger losses through the anchors. Another factor that somewhat contributes to the decrease in Q is the measurement error. As shown in Figure 3.4, the gap between the anti-resonance and the resonance peaks gets nearer as V_P is decreased. Since the Q value is experimentally measured using 3dB bandwidth method, it tends to over-estimate the Q value when the anti-resonance is near the resonance peak.

The resonant frequency shift observed in Figure 3.5 due to negative spring softening with increased V_P can be expressed with equation (3.13). This spring softening effect takes into account of contributions from both drive and sense electrodes. The extracted linear mechanical spring constant k_m and effective mass m_{eff} from Figure 3.5 are 6624.9 N/m and 3.92×10^{-10} kg, respectively. The peak value of S_{21} transmission curve in Figure 3.4 on the other hand increases with increasing V_P, which is due to the dependence of resonator output sense current on V_P. Since the motional current from equation (2.24), $i_m = V_P \frac{\partial C}{\partial x}\frac{\partial x}{\partial t}$, is converted to voltage by transresistance amplifier and subsequently detected by network analyzer, changes in V_P corresponds to proportional changes in resonance peak of S_{21} transmission curve.

If we consider the second-mode Free-Free beam resonator presented earlier in Section 2.2.2, the Euler-Bernoulli's resonant frequency according to equation (2.4) is 572.82kHz and ANSYS-simulated f_o is 586.1kHz. The measured resonant frequency is about 10% lower at 530kHz due to process variations and also anchor region not fixed

exactly right the end of the support beams. Figure 3.6 presents the frequency response curve for the resonator with a dc-bias voltage V_P of 20V, ac drive of 130mVpp, and the Q is about 11,418. The resonator is driven and sensed in fully differential configuration outlined in [34], so that the anti-resonance is relatively far away even at 20V dc-bias. The transmission of the second-mode FF beam resonator is more symmetric than that of the fundamental-mode FF beam, and leads to more accurate Q measurement.

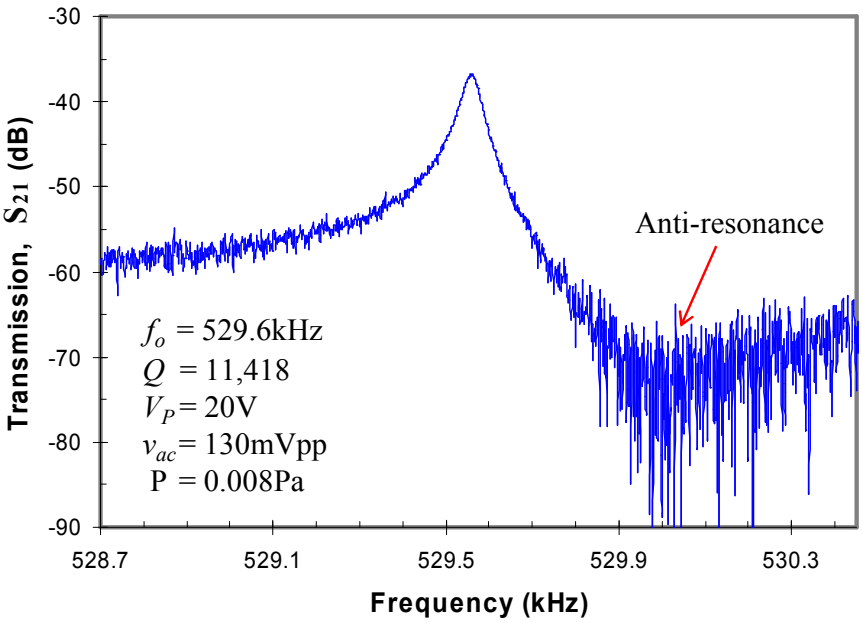

Figure 3.6: S_{21} response of second-mode Free-Free beam resonator that is differentially driven, measured Q is about 11,418 at V_P of 20V. Anti-resonance is away from the peak.

Figure 3.7 illustrates the V_P – dependence of both the resonant frequency and quality factor. Electrostatic spring softening that shifts f_o with increase in V_P observed here again can be explained with similar expression as equation (3.13), with total electrode area contributing from four electrodes. When linear mechanical stiffness and lumped effective mass is extracted from resonant frequency vs. V_P plot of Figure 3.7, k_m is 6277.8 N/m and m_{eff} is 5.67×10^{-10} kg.

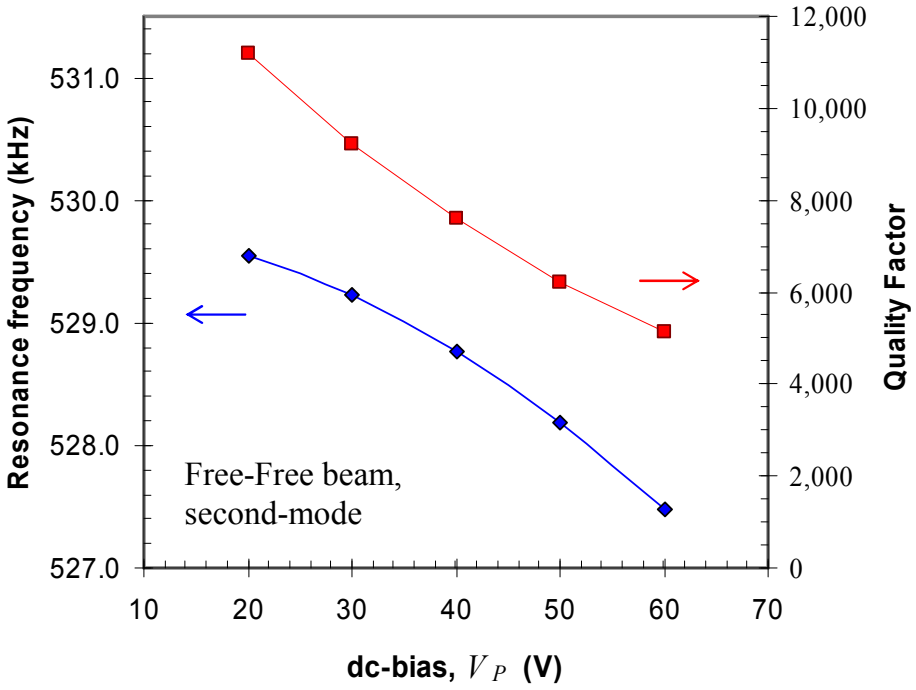

Figure 3.7: Plots of resonant frequency and Q vs. dc-bias V_P for Free-Free beam resonator differentially excited at second mode.

The quality factor reduction with increase in V_P from 20V to 60V is already more than 50%, similar characteristic as that of fundamental-mode FF beam, due to enhanced vibration energy losses through the support beams as the dc-bias is increased.

3.4.2 Bulk-acoustic-mode resonators

Bulk-mode single crystal silicon resonators tested that are in MHz frequency range reveal measured ultra-high Q's above one million. Performance of three different types of bulk-mode resonators are presented in this sub-section: Lamé-mode square resonator; wine glass mode disk resonator; and length-extensional resonator pair.

A square resonator was designed and fabricated to operate in Lamé mode, its mode shape simulated with finite element software, Abaqus, and a micrograph of the resonator is shown in Figure 3.8 with 60μm×10μm anchor. In this mode the edges of square plate bend in anti-phase while the plate volume is preserved. The length of the square edge is designed as 650μm. The anchor tether beams are placed at the nodal points of the mode, at the four corners of the square, as to minimize vibration energy losses through the support.

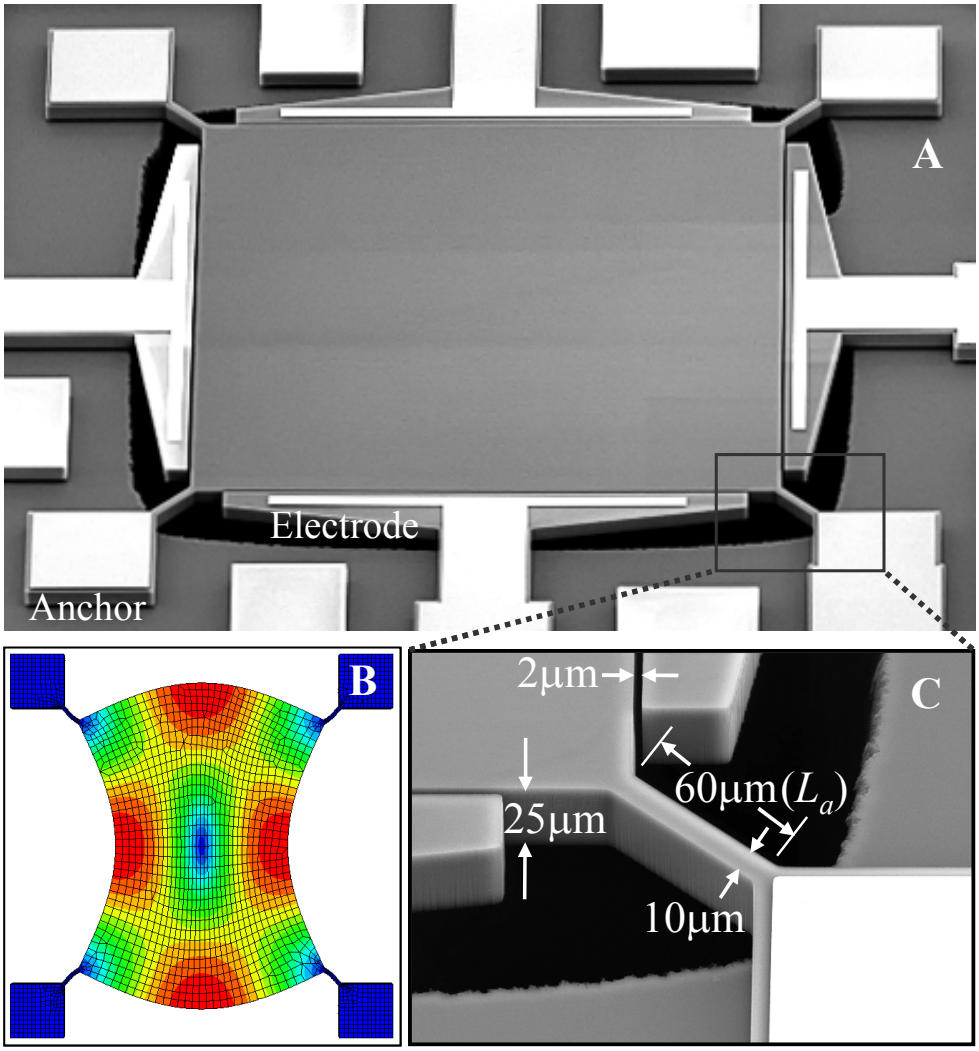

Figure 3.8: A) Micrograph of a Lamé-mode 650μm square resonator, B) Abaqus simulation of its mode shape, and C) zoomed-in view of anchor region.

Resonant frequency simulation from finite element software ANSYS is 5.94MHz using the material properties of SOIMUMPs process, E = 179GPa, ν = 0.29, and ρ = 2330 kg/m^3, which also matches with the calculated f_n based on combination of equations (2.7) and (2.8) from Section 2.2.4. The resonant frequency values predicted by above methods assume a thin square plate with isotropic material, and also calculated shear modulus according to equation (2.8) is 69.38GPa. However, the measured shear modulus C_{44} for single crystal silicon is 79.56GPa [73, 74]. Hence, resonant frequency value given by equation (2.7) using the measured C_{44} actually provides a better prediction for the measured resonant frequency of Lamé-mode square resonators of this work. Using the reported shear modulus, C_{44} = 79.56GPa, calculated resonant frequency is 6.357MHz, which matches very well with measured value of 6.353MHz shown in S_{21} transmission plot of Figure 3.9.

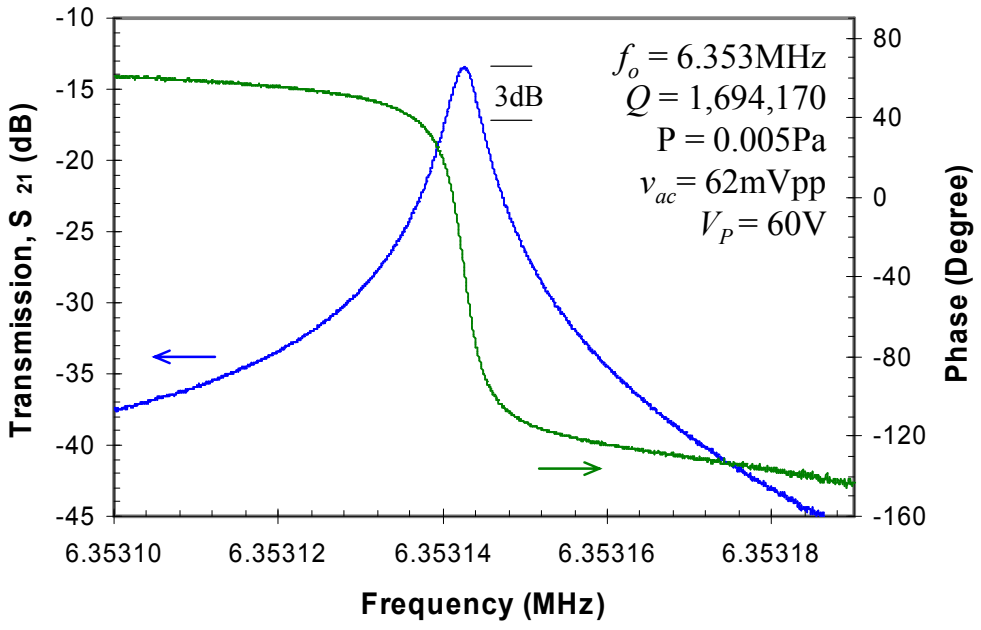

Figure 3.9: Measured transmission curve of 6.353MHz Lamé-mode square resonator, biased at 60V dc and 62mVpp ac drive. The Q measured is about 1.7million.

The measured quality factor is about 1.7million in vacuum pressure of 36μTorr, biased at V_P of 60V and 62mVpp ac drive. As can be seen from the Figure 3.9, the anti-resonance peak due to feedthrough parasitic capacitance is suppressed due to fully differential drive and sense electronics described earlier in Section 2.3.3. With the differential test setup, motional and feedthrough currents are drained at the resonator proof-mass node as the virtual ground, without charges passing through the anchors [34]. The corresponding phase plot in Figure 3.9 shows the expected sharp change in phase at resonance.

Disk resonators with different anchor designs shown in Figure 3.10 are tested for wine glass mode with measurement setup of similar differential drive architecture as that used for Lamé-mode square resonators, and a transmission plot is shown in Figure 3.11.

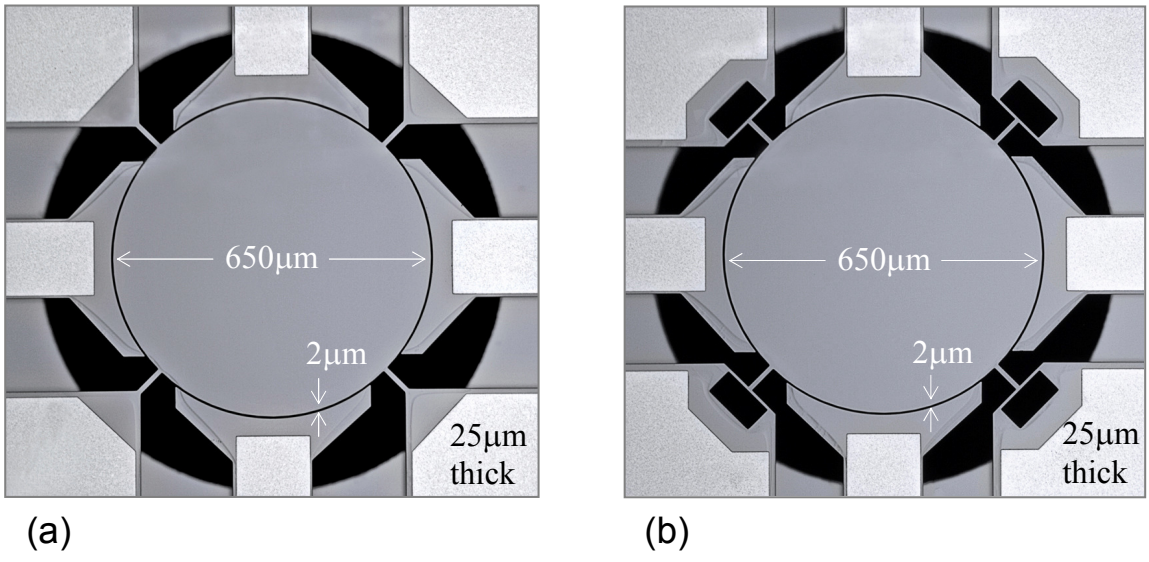

Figure 3.10: Micrograph of 6.8MHz wine glass disk resonators with different anchor geometry: (a) straight-beam anchor and (b) *T*-shaped anchor.

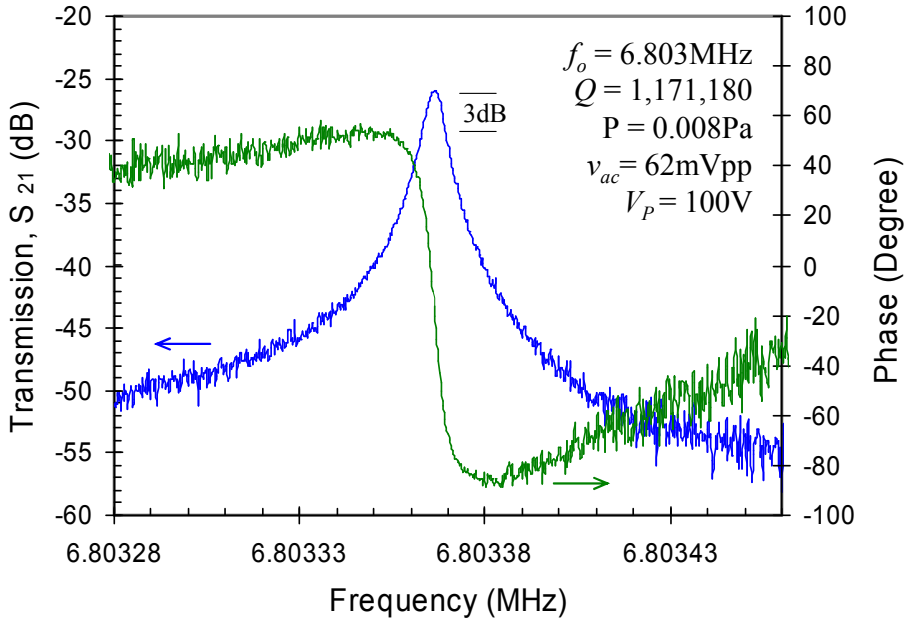

Figure 3.11: Resonance plot of 6.803MHz wine glass disk resonator with straight-beam anchors. Measured high Q is 1.17million, biased at 100V with low ac drive of 62mVpp.

The resonant frequency of 650μm–diameter disk resonator from Figure 3.10(a) with straight-beam anchor is measured at 6.803MHz with high Q of 1.17million, as shown in the transmission plot Figure 3.11. Resonant frequency according to the analytical equation (2.10) from Section 2.2.5 is 6.87MHz, which is within 1% of the measured value of 6.803MHz.

Another bulk-mode length-extensional resonator pair shown in Figure 3.12 is tested to have high Q as well with differential measurement drive method outlined in Section 2.3.3. Estimated resonant frequency for one length-extensional resonator with 600μm length according to equation (2.6) is about 7.3MHz, and the simulated value of entire dual-resonator structure in Abaqus is 7.22MHz. Both predictions are within 3% of the actual measure resonant frequency of 7.088MHz for the dual-resonator pair biased at V_P of 100V and 131mVpp ac drive.

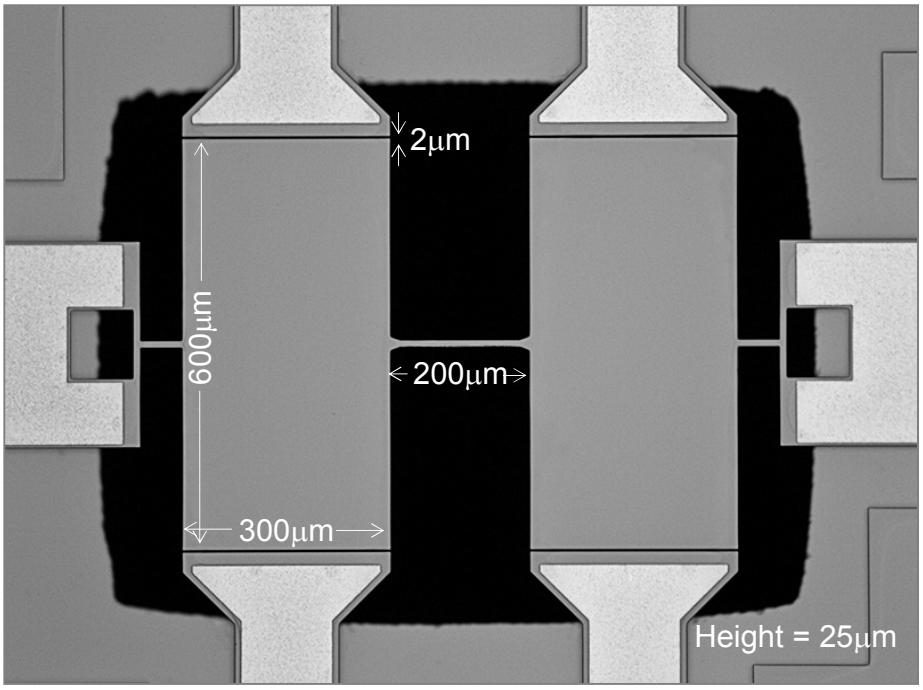

Figure 3.12: Micrograph of two adjoining length-extensional resonators with *T*-shaped anchor.

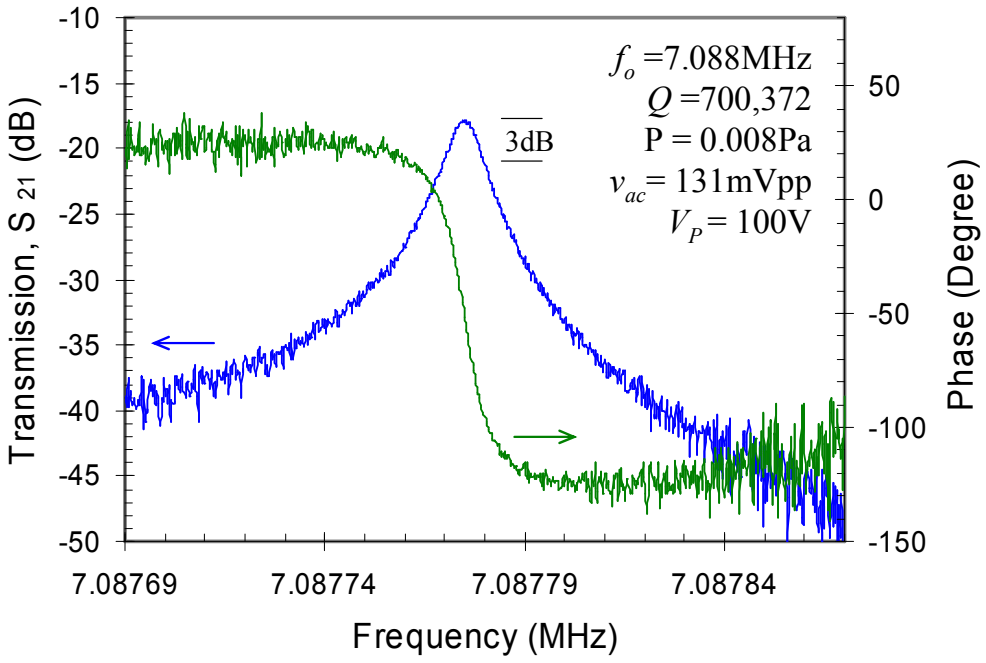

Figure 3.13: Transmission plot of differentially driven 7.088MHz length-extensional resonator pair with *T*-shaped anchors. The *Q* is 700,372 biased at 100V with 131mVpp ac drive.

The quality factor measured from S_{21} transmission plot shown in Figure 3.13 is about 700,372. The acoustic attenuation of longitudinal wave propagation in single crystal silicon along <100> axis is about 0.095dB/m at 10MHz [63]. Then the acoustic quality factor per unit wavelength according to equations (3.7) and (3.8) is about 480,420 per unit wavelength. Given the length-extensional resonator in Figure 3.12 is based on standing wave with $1/2\lambda$ wavelength, the Q_a should be doubled to 960,840. Hence the measured Q is about 73% of the predicted acoustic Q_a, which suggests that other energy losses such as anchor losses and surface losses are more dominant. Also, the acoustic Q_a serves as a measure of how good the anchor design of resonator with reduced vibration energy losses. The measured Q of length-extensional resonator is not more than one million as that of other disk and square bulk-mode resonators presented earlier at similar frequency range, which may be partly due to thermoelastic damping of longitudinal waves, whereas shear waves induce virtually no thermoelastic damping.

The acoustic attenuation of longitudinal and shear waves along <100> axis as a function of the temperature for silicon reported in [63] shows that amount of attenuation increases with temperature, and at room temperature the attenuation for longitudinal wave is about 3.6 times more than that for the shear wave along <100> direction. Since the acoustic quality factor (Q_a) is inversely proportional to the attenuation factor (α), according to equations (3.7) to (3.9), then Q_a estimate for the shear waves along <100> should be higher than that for the longitudinal waves. The attenuation of longitudinal and shear waves along <110> and <111> directions for silicon are listed in Table 3.2 and it is evident that acoustic attenuation in single crystal silicon depends on the direction of propagation.

Table 3.2: The acoustic attenuation of longitudinal waves and shear waves along <100>, <110>, and <111> directions in silicon at room temperature, units in (dB/m) normalized to 10MHz.

Type of acoustic wave	**Attenuation in (dB/m) at 10MHz along axis**		
	<100>	<110>	<111>
Longitudinal	0.0950	0.0705	0.0642
Shear	0.0265	0.1946 [a] 0.0279 [b]	n/a

[a] Polarization along $<1\,\bar{1}\,0>$ axis
[b] Polarization along $<001>$ axis
n/a = not available

The attenuation values in Table 3.2 are measured results from [63, 75, 76] at room temperature, converted to (dB/m) and normalized at 10MHz for fair comparison. From Table 3.2, the longitudinal waves propagate with the least amount of acoustic attenuation along <111> direction, so extensional resonators with acoustic waves propagating along this direction should perform with the best quality factor. Lamé-mode/wine-glass-mode resonators have mainly shear acoustic wave propagation and hence almost no contribution from thermoelastic damping and acoustic energy losses are mostly due to phonon-phonon interactions of Akhieser damping alone. Therefore, higher quality factor is expected for Lamé-mode square and wine glass disk resonators compared to the extensional resonators, and experimental results of this work are in good agreement with this expectation.

The attenuation of shear waves along <100> direction and that along <110> direction (polarized along <001> axis) are about the same with 0.027dB/m at 10MHz, which according to equation (3.9) gives the Q_a of about 2.72million per unit wavelength for 6.35MHz Lamé-mode square resonators and sets as the upper limit for achievable quality factor at room temperature. For the attenuation of shear waves along the <110>

direction, there are two possible polarizations of either along <1 $\bar{1}$ 0> axis or along <001> axis, and polarization along <1 $\bar{1}$ 0> has the highest attenuation of 0.195dB/m at 10MHz, even worse than the attenuation of longitudinal waves, so bulk-mode resonators based on shear waves along this direction should have much lower Q values. The acoustic Q_a values calculated in this way serve as a rough estimate of contributions mostly from Akhieser losses and somewhat from thermoelastic losses, and a more in-depth analysis can be found in [60-64, 72, 75-77]. N-type impurity doping of silicon, such as the case of structural material in SOIMUMPs process with phosphorus doping, further increases the attenuation of both longitudinal waves and shear waves to some extent [77], in general about 10% to 50% more attenuation than that in pure silicon.

One of the key attributes of bulk-acoustic-mode resonators is their high stiffness, that is, their spring constant k_m is much larger than flexural-type resonators. The benefit of this characteristic is high stability of resonant frequency and Q in response to fluctuations in dc-bias V_P. However, the drawback is that V_P cannot be used to tune the resonant frequency effectively. For example, measured resonant frequency shift and Q due to changes in V_P for a Lamé-mode square resonator, as shown in the Figures 3.14, suggest rather minor dependence on V_P bias. The trend of decreasing f_o due to electrostatic spring softening is still observed, but the shift is only 108Hz over the V_P range from 20V to 80V, and in parts per million (ppm) the change is only 17ppm over this V_P range. The mechanical spring constant k_m extracted from f_o vs. V_P plot of Figure 3.14 according to equation (3.11) is 1.89×10^7 N/m and m_{eff} is 1.19×10^{-8} kg. There is hardly any change in Q, reduced by only 26 or about 16ppm as V_P is increased from 20V to 80V in vacuum. The term m_{eff} here can be considered as a scaled version of the total static mass ($\rho \cdot L^2 h$) of square resonator.

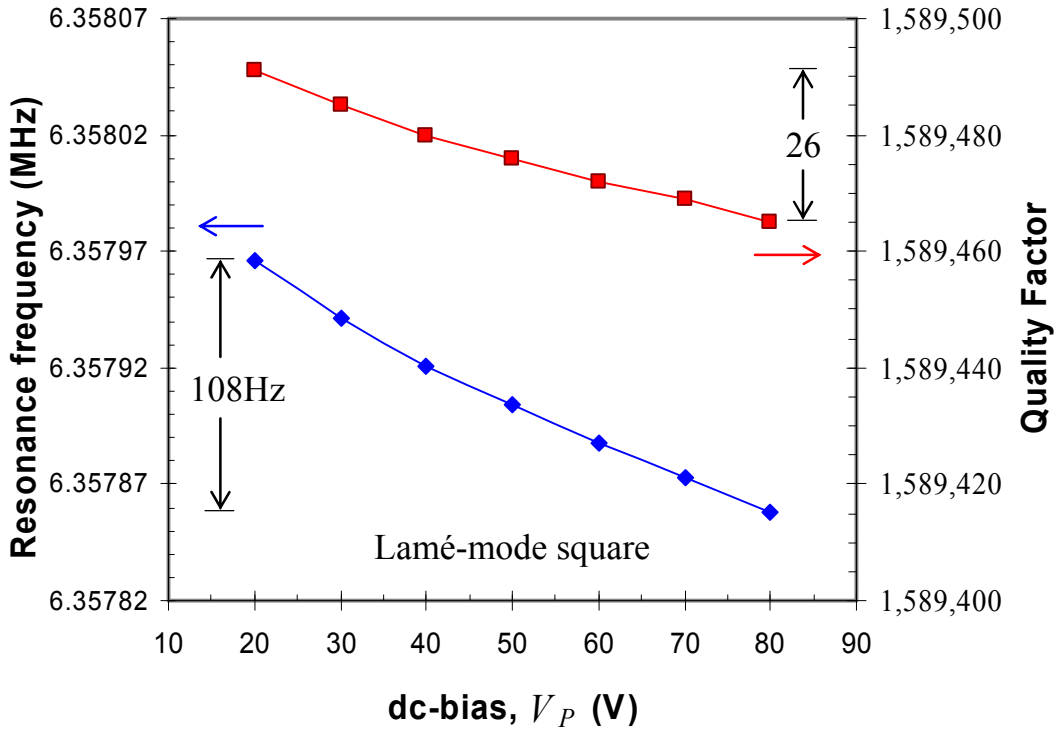

Figure 3.14: Changes in resonant frequency and quality factor with V_P increase for 6.35MHz Lamé-mode square resonator.

Moreover, Q reduction coming from ohmic losses of high resistive material, which otherwise could mask the inherent Q of the resonator, has been minimized mainly due to low resistivities of structural materials in SOIMUMPs process (Figure 2.19). Very little change in Q with V_P in low ppm values is also observed for disk resonators and length-extensional resonators presented in this work, which is the intrinsic characteristic of bulk-mode resonators with very high stiffness. In equation (3.14) the k_m term is too high that changes in k_e due to V_P tuning has very little effect. This almost constant Q property is unlike some of the flexural beam resonators where reduction in Q could be as much as 50% with V_P increase.

Measured values of quality factor, f_o–Q product, mechanical spring constant and effective mass for flexural-type beam resonators and bulk-acoustic-mode resonators of this work are listed in Table 3.3. High quality factor of bulk-mode resonators is clearly

Table 3.3: Resonant frequency, quality factor, ($f_o \times$ Q) product, mechanical spring constant, and effective mass of flexural-mode resonators and bulk-acoustic-mode resonators of this work.

Resonator design	f_o	Q	$(f_o \times Q)$	k_m **(N/m)**	m_{eff} **(kg)**
Clamped-Clamped beam	917.1kHz	4,059	3.72×10^{9}	3.51×10^{3}	1.05×10^{-10}
Free-Free beam, fundamental mode	654.2kHz	16,360	1.07×10^{10}	6.62×10^{3}	3.92×10^{-10}
Free-Free beam, second mode	529.6kHz	11,190	5.93×10^{9}	6.28×10^{3}	5.67×10^{-10}
Lamé-mode square	6.35MHz	1,694,170	1.08×10^{13}	1.89×10^{7}	1.19×10^{-8}
Wine glass disk	6.80MHz	1,171,180	7.97×10^{12}	3.44×10^{7}	1.88×10^{-8}
Length-extensional rectangle pair	7.09MHz	700,372	4.96×10^{12}	2.30×10^{7}	1.16×10^{-8}

evident from Table 3.3 in millions range and as a result, the f_o–Q product of the bulk-mode resonators is ~10^{12}–10^{13}, about three orders of magnitude higher than that of the beam resonators. Although measured Q of length-extensional resonator is not more than one million as that of other bulk-mode resonators, it is still much higher than that of flexural beam resonators. FF beam resonators have higher Q than CC beam resonator due to improved anchor geometry, and the k_m values of FF beams are around twice that of CC beam. High mechanical stiffness of bulk-mode resonators, k_m~10^7, is four orders of magnitude above the k_m values of the flexural beam resonators. The stiffness of wine glass disk resonator is 1.5 – 1.8 times higher than that of other bulk-mode resonators.

3.5 Quality factor dependence on structural geometry

In this section, the dependence of quality factor on the geometry of structural material will be explored for Lamé-mode square resonators with different number of straight-beam anchor supports, 10μm and 25μm structural layer thickness, as well as the effect of etch-hole release on the quality factor.

One of the major challenges of interfacing micromechanical resonators directly with RF electronic circuits is their large series motional resistance (R_m). Motional resistance of a capacitively driven-and-sensed parallel-plate resonator as derived earlier in equation (2.26) can be expanded as

$$R_m = \frac{\sqrt{k_{eff} m_{eff}} \cdot d^4}{Q \cdot \varepsilon^2 A_e^2 V_P^2}, \tag{3.15}$$

where d is the electrode-to-resonator gap, A_e is total effective gap area, ε is the permittivity, and V_P is the dc polarization voltage biased to the resonator. Therefore, R_m can be reduced by decreasing the electrode-to-resonator gap, increasing the dc-bias V_P, increasing the permittivity by replacing the air gap with solid dielectric material, increasing the area of the electrode overlap region, or mechanically-coupling identical arrays of resonators [59]. In addition, an innovative gap reduction technique based on structural geometry as in [78] can also be done to achieve sub-micron capacitive gaps. Higher mechanical Q due to improvements in resonator design will also lead to reduction in R_m. Moreover, as will be discussed in Section 3.6, R_m is also related to the dimension of anchor beams attached to the resonator.

Therefore, understanding of how R_m is affected by the number and the type of anchor supports attached to the resonator will be useful. The thickness of the structural

layer varies between different fabrication processes. A thinner structural layer results in a reduction in electrode area, which translates to higher motional resistance but its impact on the Q value is less understood. For some surface micromachining processes, the need for etch-hole release is unavoidable, so the effect of etch holes on the performance of bulk-acoustic-mode will be very useful for resonator design in such processes. The focus of this section is to investigate the influence of geometry parameter variations on the Q and R_m values of micromechanical Lamé-mode square resonators.

3.5.1 The number of anchors

As discussed earlier in Section 3.3, for Lamé-mode square resonators in vacuum with negligible air damping, anchor losses are most likely the dominant loss mechanism governing the overall quality factor. Therefore from intuition, reducing the number of anchors should improve the Q of resonator. However, the anchor beams are placed at nodal points that have minimum displacement and they are needed to properly hold the resonator in place as it vibrates at resonance. A disk resonator with 29.4μm diameter and 3μm thickness, which has only one anchor beam supporting, has been reported in [65] to function well in vacuum without interference with electrodes. For such small devices, one anchor tether may be sufficient to hold the resonator in place. However, for 650μm square resonators with only one anchor beam at the square corner, it was tested to be inadequate to set the square resonator into resonance. This is possibly due to swaying lateral motion that eventually leads to stiction of the square plate with the electrodes, and consequently shorting the dc-bias voltage of resonator-mass to ground.

For two anchors supporting the square resonator, there are two possible arrangements: two opposite anchors or two adjacent anchors. The square resonator with four anchors shown in Figure 3.8 is named design 3A, the resonators with only two anchors are named design 3B and 3C, and micrographs are shown in Figure 3.15.

Resonator Design	**Anchor length, L_a (μm)**	**Anchor width, W_a (μm)**	**Thickness (μm)**
3A (4 anchors)	60	10	25
3B (2 opp. anchors)	60	10	25
3C (2 adj. anchors)	60	10	25

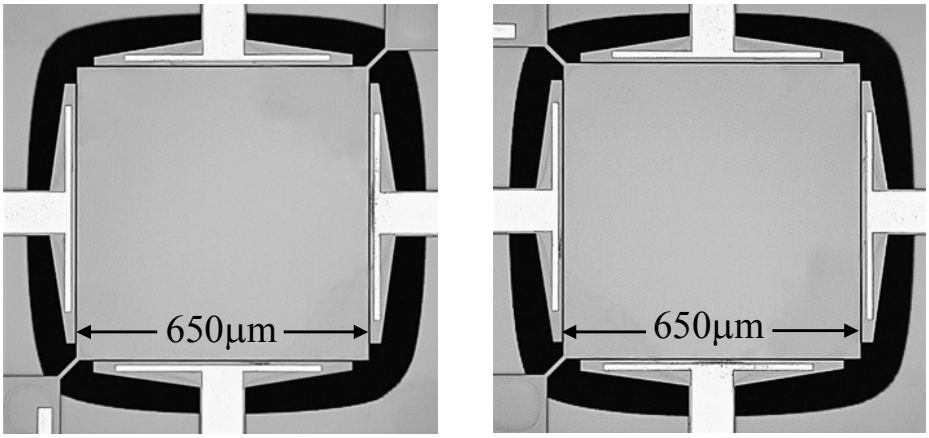

Design 3B – *opposite anchors* Design 3C – *adjacent anchors*

Figure 3.15: Dimensions of resonator designs 3A, 3B, 3C, and micrograph of square resonators with two opposite anchors and two adjacent anchors.

The dimension of anchor beams are length L_a = 60μm and width W_a = 10μm for all three devices, and the structural layer is also the same with 25μm thickness. The transmission plots measured for devices 3A, 3B and 3C are shown in Figure 3.16 for V_P of 60V and low ac drive of 62mVpp. Since the resonant frequency of each of the devices is different due to design and process variations, the transmission plots are normalized to f_o over 100Hz span. From Figure 3.16, motional resistance (R_m) can be extracted from the peak value of S_{21} plot, namely the insertion loss (IL) of transmission.

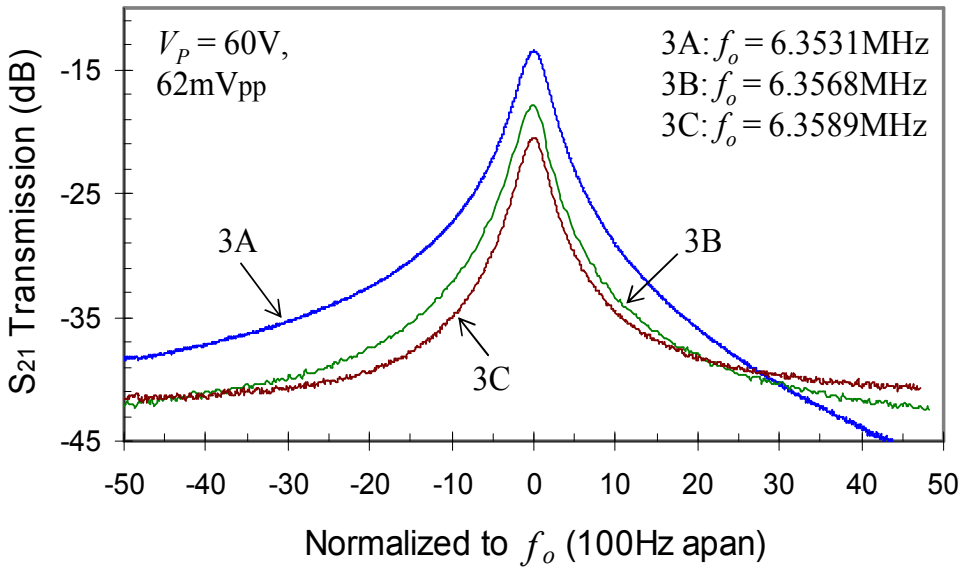

Figure 3.16: Measured S_{21} transmission of device 3A with four anchors, device 3B with two opposite anchors, and device 3C with two adjacent anchors.

If the output port of the resonator is directly terminated with 50Ω load of the network analyzer, the equivalent motional resistance of resonator [79] can be extracted

$$R_m = 50 \times 10^{-\frac{IL}{20}}, \tag{3.16}$$

where *IL* is the peak value of the frequency response S_{21} plot in decibel (dB). However, if the output current is too small with large electrode-to-resonator gap (for example, 2μm gap of SOIMUMPs process), a transresistance amplifier is required to convert the output current to voltage with some gain, as shown in the measurement setups of Figure 2.15 and Figure 2.16. In transresistance amplifier setup there are feedback capacitance C_F and resistance R_F in parallel arrangement. Then, the measured R_m can be extracted by replacing the 50Ω in equation (3.16) with parallel combination of C_F and R_F as follow

$$R_m = \left| \frac{1}{j2\pi f_o C_F} \| R_F \right| \times 10^{-\frac{IL}{20}}. \tag{3.17}$$

Using equation (3.17) the motional resistance of devices 3A, 3B and 3C can be extracted from transmission plots of Figure 3.16. Table 3.4 lists the resonant frequency, Q and R_m of all three resonator designs.

Table 3.4: Resonant frequency, quality factor and motional resistance of Lamé-mode square resonators with different number of anchors.

Resonator design	f_o **(MHz)**	**Quality factor**	R_m **(kΩ)**
3A (4 anchors)	6.3531	1.67×10^6	78.9
3B (2 opposite anchors)	6.3568	1.77×10^6	98.0
3C (2 adjacent anchors)	6.3589	1.78×10^6	133.2

Square resonators with only two anchors, designs 3B and 3C, give slightly higher Q than the design 3A with four anchor supports. Energy dissipation through the anchor support is lower with only two anchors and it is expected to result in higher Q. However, designs 3B and 3C have higher R_m values than the four-anchored design 3A, which is most likely due to the asymmetry of having only two anchors. In addition, the two free ends are able to rotate and sway laterally, thus leading to uneven vibrations. Design 3C with two adjacent anchors is more asymmetric than design 3B with two opposite anchors, and consequently results in design 3C with higher R_m than design 3B. Even though energy dissipation is lower with slightly better Q for resonators with only two anchors, more symmetric design with four anchors can provide lower motional resistance and still maintain high quality factor.

3.5.2 Structural layer thickness

The thickness of the structural layer for MEMS resonators varies between different fabrication processes. A thinner structural layer results in a reduction in electrode area, which translates to higher motional resistance but its impact on the Q value is less understood. The focus of this section is to investigate the influence of structural thickness on the quality factor and motional resistance of bulk-acoustic-mode Lamé square resonators.

Measured results of resonant frequency, quality factor and motional resistance for two Lamé-mode square resonators with different thickness are listed in Table 3.5. The thickness of top silicon layer for design 3A is 25μm and that of design 3D is 10μm.

Table 3.5: Resonant frequency, quality factor and motional resistance of Lamé-mode square resonators with different structural layer thickness.

Resonator design	f_o **(MHz)**	**Quality factor**	R_m **(kΩ)**
3A (25μm thickness)	6.3531	1.67×10^6	78.9
3D (10μm thickness)	6.3464	1.08×10^6	135.5

Figure 3.17 shows the measured S_{21} transmission plots of designs 3A and 3D, taken at DC of 60V and 62mVpp AC drive, which clearly show that design 3D with thinner structural layer has lower Q value, which is 65% of the Q obtained for design 3A. The thinner structural layer in design 3D allows interference from other nearby out-of-plane resonance modes of the square resonator increasing the overall energy losses. Design 3D also has smaller electrode area (A_e) compared to design 3A, which also leads

to higher R_m. The combined effect of lower Q and smaller electrode area results in design 3D having roughly 1.7 times higher motional resistance than design 3A.

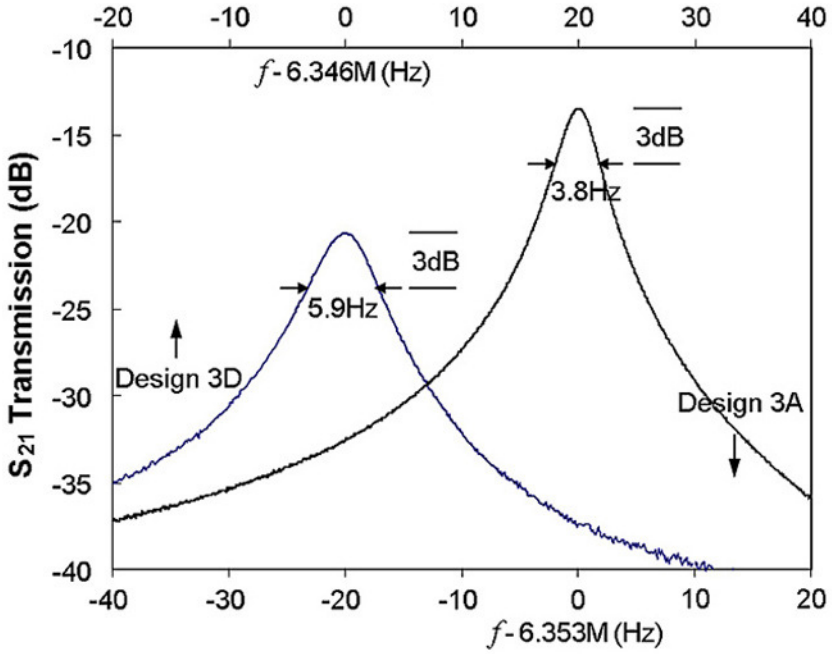

Figure 3.17: Measured S_{21} transmission plots of designs 3D and 3A with same measurement setup (resonators have different structural thickness of 10μm (3D) and 25μm (3A)).

3.5.3 Bulk mode and release etch holes

Sometimes in the fabrication process, etch holes are required in order to release the structural layer of micromechanical devices. Etch-hole step to release the resonator from substrate is an important step in surface micromachining process. For SOI bulk micromachining process such as SOIMUMPs where backside release etching is possible, etch holes may not be necessary to release the structural layer. Nevertheless, understanding of how etch holes affect the performance of different types of resonators

is invaluable information. For flexural clamped-clamped beam resonators for example, carefully placed etched slots could actually improve the device performance by reducing the thermoelastic damping and enhance the quality factor [71].

Although the effect of release-etch holes on the mechanical properties (such as tensile stress and Young's modulus) of structural material have been reported in [80-81], they have not investigated how the quality factor of resonator is affected by etch holes. Our group has reported on the effect of etch holes on the quality factors of Lamé-mode micromechanical square resonators in [82], which also includes that the Q actually depends on the location of etch holes on the resonator.

The square resonator design 3E shown in Figure 3.18 has $10\mu m \times 10\mu m$ square etch holes that are 30μm apart evenly placed all over the resonator. Other geometric dimensions of design 3E are the same as that of solid square design 3A from Figure 3.8. Measured S_{21} transmission plots of designs 3E and 3A under the same drive conditions are shown in Figure 3.19.

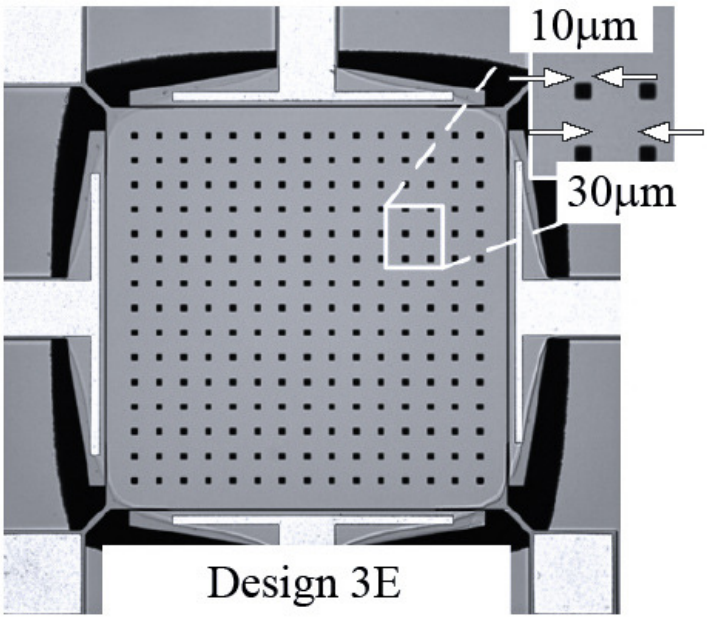

Figure 3.18: Square resonator design 3E with etch holes evenly placed all over the resonator.

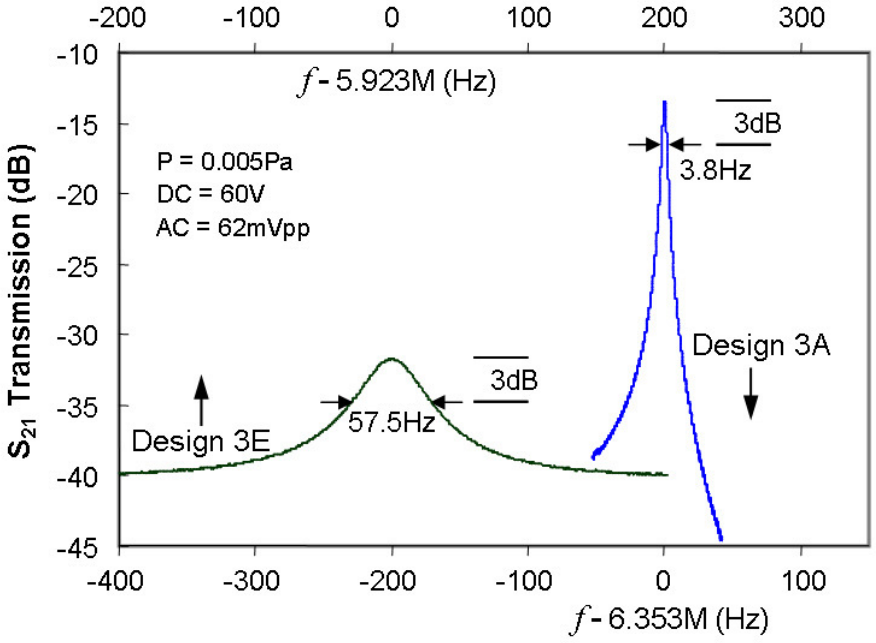

Figure 3.19: Measured S_{21} plots of designs 3E (with etch holes) and 3A (without etch holes) under the same measurement setup.

As can be seen in Figure 3.19 the quality factor of design 3E is 103,012, which is more than an order of magnitude lower compared to 1.67million of design 3A. This severe reduction in Q can be attributed primarily due to interference between the bulk acoustic wave propagation and the etch holes, and partly due to energy losses through the movement of anchor beams [82]. Experimental results of other identical square resonators with etch holes placed at various locations (center, middle edge, and corner) conclusively show that etch holes decrease the Q by more than an order of magnitude regardless of the location of etch holes. Furthermore, the Q of the Lamé-mode square resonator also depends on the location of etch holes. Etch holes placed at the square corners, where displacement is smaller at resonance, can provide better Q compared to etch holes placed at centre or middle edge. If etch holes are inevitable in such processes as in surface micromachining, the results reported in [82] could serve as useful guidelines for maximizing the Q even in the presence of etch holes.

3.6 Square resonators with straight-beam anchors

This section investigates how geometric sizing of straight-beam anchors affect the quality factor of Lame-mode square resonators. For the square resonators reported in this section, the length of the square edge of the resonator is fixed at 650μm to give approximately the same resonant frequency for different anchor designs. Four identical straight anchor beams are placed at four corners of square resonator. Ten different combination of length (L_a) and width (W_a) of anchor beams are tested, as listed in Figure 3.20, and structural thickness is fixed at 25μm for all the designs.

Design	L_a (μm)	W_a (μm)
3F	48	10
3A	60	10
3G	100	10
3H	120	10
3I	320	10
3J	60	20
3K	80	20
3L	100	20
3M	160	20
3N	230	20

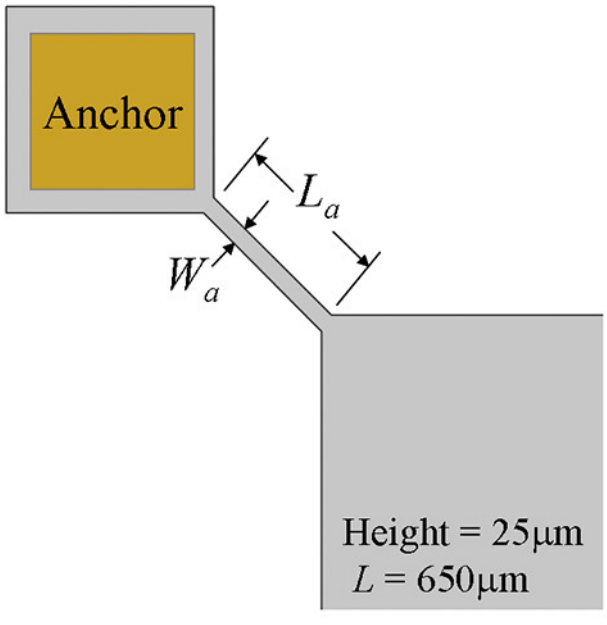

Figure 3.20: Schematic of anchor support and dimensions of anchor beams investigated, where identical anchors are placed at all four corners of the square resonator.

Given the lateral movement of the Lamé mode, the anchor beam can be considered as a vibrating cantilever beam (clamped-free beam) at resonance under shear stress. The beam's edge at the square end is in tilting motion caused by rotational shift

of the square corner. As outlined in analytical derivation for Q of disk resonators in bulk-mode [69], where anchors are under shear stress due to lateral vibrations of the resonator, Q is directly proportional to $(L_a/W_a)^6$, but inversely proportional to 8th power of *mode constant* (β). The term β is related to the mode shape of the anchor beam considered as cantilever, and β increases with higher mode order of anchor beam. For different anchor beam lengths, the beam vibrates in cantilever mode order at a frequency that is approximately at f_o of disk resonator. Hence according to the model, an increase in Q by making anchor beams longer and thinner is somewhat offset by Q reduction due to increase in mode order of the beam. In the snapshot diagram of anchor area from finite element simulation of square resonators in Abaqus is shown in Figure 3.21.

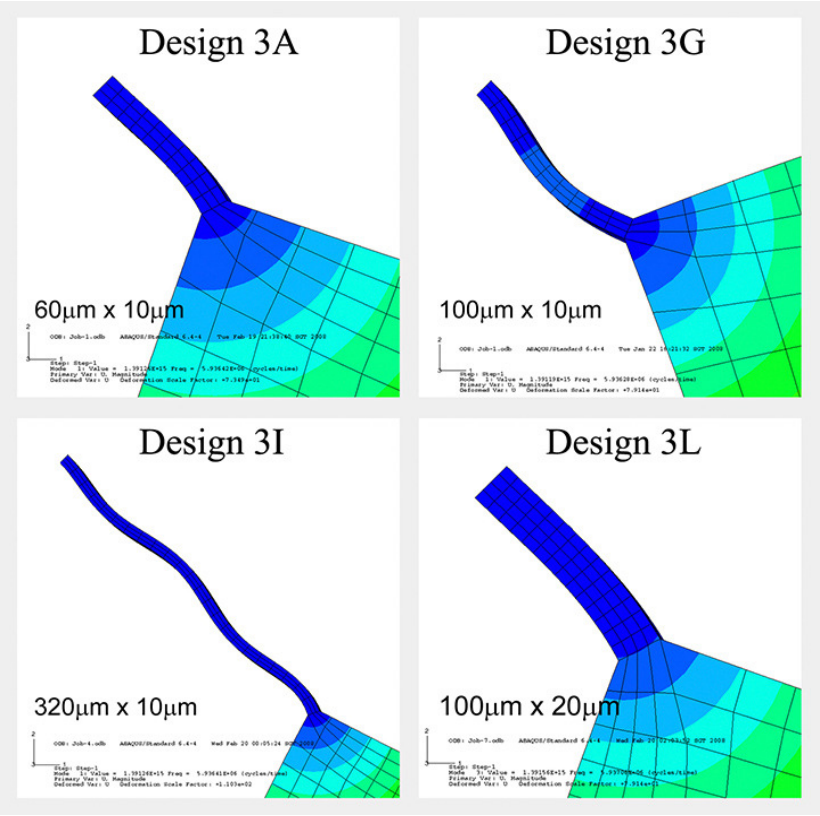

Figure 3.21: Cropped snapshot of anchor area from Lamé-mode simulation of squares with different anchor designs in Abaqus, where the anchor beam is fixed at one end. For short beams, its vibration resembles first or second normal mode of cantilever resonance, whereas longer beams vibrate close to or at higher orders of normal mode.

For designs 3A, 3G, 3I and 3L, simulation indicates that anchor beams vibrate with mode shape close to or at normal modes of cantilever resonance (f_{anchor_beam}). The exact shape of beam vibration depends on the dimension of anchor beam and the natural resonant frequency of the square bulk resonator. For short and stiff anchor beams, the mode shape is expected to be similar to 1st or 2nd order of cantilever resonance, whereas for longer and more flexible beams it will vibrate close to 3rd, 4th, or 5th order of normal resonance mode. Similar observations were made from the simulation results of the rest of ten anchor designs.

Based on experimental observations, when Lamé-mode square resonator is operated in high vacuum, Q value is limited by other loss mechanisms and not due to air damping, and anchor losses through support is considered as the Q-limiting factor. Therefore, ten anchor beam designs listed in Figure 3.20 with different length and width are examined for their overall performance. For a beam used as anchor, variable dimensions are length (L_a) and width (W_a) of the beam that will change the stiffness and flexibility of the support. Our main objective is to determine possible set of values for L_a and W_a so that performance of square resonator is optimum in terms of Q, power handling, motional resistance, and structural stability (that is, no stiction, pull-in, or breakage). Table 3.6 lists the resonant frequency, quality factor, motional resistance and effective stiffness (k_{eff}) of all ten designs measured under high vacuum, under the same condition of 60V V_P and 0.42Vpp AC drive. The effective spring constant k_{eff} values in Table 3.6 are derived from measured results, and calculations are based on combination of equations (3.10) and (3.15). For fair comparison, resonators are designed with similar resonant frequency f_o of about 6.35MHz, and all other test setup and drive conditions maintained to be as similar as possible.

Table 3.6: Measured resonant frequency, Q value, motional resistance and effective spring constant of Lamé-mode square resonator designs. The resonant frequency values for f_{anchor_beam} in the last two columns are simulated normal mode of resonance for a cantilever beam, which are nearby the f_o of the square resonators.

Anchor Design $L_a(\mu m) \times W_a(\mu m)$	f_o **(MHz)**	**Quality Factor**	R_m **(kΩ)**	k_{eff} **(MN/m)**	f_{anchor_beam} **(MHz) (mode)**	
3F (48 × 10)	6.35415	1.713×10^6	61.4	15.4	6.1 (1st)	32.2 (2nd)
3A (60 × 10)	6.35315	1.671×10^6	78.9	19.3	3.9 (1st)	21.9 (2nd)
3G (100 × 10)	6.35424	1.717×10^6	96.2	24.1	1.4 (1st)	8.5 (2nd)
3H (120 × 10)	6.35408	1.318×10^6	88.7	17.1	6.0 (2nd)	16.1 (3rd)
3I (320 × 10)	6.35275	1.217×10^6	120.7	21.5	4.7 (4th)	7.6 (5th)
3J (60 × 20)	6.35396	1.221×10^6	109.8	19.6	7.4 (1st)	33.6 (2nd)
3K (80 × 20)	6.35227	1.477×10^6	61.3	13.2	4.3 (1st)	21.7 (2nd)
3L (100 × 20)	6.35353	276,240	463.2	18.7	2.7 (1st)	15.0 (2nd)
3M (160 × 20)	6.35345	1.427×10^6	58.4	12.2	6.4 (2nd)	16.6 (3rd)
3N (230 × 20)	6.35460	1.412×10^6	75.4	15.5	3.2 (2nd)	8.6 (3rd)

Designs 3F, 3A and 3G with different anchor beam lengths and same width of 10μm all perform well, and have very high Q values of about 1.7million. At first when considering the motional resistance (R_m) values alone for devices (3F, 3A, 3G, 3H and 3I) with increasing anchor beam length, there appears to be a trend of increasing R_m value, and that R_m is partly dependent on anchor beam length. However, motional resistance (R_m) is inversely proportional to Q, according to equation (3.15), so reduction in Q will also lead to increased motional resistance. When anchor beam length L_a is 320μm long for design 3I, measured Q is reduced to 72% of designs 3F, 3A and 3G. The Q of design 3I comes down to 1.22million and R_m is increased accordingly. For design 3I, soft and flexible long anchor beams probably allow interference from nearby out-of-plane modes of the square resonator.

As listed in Table 3.6, the resonator designs with anchor width of 20μm have marginal drop in Q compared to square resonators with 10μm anchor width. Comparing designs 3A and 3J, when anchor width of design 3J is doubled for all four anchors, Q of design 3J is about 73% that of design 3A and consequently motional resistance is increased to 1.4 times as well. Designs 3K, 3M and 3N all have similar performance with Q values of about 1.4million. Given roughly the same Q, the R_m values for designs 3K, 3M and 3N are expected to be similar. However, variation in measured R_m values for these devices indicates that motional resistance may be weakly dependent on anchor beam length, and that R_m variation is in a narrow range of values. Moreover, for the same beam width W_a there is a range of beam length L_a values for which Lamé-mode resonator performs well.

Design 3L has unusually high motional resistance of 463.2kΩ with much lower Q of 276,240, which was observed for repeated tests with multiple devices from different dies. This performance of low Q and high R_m values is believed to be due to increased energy losses through the anchors. Further investigation needs to be done to verify this low Q using CAD tools such as COMSOL Multiphysics software to determine the nature of anchor losses. In addition, significant reduction in Q of design 3L leads to considerable increase in motional resistance. If the Q of design 3L had been above one million, motional resistance would have come down significantly from current 463.2kΩ. Therefore, Q directly influences the motional resistance, and that motional resistance is weakly dependent on dimensions of anchor beam.

The values in the last two columns under f_{anchor_beam} of Table 3.6 are the simulated cantilever mode frequencies neighbouring f_o (6.35MHz) of the square resonator for the given anchor beam dimension. The term in brackets (mode) is the order

of normal cantilever mode for the given anchor beam. The idea is to observe whether matching f_o with a normal mode frequency of the anchor beam considered as a cantilever (clamped–free beam) has any effect on performance of the resonator. Designs 3F, 3H and 3M were designed with nearly matching frequencies between the first or second cantilever mode of the anchor beam and f_o of the square resonator. Based on observed results, although the devices performed relatively well, there is no strong correlation between the overall performance and how well these frequencies match.

3.7 Advantage of *T*-shaped over straight-beam anchor

Losses through anchor support are observed to be major mechanism limiting the quality factor of bulk-mode micromechanical resonators. Therefore, optimized anchor design with minimum losses would lead to resonators with enhanced quality factor. Bulk-mode resonators with straight beams as anchors have been shown to perform well with very high quality factor. As the resonator is scaled to higher frequencies, improvement in anchor geometry is desired to further minimize the anchor losses.

In this work, *T*-shaped anchor geometry has been observed to be better than straight-beam anchor design in terms of reducing energy losses for Lamé-mode square resonators and also for length-extensional rectangular resonators. We have reported the advantage of *T*-anchor design over straight-beam anchor in [67] as the double in Q for 12.9MHz Lamé-mode square resonators. Moreover, as reported in [83], 7MHz length-extensional resonators with *T*-shaped anchors result in lower motional resistance and six times higher Q than that achieved with straight-beam anchors.

3.7.1 12.9MHz Lamé-mode square resonators

In this sub-section, two 12.9MHz Lamé mode square resonators with straight-beam anchor and *T*-shaped anchor designs are investigated. Their mode shapes simulated with Abaqus and micrographs of the resonators are shown in Figure 3.22 and Figure 3.23.

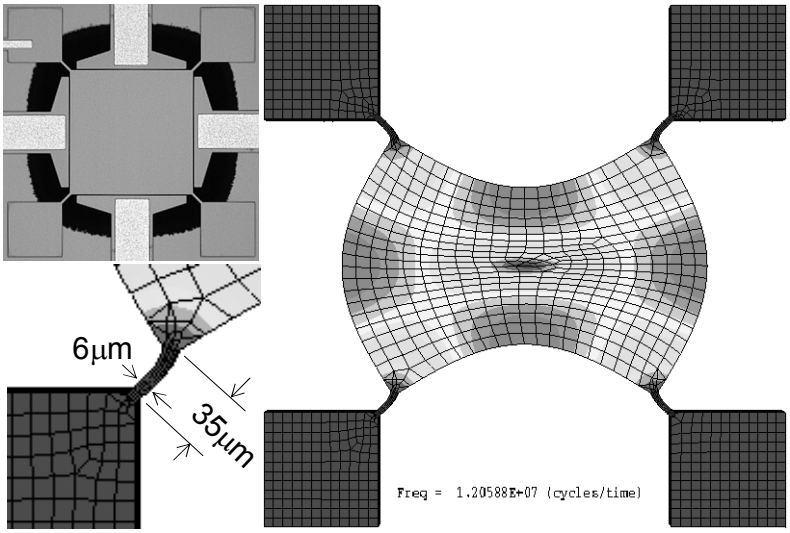

Figure 3.22: Micrograph of 12.9MHz square resonator with straight-beam anchor, Abaqus simulation of Lamé mode and anchor dimensions.

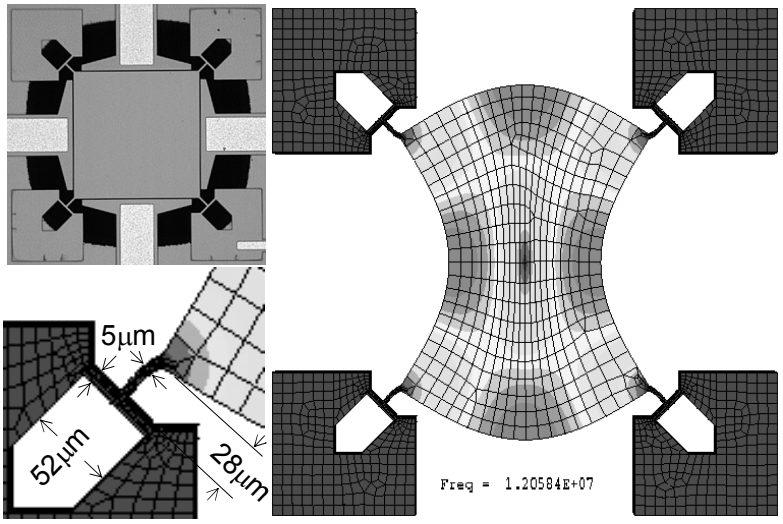

Figure 3.23: Micrograph of 12.9MHz square resonator with *T*-shaped anchor, Abaqus simulation of Lamé mode and anchor dimensions.

The length of the square edge is designed at 320μm. The anchor tether beams are placed at the nodal points so that there is a minimum energy loss through the anchors. The measured S_{21} transmission curves of differentially-driven square resonators with straight-beam anchor and *T*-shaped anchor are shown in Figure 3.24 and Figure 3.25, respectively. The absence of anti-resonance peaks is clearly evident from these figures. The resonant frequencies of both resonators are around 12.91MHz.

An increase in *Q* value from 404,000 for the square resonator with straight-beam anchor to a *Q* value of about 800,000 for that with *T*-shaped anchor was observed even though the resonators were operated under the same driving conditions at 100V DC and 130mVpp AC drive. This difference in *Q* value is most likely due to variation in energy losses through two different anchor designs. Since the pressure was maintained at a relatively low value of about 36 μTorr, measured *Q* value is not in the pressure-limited regime and not influenced by air damping.

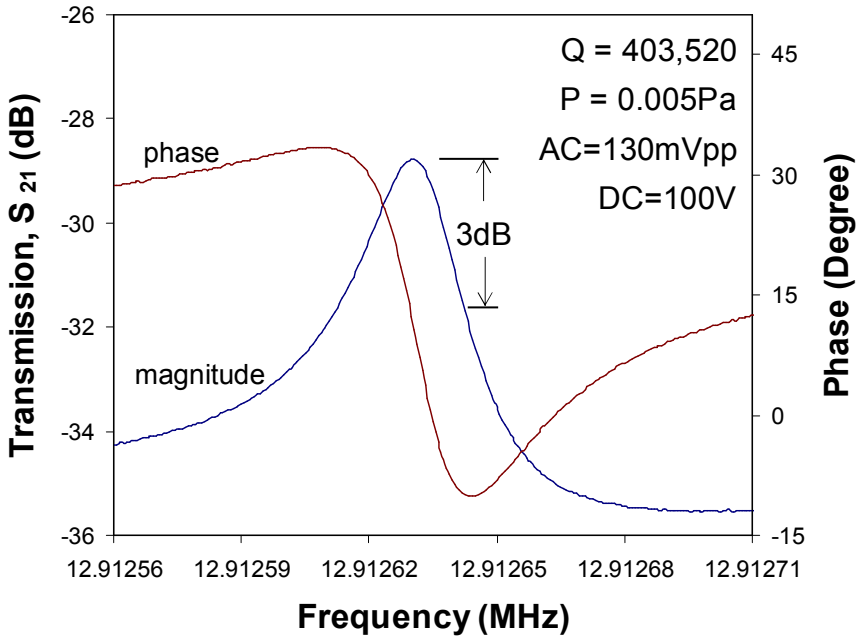

Figure 3.24: Measured transmission curve of 12.912MHz Lamé mode square resonator with straight-beam anchor, biased at 100V DC and 130mVpp AC. Measured *Q* value is 403,520.

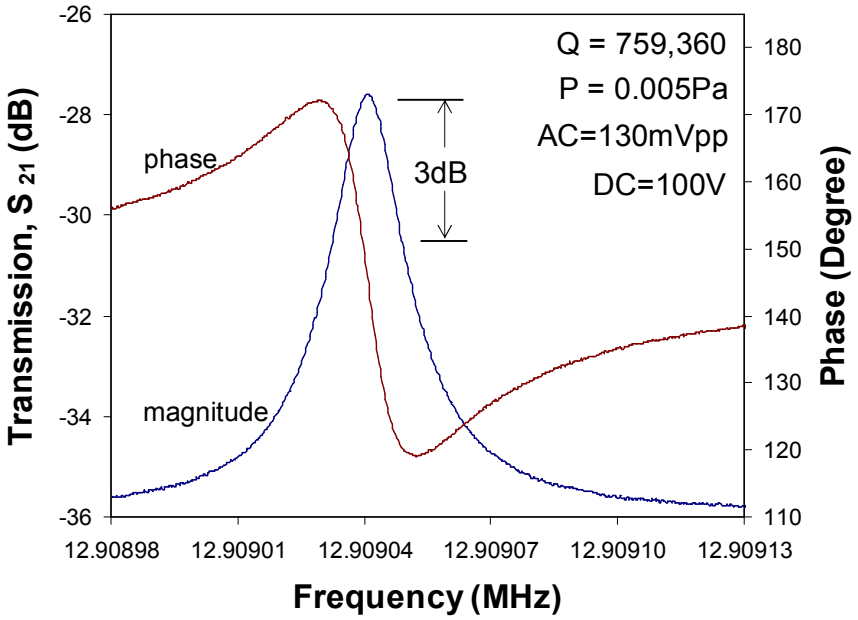

Figure 3.25: Measured transmission curve of 12.909MHz Lamé mode square resonator with *T*-shaped anchor, biased at 100V DC and 130mVpp AC. Measured *Q* value is 759,360.

The rotational tilting motion that the anchor experiences at the nodal point of Lamé mode is shown in Figure 3.26. For the *T*-anchored resonator, the middle beam attached to the square corner has more freedom to move. Whereas for the straight-beam anchor, one end of it is attached to the square corner while the other is fixed, leading to higher energy loss through the anchor. When the displacement simulation of *T*-anchored resonator was examined carefully, lateral movement of the adjacent beam that forms the "*T*" shape can be seen, as indicated in Figure 3.26. This relieves the shear stress and provides more freedom at the nodal point of the square resonator and believed to have reduced the stresses introduced by the rotational tilting motion of the square corner. For the square resonator with straight-beam anchor, the vibration energy is propagated directly through the fixed part of the anchor support, which means less freedom for the anchor beam and energy losses are higher. Hence, there are increased energy losses through the straight-beam anchor of the resonator resulting in lower *Q* value.

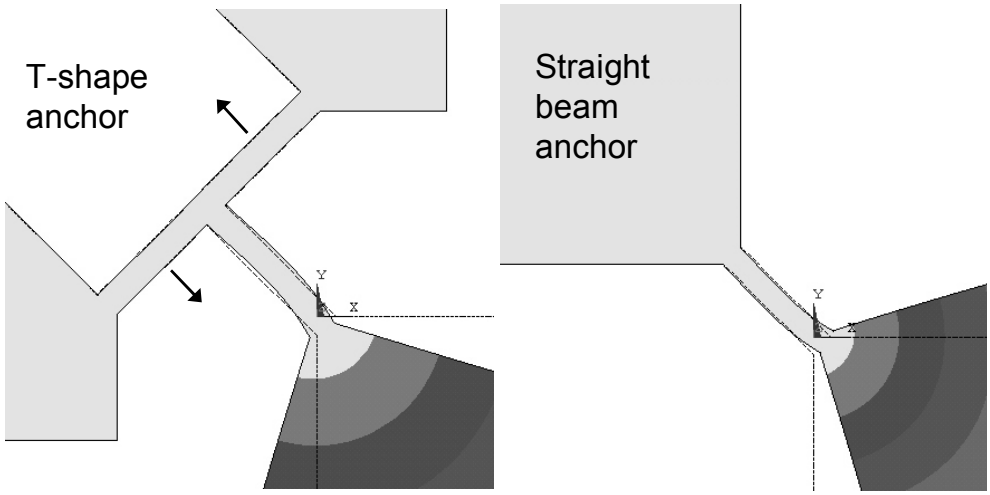

Figure 3.26: Detailed movement of *T*-shaped anchor and straight-beam anchor at resonance from the simulation of Lamé-mode square resonator.

Other factors that could contribute to the difference in *Q* values are the sizing of the anchor beams, such as width and length of the beams. A detailed study of all these factors with regard to anchor losses and how different anchor geometry impacts the quality factor would be invaluable information for resonator design.

3.7.2 7MHz length-extensional resonators

Improvement in device performance through enhanced modification of anchor geometry applies not only for Lamé-mode square resonators but also for other types of bulk-mode resonators such as length-extensional rectangular resonators. This sub-section presents the performance of differentially-driven 7MHz length-extensional bulk-mode resonators with *T*-shaped and straight-beam anchors. Resonators with *T*-shaped anchors perform better with lower motional resistance and six times higher quality factor than the resonators with straight-beam anchors.

Normally, length-extensional resonator is driven and sensed in one-port or two-port electrical configuration. A pair of two length-extensional resonators, as shown earlier in Figure 2.5, can be used to create anti-phase mode shapes such that differential drive is possible, along with the benefit of suppressing the parasitic feedthrough capacitances. Micrograph and mode shape simulation in Abaqus of length-extensional resonator pair with straight-beam anchors are shown in Figure 3.27, and that of resonator pair with *T*-shaped anchors are shown in Figure 3.28. Modal simulation shows only slight difference in mode shapes between straight-beam and *T* anchor designs. With *T* anchor, lateral movement near anchor region along the width is more pronounced. The displacement is zero right at the center of the rectangular resonators. The *T* anchor is basically an extension of the straight-beam anchor of 60μm × 10μm, which is attached to another beam termed *T-beam* with dimensions of 100μm × 10μm.

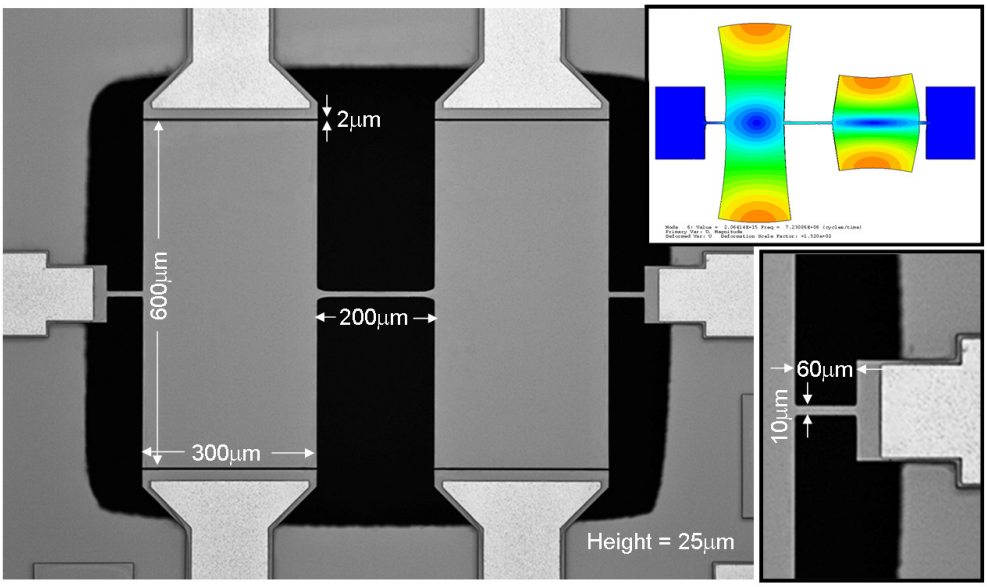

Figure 3.27: Micrograph and mode shape of length-extensional resonator pair with straight-beam anchors.

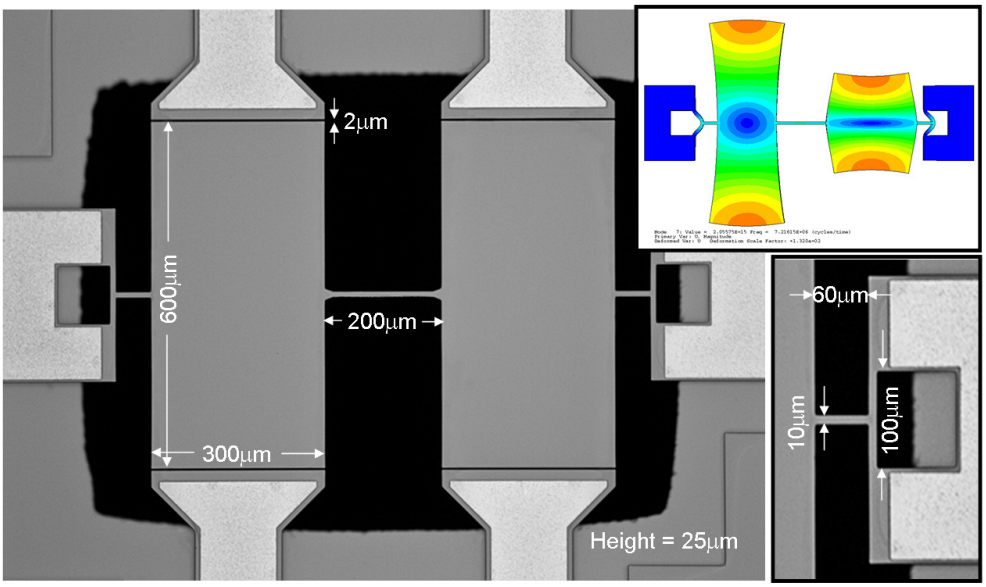

Figure 3.28: Micrograph and mode shape of length-extensional resonator pair with *T*-shaped anchors.

Measurement of length-extensional resonators from Figure 3.27 and Figure 3.28 were done at the same drive conditions, AC drive of 0.42Vpp with V_P bias of 100V. The S_{21} transmission plots for both devices are shown in Figure 3.29.

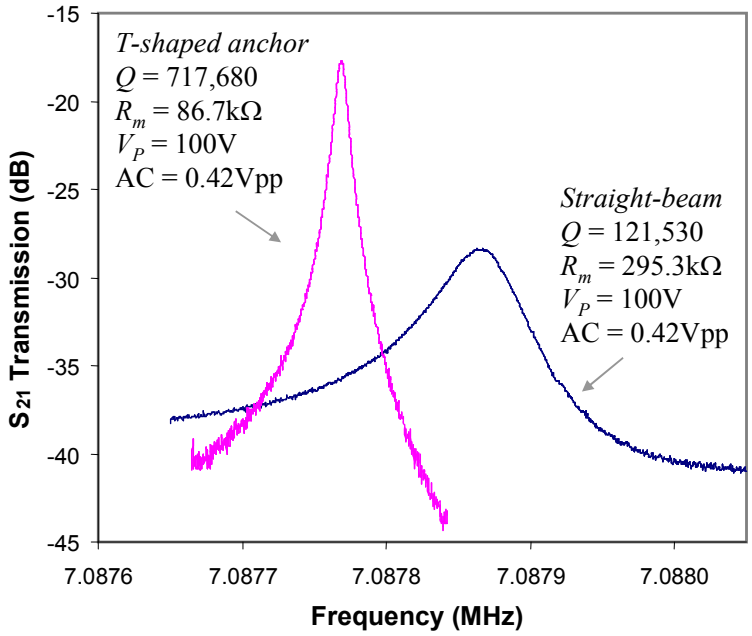

Figure 3.29: S_{21} response of resonators with *T*-shaped anchor (*T-beam* = 100μm) and straight-beam anchor. *T*-anchored resonators perform better with six times higher in *Q* and 70% lower motional resistance.

The resonant frequencies of resonators are close to each other at 7.09MHz. Length-extensional resonator with *T* anchors has about six times higher quality factor and 70% lower motional resistance compared to that with straight-beam anchors. Since the mode shape from finite element displacement contour simulation as shown in Figure 3.30 indicates that anchoring point at the middle of the resonator's length moves in and out laterally. Therefore, flexibility at anchor point would reduce energy losses with sustained vibrations at resonance, which is in agreement with our experimental data that resonators perform better with flexible *T* anchors. However, the *T-beam* that makes up the *T*-shape needs to be carefully designed. Another device with longer T-beam of 200μm is measured to have almost undetectable S_{21} response because the output signal is very weak, not enough to measure the *Q* with 3dB-bandwidth method. Simulation result shown in Figure 3.31 reveals that strong flexural vibrations of T-beam suppress the extensional bulk-mode of our interest.

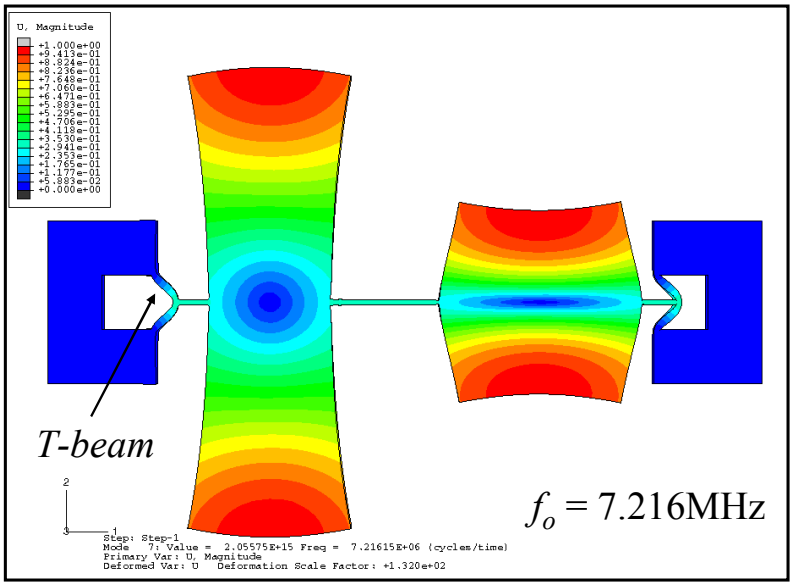

T anchor with *T-beam* = 100μm

Figure 3.30: Mode shape of *T*-anchored resonator with 100μm *T-beam*. In this case the length-extensional mode appears normal.

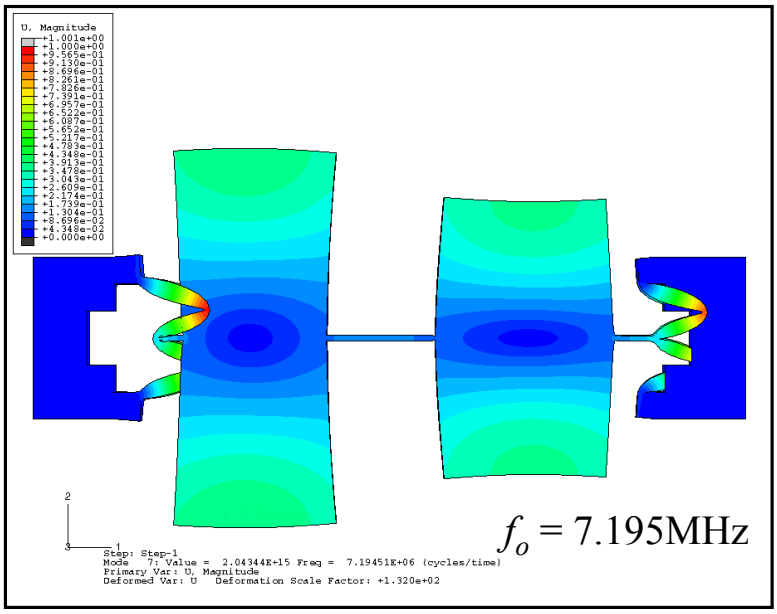

T anchor with *T-beam* = 200µm

Figure 3.31: Desired length-extensional mode is interfered by vibrations of longer *T* anchor with 200µm *T-beam*.

Abaqus simulations of other T-beam lengths show that the device might not work well for a narrow range of values for T-beam length from 195µm to 210µm. The worst case for T-beam length is about 204µm and the length-extensional mode is barely visible in simulation result. A closer examination of the *T* anchor region from simulation result is shown in Figure 3.32 where the resonator mass hardly moved with near zero displacement. It's interesting to note that the T-beam in Figure 3.32 is not one of the normal modes of resonance for a clamped-clamped beam. At this mode, the two halves of the *T-beam* bend in-sync laterally in the same plane as the resonator. The middle point of the T-beam is forced to have almost zero movement and in turn this obstructs the length-extensional mode of the resonator.

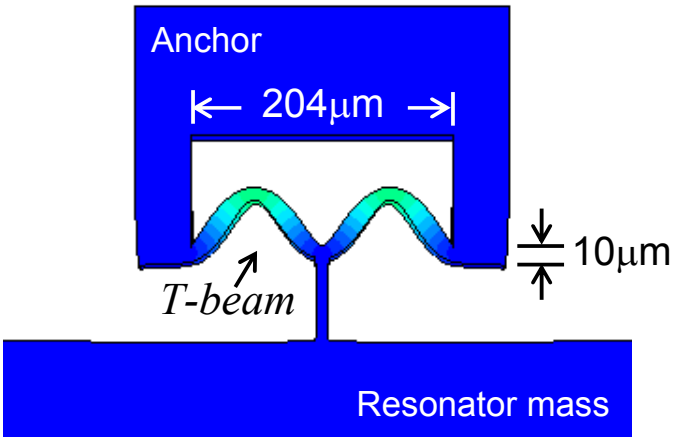

Figure 3.32: A cropped section of an anchor region from Abaqus modal simulation for length-extensional resonator pair with *T-beam* = 204μm.

In summary, for length-extensional mode resonator, if the width of the resonator is not considerably smaller than its length, then there are in-plane lateral displacements perpendicular to the longitudinal vibrations at the middle region of the resonator plate. These movements effectively impose axial stress on the straight-beam tethers. Therefore, by replacing the straight tether beam with *T*-shaped anchor geometry relieves the stress with more freedom for lateral movement. However, it was observed that at certain dimensions of the *T* structure, a particular flexural resonance mode of *T*-shaped anchor significantly hinders the length-extensional mode of the resonator.

3.8 Summary

Quality factor performance of micromechanical resonators has been explored in this chapter. Quality factor of bulk-mode resonators (Lamé-mode square, wine-glass disk and length-extensional resonators) are measured to be on the order of ~10^6 and that of flexural Clamped-Clamped beam and Free-Free beam resonators are only in thousand range. As a result, the f_o–Q product of the bulk-mode resonators is about 10^{12} –10^{13}, which is three orders of magnitude higher than that achievable with the beam resonators. High mechanical stiffness k_m ~10^7 of bulk-mode resonators are roughly four orders of magnitude above the k_m values of flexural beam resonators.

The quality factor is also dependent on the structural geometry of Lamé-mode square resonators based on the number of anchors, structural layer thickness, and the presence of release etch holes. There are several Q-limiting energy loss mechanisms that govern the overall Q of resonator and anchor losses are one of the dominant factors affecting the Q of bulk-mode resonators. A study of bulk-mode resonators having various straight-beam anchor and T-shaped anchor designs suggest that optimized anchor design with minimal energy losses would result in resonators with superior quality factor.

However, quality factor is not the only key performance parameter to be optimized for resonator. For example, anchor geometry could be designed such that power handling does not go down significantly. The Q values that have been reported in this chapter are all measured at high vacuum. The Q will inevitably drop as the surrounding pressure is increased mainly due to *squeeze-film damping* or *air damping*, and the following chapter will discuss this matter in more detail.

Chapter 4

Pressure Stability of Resonators

How stable the frequency response of a resonator under various pressure levels has practical implication. Pressure changes can have considerably impact on the short-term and long-term frequency stabilities of the resonator. The quality factor of the resonator will drop as the surrounding pressure is increased beyond a threshold level due to squeeze-film damping or air damping. Therefore, it is desirable to understand how the resonant frequency and the quality factor of resonators change with varying pressure. This chapter presents the measured performance of flexural beam resonators and bulk-mode resonators under various pressure levels.

4.1 Pressure stability

For capacitive micromechanical resonators that have air gaps between the electrodes and the resonator, air damping will interfere with the vibrations of resonator at high pressure levels. Therefore, the resonator needs to operate in vacuum and hermetically sealed for eventual commercialization of the device. A good performance of the resonator under high pressures will lead to lower cost in vacuum packaging, because high level vacuum

is generally more expensive to achieve for device packaging. One of the attractive packaging methods is the wafer-level encapsulation approach [84-86] that not only reduces the cost, but also protects the device during subsequent process steps such as dicing and cleaning.

The two main parameters that are affected by pressure changes are the quality factor and the resonant frequency of the resonator. The resonant frequency will slightly *increase* or *decrease* with gas pressure depending on whether the *viscous damping forces* (proportional to the velocity) or the *elastic damping forces* (proportional to displacement and acceleration) are more dominant [87]. However, the shift in resonant frequency is usually minor compared to the more significant changes in Q with pressure.

If the resonator is operated in high enough pressure, the term Q_{air} in equation (3.5) becomes dominant such that after some threshold pressure level the Q gradually drops off with a certain trend. For example, the quality factor is reported to be inversely proportional to the pressure for tuning-fork resonators [70]. The squeezed-film damping effect is much more pronounced for lower resonant frequencies. However, the effect is likely insignificant at higher frequencies at UHF range for certain bulk-mode resonator design with high mechanical stiffness, as reported in [29] for the disk resonator that could achieve fairly high Q in air without vacuum packaging.

4.2 Squeeze-film damping or air damping

The squeeze-film damping or air damping phenomenon is a complex process, and in-depth analysis and accurate modeling are beyond the scope of this thesis. A brief summary on air damping will be presented in this section. A comprehensive overview paper on squeeze-film air damping is reported by M. Bao, *et al*. in [88], which discusses the basic effects of squeeze film damping on the dynamic performances of micro-structures including the air damping of parallel plates, slotted plates, and torsion mirrors.

For a pair of parallel plates, the resistive force to the moving plate interacting with the stationary plate is caused by the damping pressure between the two plates [88]. The damping pressure consists of two main components: the component that causes the viscous flow of air (viscous damping force) and the other that causes the compression of air film (elastic damping force). If the plate oscillates with a low frequency, the gas film is not compressed appreciably and the viscous damping force is dominant. The viscous force is directly proportional to the speed of the plate. On the other hand, if the plate oscillates with a very high frequency, the gas film is compressed and trapped within the gap, in which case the elastic force is dominant. The elastic force is directly proportional to the displacement of the plate.

According to Blom, *et al*. [89], the pressure dependence of quality factor can be divided into three different regions: 1) the intrinsic region, 2) the molecular region, and 3) the viscous region. Instead of calculating all the damping parameters in every region, Blom, *et al*. proposes to concentrate on the damping parameters that are dominant in one particular region. In the intrinsic region, the air pressure is very low that air damping may be negligible and the Q of resonator can reach a maximum value.

In the molecular region, the interaction between gas molecules can be ignored and the damping force is caused by the collisions of air molecules with the moving surface of the vibrating resonator. The quality factor due to air damping for the resonator with parallel-plate electrodes in this region in low vacuum (high pressure) [70, 88] can be predicted as

$$Q = \frac{h\rho(2\pi f)}{4}\sqrt{\frac{\pi}{2}}\sqrt{\frac{RT}{M_m}}\cdot\frac{1}{P}, \tag{4.1}$$

where h = thickness of the resonator,

ρ = mass density of the resonator plate,

f = resonant frequency of the plate,

R = universal molar mass constant = 8.31 kg m^2/(s^2 K),

T = absolute temperature in Kelvins, and

M_m = molar mass of the gas.

In the viscous region, the pressure levels are high up to the atmospheric pressure or even higher levels. The air behaves as a viscous fluid in this region and damping force is calculated using fluid mechanics [89].

In summary, below a certain low pressure level in high-vacuum the damping is intrinsic to the resonator and the Q is independent of the pressure. As the pressure rises to intermediate levels, the damping is determined by the independent collisions of the gas molecules and vibrating resonator. At very high pressures the damping mechanism is governed mostly by the fluid mechanics.

4.3 Performance of resonators under varying pressure

Performance of flexural beam resonators and bulk-mode resonators under various pressure levels, from high vacuum towards the atmospheric pressure, will be presented in this section. In high vacuum, the intrinsic damping of the resonator is dominant and the Q of resonator is expected to be independent of pressure. As the pressure is increased, the collisions of air molecules and the resonator become significant such that degradation in Q of the resonator in general is inversely proportional to the pressure. Under very high pressures up to the atmospheric pressure level, the resonator would be seriously damped and respond with the lowest quality factor.

4.3.1 Flexural-mode resonators

Performance of Clamped-Clamped beam resonator and Free-Free beam (fundamental-mode and second-mode) resonators under different pressures are presented in this section. The resonant frequency generally increased for all the beam resonators as the pressure is increased from high vacuum to ~1000Pa, and the frequency shift is about 30ppm – 140ppm over this pressure range. Since the resonators are vibrating at low frequency, the gas film is not compressed appreciably and the viscous damping force is dominant, which leads to an increase in resonant frequency [87]. The change in quality factor with increasing pressure is much more significant compared to the resonant frequency shift. Figure 4.1 shows the plot of measured quality factor of all three beam resonators vs. pressure in log-log scale.

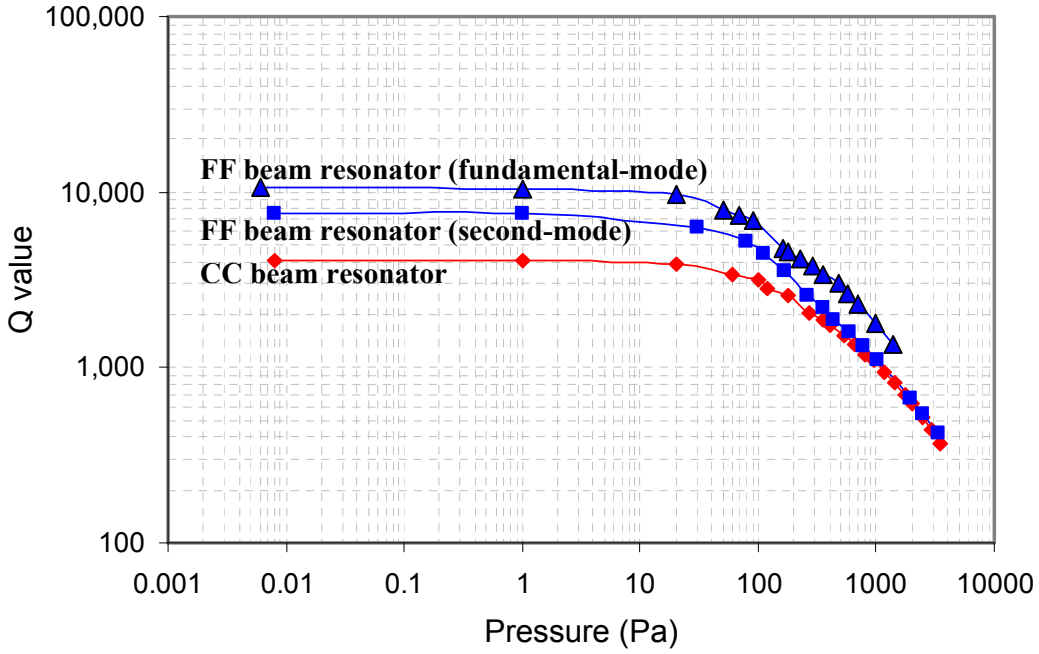

Figure 4.1: Quality factor vs. pressure plots for Clamped-Clamped beam resonator and Free-Free beam (fundamental-mode and second-mode) resonators.

The *Q* is measured with 3-dB method until it is no longer accurate due to anti-resonance peak at high pressures. The measured quality factor is roughly constant at maximum value at pressures below 10Pa, and the *Q* gradually decreases at higher pressures. The 615kHz Free-Free beam resonator (fundamental-mode) has the highest maximum *Q* of 10,520 followed by the 529kHz second-mode Free-Free beam resonator with *Q* of 7,510. The maximum *Q* of 917kHz Clamped-Clamped beam resonator is only 4,070. In the molecular region, all the curves eventually follow a similar trend of *Q* inversely proportional to the pressure. Given that all the tested beam resonators have parallel-plate drive and sense electrodes, their *Q* performance affected by air damping is quite comparable.

4.3.2 Bulk-mode resonators

Performance of bulk-mode resonators under various pressures are presented in this section. The resonant frequency increases with pressure for all the bulk-mode resonators tested, indicating that viscous damping force is dominant for parallel-plate electrodes with 2μm electrode-to-resonator gap. The amount of frequency shift for bulk-mode resonators is less than that of the flexural beam resonators described in previous section, about 18ppm – 30ppm over the pressure range from high vacuum to ~1000Pa, compared to 30ppm – 140ppm of the beam resonators.

The Q of 6.358MHz Lamé-mode square resonator was measured at pressure levels from high vacuum up to one atmospheric pressure (~10^5 Pa) and the results are shown in Figure 4.2, where Q vs. pressure is plotted in log-log scales.

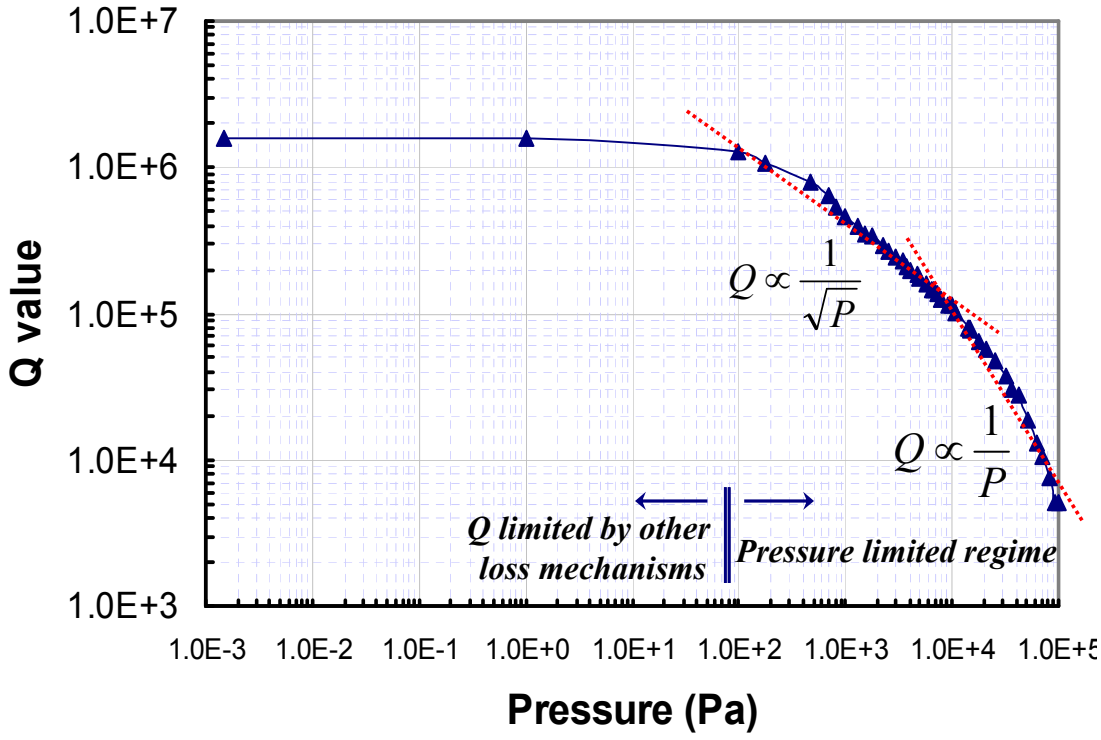

Figure 4.2: A plot of measured Q vs. Pressure for 6.358MHz Lamé mode square resonator.

The polarization voltage V_P of 60V was fixed at all pressure levels. The Q value remained almost constant up to 100Pa, maintaining Q values exceeding one million. However beyond 100Pa, the measured Q drops inversely with the square root of pressure initially, and then drops inversely with pressure, reaching a Q of about 5100 at a pressure of ~10^5 Pa. The relatively low Q in this pressure-limited regime at pressures above 100 Pa is mainly due to air damping [70, 88, 89], which means that the effect of squeeze-film or air damping is the dominant loss mechanism.

As the pressure gets higher, low AC drive signal is not strong enough to characterize the S_{21} resonance peak, and higher AC levels become necessary. Figure 4.3 illustrates S_{21} resonance peaks of the same Lamé-mode square resonator, design 3J (60μm × 20μm) from Section 3.6. At pressure of 100 Pa, the measured Q is 977,600 and the Q drops to 102,500 at 1.09×10^4 Pa, while the shift in resonant frequency is minimal.

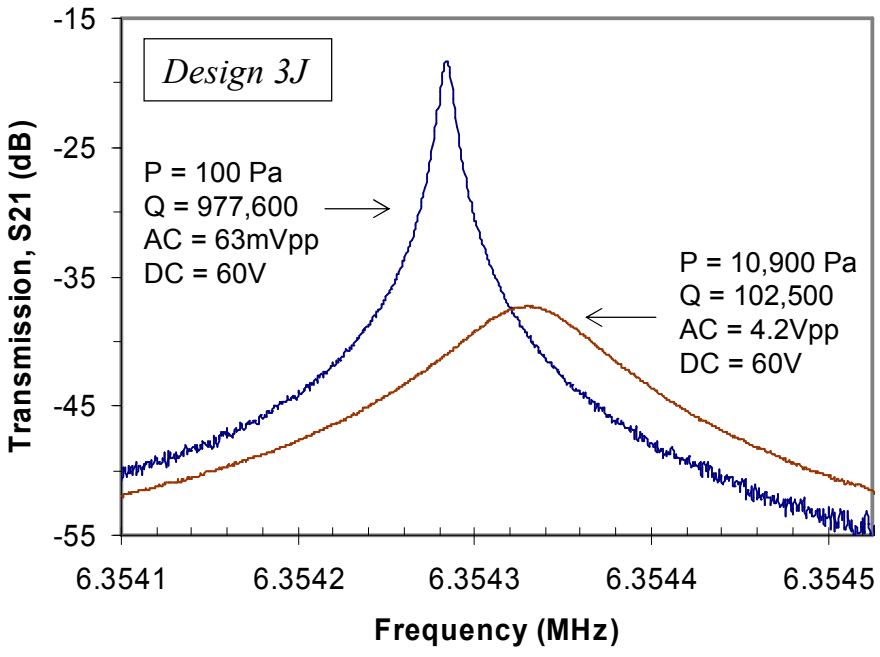

Figure 4.3: S_{21} plots of design 3J with 60μm by 20μm anchor. Measured Q value drops from 977,600 at 100Pa to 102,500 at 1.09×10^4 Pa.

Quality factor measurements with varying pressure are done for other bulk-mode wine glass disk resonator (shown earlier in Figure 3.10(b)) and length-extensional resonator (shown in Figure 3.12). Figure 4.4 presents the log-log plot of Q vs. pressure for all three types of bulk-mode resonators.

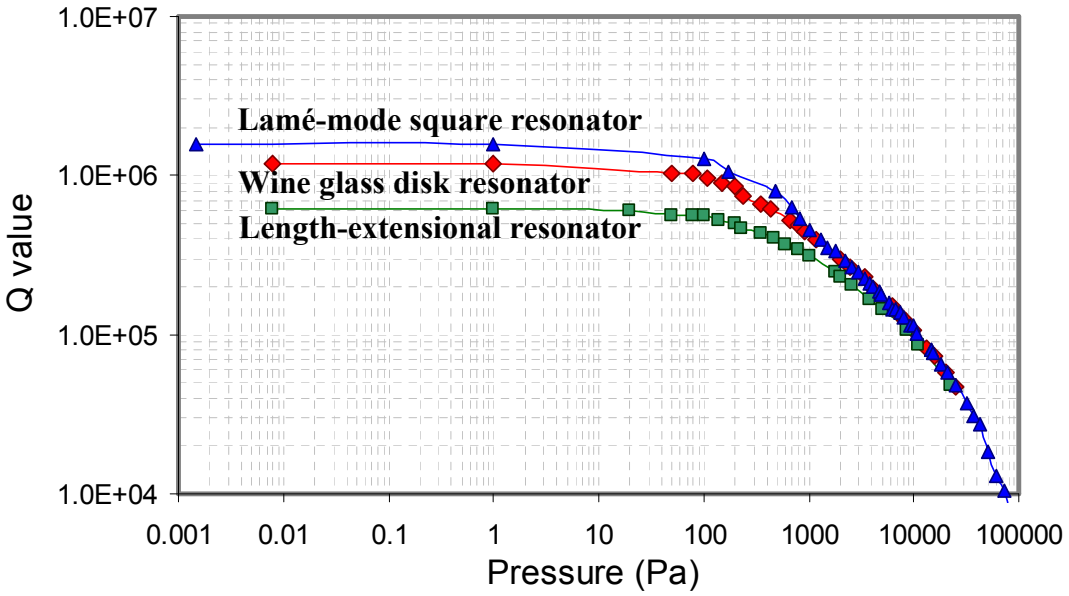

Figure 4.4: Comparison of Q vs. pressure log-log scale plots for Lamé-mode square resonator, wine glass disk resonator and length-extensional resonators.

For all three bulk-mode designs, low pressure high-Q values are maintained with very little drop in Q as pressure is increased up to 100's of Pa. Let P* to designate the pressure at which the Q value is about 70.7% of the maximum Q. The quality factor decreases much faster at pressures above P* where air damping is the major loss mechanism. The P* values for Lamé-mode square, wine glass disk and length-extensional resonators are 150 Pa, 220 Pa and 310 Pa, respectively. The P* values of fundamental-mode Free-Free beam, second-mode Free-Free beam and Clamped-Clamped beam resonators from Figure 4.1 on the other hand are about 55 Pa, 65 Pa and 90 Pa, respectively.

The optimal operating pressure should be lower than P* so as to achieve quality factor closer to the maximum Q value. If we consider the Q versus pressure plot of tuning-fork type beam resonators reported in [70], the drop in Q from maximum value happens at pressures of 0.1Pa to 1Pa. For the bulk-mode resonators reported here, significant Q reduction only happens at much higher pressures, at hundreds of Pascal.

The plot in Figure 4.5 compares the Q performance under different pressures for bulk-mode resonators and flexural-mode beam resonators of this work, which clearly shows that bulk-mode resonators outperform the beam resonators in terms of maximum achievable quality factor and higher threshold pressure level when the Q begins to drop. This observation is mainly due to the high stiffness or spring constant (k) of the bulk-mode resonators in comparison to flexural-type resonators.

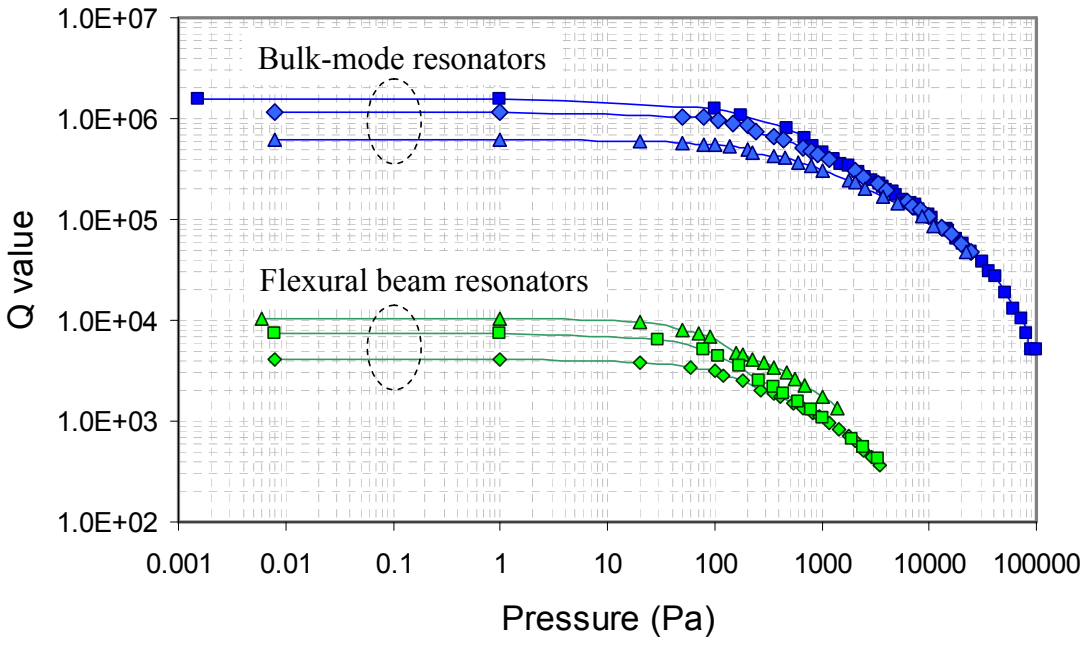

Figure 4.5: Quality factor vs. pressure plot comparison of bulk-mode resonators and flexural-mode beam resonators.

The equation (2.15) can be rearranged to give the relationship between Q and k as:

$$Q = \frac{k}{\delta \cdot (2\pi f_o)}. \tag{4.2}$$

Even though the magnitude of air damping at certain pressure (with damping coefficient δ) experienced by both types of resonators is the same, bulk-mode resonators with four orders of magnitude higher mechanical stiffness (as listed in Table 3.3) will have corresponding higher quality factor. Figure 4.5 suggest that bulk-mode resonators could provide Q > 100,000 at pressures as high as ~10^4 Pa and that they would perform well in atmospheric pressure, and eliminate the need for high vacuum level packaging.

4.4 Summary

This section presented the stability of flexural and bulk-mode resonators under various pressures. The resonant frequency can shift with pressure changes depending on the type of damping force, but changes in Q with pressure are much more significant compared to the resonant frequency shift. After certain threshold pressure level the Q of resonator will begin to drop due to air damping, and eventually Q becomes inversely proportional to the pressure. Performance comparison of flexural beam and bulk-mode resonators show that bulk-mode resonators with much higher mechanical stiffness outperform the beam resonators, and bulk resonators are able to maintain the maximum Q under higher pressure levels. The test results presented in this section were done with resonators operating in linear region of vibration. The following chapter discusses how their performance is affected when they are operating in nonlinear region.

Chapter 5

Power Handling and Nonlinearity

Power handling capability is one of the important parameters for resonators. In this chapter, power handling of flexural resonators and bulk-mode resonators will be discussed along with the mechanical nonlinearity and electrical nonlinearity of micromechanical resonators. When a resonator is driven to operate in nonlinear region, resonant frequency begins to fluctuate and becomes dependent on the vibration amplitude. Nonlinearities also alter the structural damping and hence affect the quality factor. Nonlinearities also put a limitation on the power handling capabilities of the resonator. Power handling of a resonator is just as important as the quality factor when considering its overall performance. Measured results of Free-Free beam resonator and Lamé-mode square resonators show that bulk-mode square resonators can handle much more power, orders of magnitude higher compared to the power that Free-Free beam resonators can withstand, before the resonators go into nonlinear region.

5.1 Power handling of resonator

As the size of micromechanical resonators becomes smaller to push the operation frequency into UHF range, it is inevitable that the power handling capability of the

resonator will become reduced. For resonators targeted towards VHF and UHF frequency ranges, bulk-mode and contour-mode micromechanical resonators have shown to provide higher Q values along with better power handling capabilities, compared to the flexural-type beam resonators [19, 90, 91]. Trade-offs between Q and power handling is considered to be very important in setting the close-to-carrier and far-from-carrier phase noise for an oscillator [19]. The importance of power handling capabilities for an oscillator can be demonstrated by examining Leeson's equation of phase-noise density to carrier power ratio. Leeson's equation as reported in [92, 93] that models the phase noise-to-carrier ratio for an ideal linear oscillator is

$$L(\Delta f) = 10 \cdot \log\left\{\frac{2kT}{P_{out}}\left(1+\left(\frac{f_o}{2Q\Delta f}\right)^2\right)\right\}, \tag{5.1}$$

where P_{out} = the signal power of oscillator,

k = Boltzmann constant (1.38×10^{-23} JK^{-1}),

T = absolute temperature in Kelvins,

Q = quality factor,

f_o = carrier frequency, and

Δf = frequency offset from the carrier.

According to Leeson's equation above, the overall phase noise can be reduced by an increase in oscillation output signal power (P_{out}). Expression for P_{out} [19] is given by

$$P_{out} = \frac{1}{2} i_o{}^2 R_{tot}, \tag{5.2}$$

where i_o is motional output current and R_{tot} is total resistance that consumes power in oscillation loop. The output power can also be expressed in terms of the stored signal energy (E_{stored}) as below:

$$P_{out} = \frac{2\pi f_o E_{stored}}{Q}. \tag{5.3}$$

When equation (5.3) is substituted into equation (5.1), Leeson's equation for phase noise can be derived as

$$L(\Delta f) = 10 \cdot \log\left\{ \frac{kTQ}{\pi f_o E_{stored}} + \frac{kTf_o}{4\pi E_{stored} Q \Delta f^2} \right\}. \tag{5.4}$$

The first term in equation (5.4) determines the noise floor and the second term represents the close-to-carrier phase noise. Having high Q and large E_{stored} both can lower the close-to-carrier noise. However, the noise floor will deteriorate with increasing Q, and therefore large E_{stored} of similar order of magnitude is needed to offset very high quality factor. Hence, it is important to optimize both the Q and E_{stored} together.

The vibration energy stored (E_{stored}) in the micromechanical resonator [91, 94] is

$$E_{stored} = \frac{1}{2} k_l X^2, \tag{5.5}$$

where k_l is the linear spring constant and X is the vibration amplitude of resonator. Moreover, output current i_o is directly proportional to vibration amplitude X of the resonator. Therefore, resonator with good power handling implies that it can produce high output current due to large amplitude of vibration, as well as it is able to store large vibration energy. Bulk-mode resonators are shown to be able to store orders of magnitude higher vibration energy than flexural beam resonators [91] mainly due to high mechanical stiffness of bulk-mode resonators. Mechanical spring constant of bulk-mode resonators, as presented earlier in Table 3.3, is four orders of magnitude higher than the stiffness values of flexural beam resonators.

For applications where nonlinear vibrations are undesirable, the maximum stored energy ($E_{stored}^{\max}$) of micromechanical resonator is limited by critical vibration amplitude (X_C) at the onset of nonlinear hysteresis. In other words, it is the maximum power that resonator can handle before it goes into nonlinear regime. Based on nonlinearity comparison, it is shown in [91] that Lamé-mode square resonator has three orders of magnitude larger maximum energy storage capacity than the Free-Free beam resonator. Therefore, bulk-mode resonators having both ultra-high Q's in millions and high energy storage capability should perform well for oscillator applications with superior phase noise performance.

5.2 Nonlinearity in micromechanical resonator

The displacement of a typical micromechanical resonator can be approximated by that of a mass-spring-damper system as described in Section 2.3.1. Equation (2.11) is valid when the displacement or amplitude of vibration of the resonator is relatively small with linear motion. Once the excitation force $F(t)$ becomes large and resulting in larger vibration amplitudes, additional terms are necessary in equation (2.11) to factor in the mechanical and electrical nonlinearities. The nonlinear motion can be estimated by replacing $\{kx\}$ term of equation (2.11) with $\{k_1x + k_2x^2 + k_3x^3\}$, where k_1 is linear spring constant, anharmonic spring constants k_2 and k_3 account for *quadratic* nonlinearities and *cubic* nonlinearities, respectively. Then, the lumped Duffing's equation for nonlinear vibration [95] for a micromechanical resonator can be written as

$$m\frac{\partial^2 x}{\partial t^2}+\delta\frac{\partial x}{\partial t}+k_1x+k_2x^2+k_3x^3=F(t), \tag{5.6}$$

According to Landau, the shift in resonant frequency due to nonlinearities can be solved through successive approximation to give a new amplitude-dependent frequency (f_o') expressed as

$$f_o'=f_o+\kappa\cdot X_{o,f_o'}^2, \tag{5.7}$$

where $X_{o,f_o'}$ is the vibration amplitude of resonator at frequency f_o' and the term κ is a function of spring constants given by

$$\kappa=\frac{3k_3}{8k_1}f_o-\frac{5k_2^2}{12k_1^2}f_o. \tag{5.8}$$

Depending on the sign of the nonlinear parameter κ, the nonlinear resonant frequency peak could bend towards the higher frequency (spring hardening for positive κ), or towards lower frequency (spring softening for negative κ) [95], as shown in Figure 5.1.

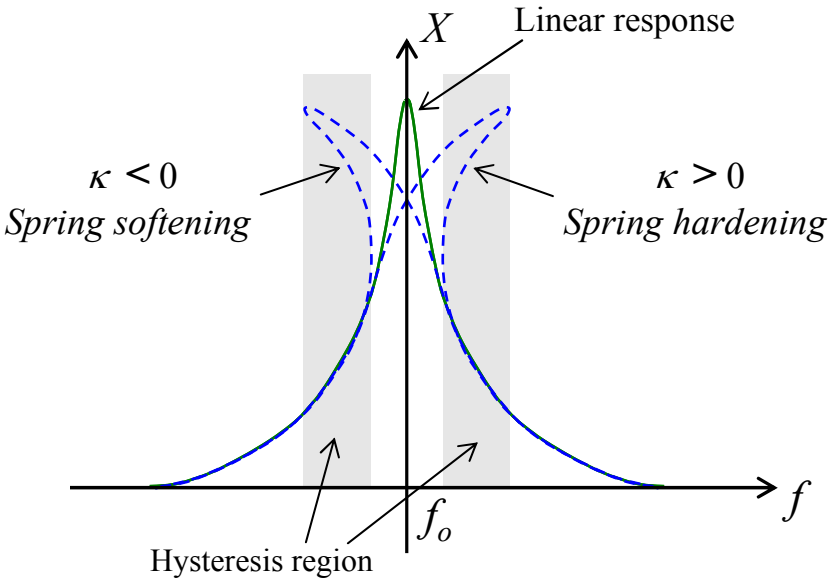

Figure 5.1: The effect of nonlinearity on the transmission curve of resonator. Resonance peak tilts toward higher frequency for $\kappa > 0$, and toward lower frequency for $\kappa < 0$. The shaded hysteresis region has three possible solutions for resonant frequency.

Usually the effect of cubic nonlinearity is dominant over that of the quadratic nonlinearity. The equation (5.6) represents the overall dynamics of resonator's nonlinearity, which can be further broken down into mechanical nonlinearity and electrical nonlinearity.

5.2.1 Mechanical nonlinearity

When considering the mechanical nonlinearities, if the resonator structure is designed to be symmetric for both positive and negative displacements, the quadratic nonlinearity term can be dropped and the nonlinear response can be approximated by using the term $\{k_{m1}\,x + k_{m3}\,x^3\}$ [96, 97], where k_{m1} and k_{m3} represent linear and cubic mechanical spring constants, respectively. The even-powered quadratic nonlinear term $\{k_{m2}\,x^2\}$ should be included when drift motion is involved, such that the oscillatory motion is not centered at some middle axis [98].

One method of approximating the mechanical spring constants is to use finite element tool such as ANSYS. A distributive excitation force can be applied to the side of the beam, while large nonlinear displacement calculations are included in the simulation for beam deflections. After which the values of k_{m1}, k_{m2} and k_{m3} can be extracted from force versus displacement curve. However, this method usually does not yield accurate results for a complex resonator structure and hence, alternate methods are needed to extract the nonlinear mechanical spring constants. One of such methods is presented in [99] as semi-analytic technique to model and characterize nonlinearities of any type of resonators, and is very effective in extracting both the linear and nonlinear

parameters of resonator from preliminary measurement results. Mechanical nonlinearity mechanism due on quadratic nonlinearity has the spring softening effect if the value of k_{m2} is significant, regardless of the sign of k_{m2}, and if the cubic spring constant k_{m3} is smaller than a certain critical value [98]. The actual estimation of this critical k_{m3} value could be difficult depending on the complexity of the resonator structure.

The resonant frequency shift due to nonlinearity is dependent on the square of the vibration amplitude according to equation (5.7). Larger vibrations lead to a discontinuity or jump (bifurcation) in frequency response curve and eventually result in frequency *hysteresis*. The hysteresis region as shown in Figure 5.1 is where the frequency response curve is triple-valued, which means there are three possible solutions from theoretical calculation. However, only two stable points can be experimentally observed within the hysteresis region of transmission curve in open-loop measurements. The hysteresis loop in transmission response can be experimentally observed by sweeping the frequency upward and then downward again.

The onset of bifurcation, also termed as 'hysteretic point' in [100], is commonly used as the boundary of linear and nonlinear operation for resonator. The critical excitation force F_C that would initiate the bifurcation can be calculated [95, 96] below:

$$F_C = \sqrt{\frac{64\sqrt{3}\pi^4 m^2 f_o^5}{9|\kappa|Q^3}}, \tag{5.9}$$

where m is the effective mass of the resonator, f_o the natural frequency, and κ is the constant term of equation (5.8). The maximum amplitude of vibration (X_C) at hysteretic point can be derived [95] as

$$X_C = \sqrt{\frac{4 f_o}{3\sqrt{3}|\kappa|Q}}. \tag{5.10}$$

For an electrostatically-actuated micromechanical resonator, the interaction between the electrostatic driving force and the mechanical restoring force determines the overall dynamics of the resonator. When the electrostatic excitation force exceeds the critical force F_C, bifurcation will begin to happen with hysteresis loop in frequency response. The following section discusses the nonlinearity contributed by the electrostatic driving force in detail.

5.2.2 Electrical nonlinearity

For a two-port capacitively driven-and-sensed resonator with parallel-plate electrodes, the forcing term *F(t)* on the right of equation (5.6) becomes the overall electrostatic force F_e, which depends on DC bias V_P and AC drive v_{ac} as below:

$$F_e = \left[\frac{1}{2}{V_P}^2 \frac{\varepsilon_o A_e}{(d-x)^2}\right] - \left[\frac{1}{2}(V_P - v_{ac})^2 \frac{\varepsilon_o A_e}{(d+x)^2}\right], \tag{5.11}$$

where ε_o is the permittivity of free space, A_e is the area of the electrode plate, d is the original electrode gap, and x is displacement of resonator. As the force F_e is imposed on the resonator it moves by some displacement x. Since $V_P >> v_{ac}$, v_{ac} can be neglected in equation (5.11) for non-zero x and the force F_e becomes

$$F_e = \frac{1}{2}\varepsilon_o A_e {V_P}^2 \left[\frac{1}{(d-x)^2} - \frac{1}{(d+x)^2}\right]. \tag{5.12}$$

For $\left(\frac{x}{d}\right) << 1$, substituting the Taylor series expansion in equation (5.12), the overall electrostatic spring force can be simplified as below:

$$F_e = \frac{\varepsilon_o A_e {V_P}^2}{2d^2}\left[4\left(\frac{x}{d}\right)+8\left(\frac{x}{d}\right)^3+\ldots\right]. \tag{5.13}$$

From above equation (5.13), the linear and cubic electrical spring constants can be extracted as

$$k_{e1} = -\frac{2\varepsilon_o A_e {V_P}^2}{d^3} \quad \text{and} \quad k_{e3} = -\frac{4\varepsilon_o A_e {V_P}^2}{d^5}, \tag{5.14}$$

which are largely dependent on the square of DC voltage V_P and inversely proportional to the powers of electrode gap. The quadratic electrical spring constant k_{e2} is zero in this case. The negative signs of k_{e1} and k_{e3} indicate that the electrostatic force is in the direction opposite to the mechanical restoring force.

In order to take the combined effects of both mechanical and electrical nonlinearities, the mechanical spring constants k_m's and electrical spring constants k_e's should be summed up and the overall system dynamics of equation (5.6) becomes

$$m\frac{\partial^2 x}{\partial t^2}+\delta\frac{\partial x}{\partial t}+\left(k_{m1}+k_{e1}\right)x+\left(k_{m3}+k_{e3}\right)x^3 = \frac{\varepsilon_o A_e}{d^2}\cdot V_P \cdot v_{ac}, \tag{5.15}$$

where the interactions of mechanical and electrical spring constants determine the overall nonlinear behavior. The nonlinearity from electrical spring constants always results in spring softening. If the cubic nonlinearity is dominant, the difference between k_{m3} and k_{e3} will dictate the Duffing behavior. The k_m values come from intrinsic mechanical properties of the resonator, whereas the k_e values can be tuned by adjusting DC bias or the electrode gap. Hence, there is the possibility of nonlinearity cancellation if the k_e values are in the same order of magnitude as k_m values. The quadratic nonlinear spring constant terms are ignored with the assumption of symmetric resonator structure.

5.3 Nonlinearity of Free-Free beam resonator

This section presents measured nonlinear behavior of a Free-Free beam at fundamental mode as shown in Figure 2.2 of Section 2.2.2. The symmetric shape of transmission curve at resonance is observed for low AC drives (v_{ac}) as seen in Figure 5.2. When v_{ac} is increased keeping V_P constant, the resonance peak becomes distorted by tilting to the right (spring hardening). This is due to nonlinear "Duffing" behavior as outlined in previous section, and the spring hardening effect is a typical result observed for all constant V_P-biased v_{ac} variations for this device.

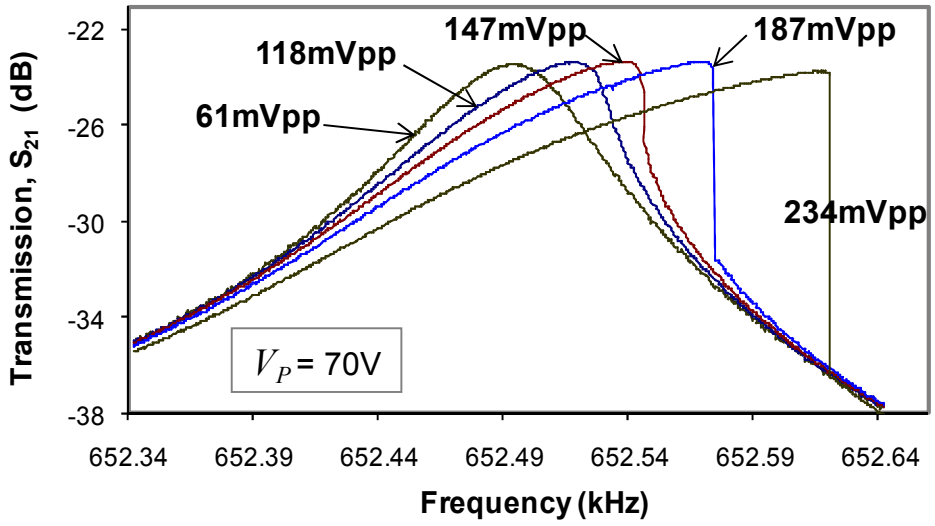

Figure 5.2: Measured nonlinear response of Free-Free beam (fundamental mode) for increasing v_{ac}, with V_P fixed at 70V.

From measured resonant frequency vs. V_P plot at low AC drive shown in Figure 5.3, linear mechanical spring constant k_{m1} can be extracted using equation (3.10). The value of k_{m1} can also be found from force vs. displacement obtained through ANSYS simulations. Predicted resonant frequencies using k_{m1} from ANSYS is also plotted in Figure 5.3 and they differ from measured data as shown.

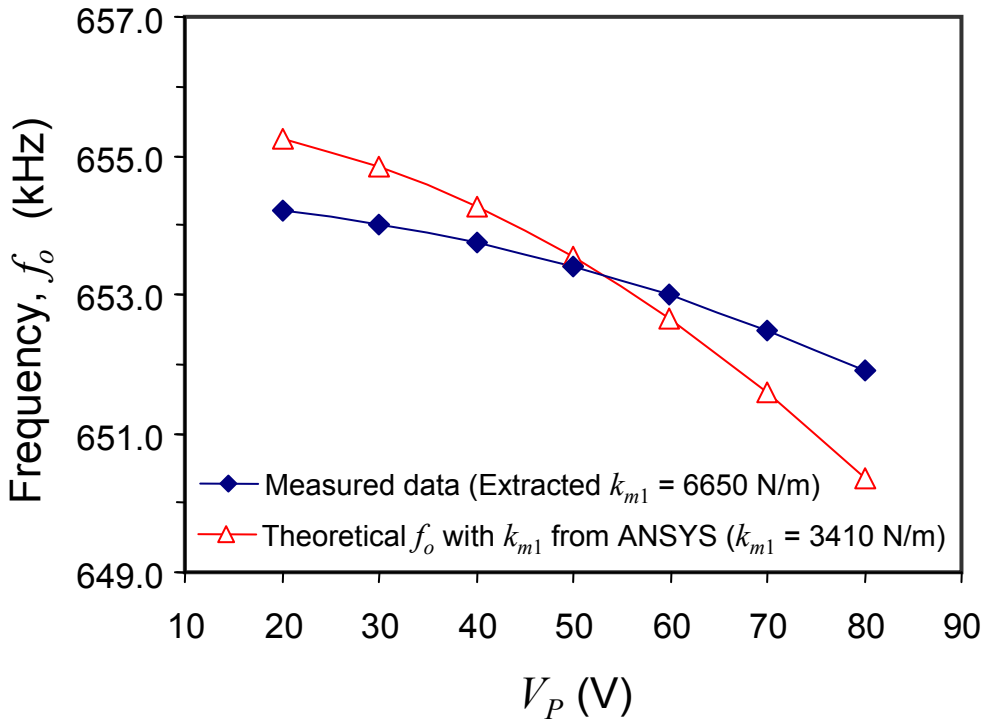

Figure 5.3: Measured resonant frequency vs. V_P, along with extracted k_{m1} value. Theoretical f_o values are calculated using k_{m1} value from ANSYS simulations.

Although the error in predicting resonant frequency is not very significant, the value of k_{m1} deviates quite considerably. That is, the extracted k_{m1} from measured data is about twice that extracted using ANSYS. Therefore for nonlinear studies, where quadratic and cubic spring constant terms (k_{m2} and k_{m3}) play a major role, predicting nonlinear behavior with extracted k_m values from ANSYS may be inadequate. The semi-analytic method presented in [99] is quite efficient in predicting higher order nonlinear spring constants, and it predicts that the overall cubic spring constant k_3 for this device is about 2285.05 μN/μm^3. The electrical cubic spring constant k_{e3} at high V_P of 100V is roughly 38.7 μN/μm^3, which is only 1.7% of k_3. Therefore, the value of k_{m3} is very large and dominates the cubic spring constant, which accounts for the spring hardening nonlinear behavior of the device.

Figure 5.4 shows the measured response curve for V_P = 50V and v_{ac} = 420mVpp, obtained with upward and downward frequency sweep showing two sharp 'jump' transitions. The bounded region between two jumps is an unstable part of the response that cannot be measured experimentally [98-100]. This unstable region is outlined with a dotted trace between the two jumps in Figure 5.4. The larger the AC drive amplitude the more the hysteresis loop will expand, and the extent of which can be observed by sweeping the frequency upward and then downward for different drive conditions.

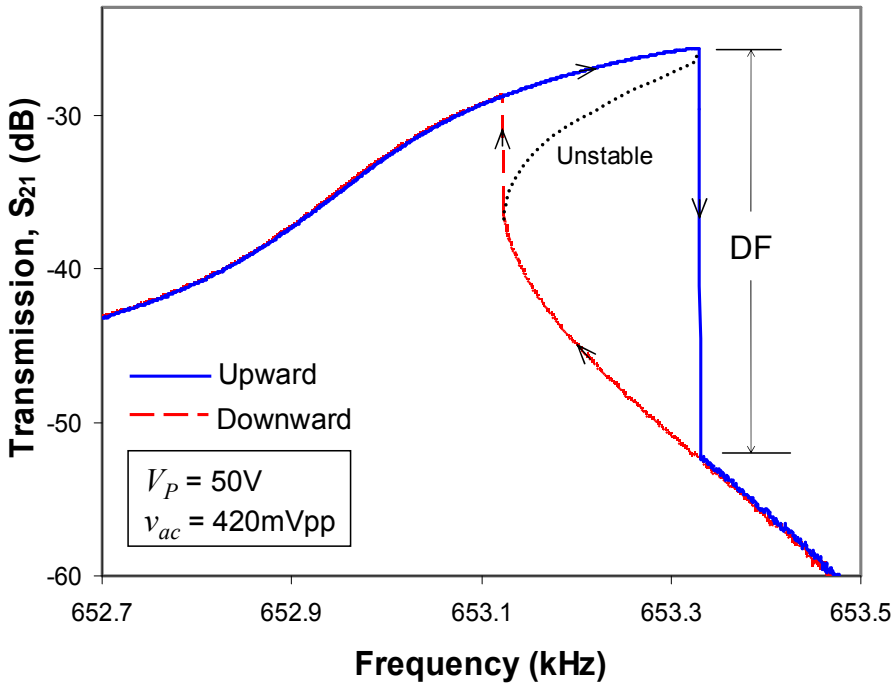

Figure 5.4: A hysteresis loop illustration with upward and downward frequency sweep taken at V_P = 50V and v_{ac} = 420mVpp. The Duffing Factor (DF) is defined for an upward sweep.

For quantification of the amount of Duffing nonlinearity, a term "Duffing Factor" (DF) is introduced, which is defined as the largest drop in the transmission curve, or the largest difference between the consecutive S_{21} transmission dB values, as illustrated in Figure 5.4. This term can be used for careful analysis of early stages of nonlinear distortions.

Figure 5.5 shows the DF extracted for fundamental-mode Free-Free beam resonator biased at different V_P and v_{ac} amplitudes. For low v_{ac} below a critical value, there is hardly any Duffing nonlinearity despite increasing V_P bias.

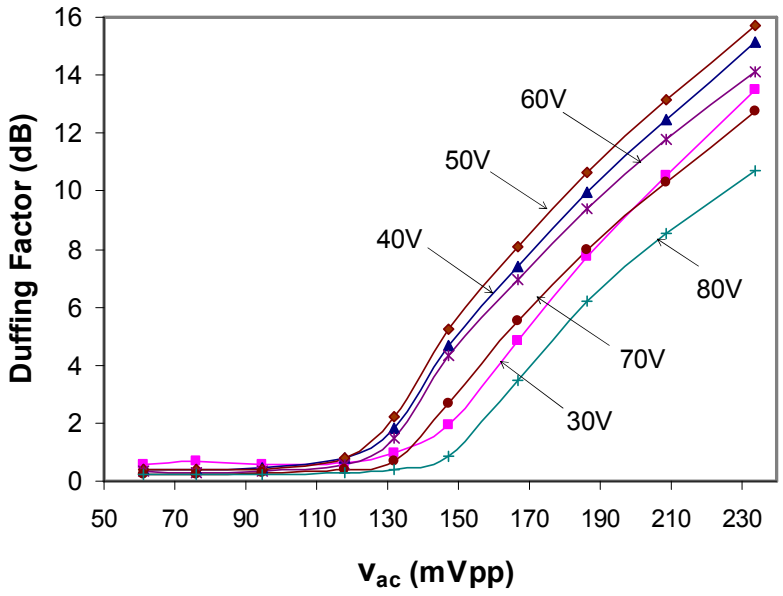

Figure 5.5: Plot of Duffing Factor (DF) versus v_{ac} increase for each of the fixed V_P value.

If the threshold for Duffing is decided at the level of DF=1dB, then the corresponding critical v_{ac} is around 120mVpp. With the drive conditions of v_{ac} less than 120mVpp at different V_P, the resonator displacement was estimated (using experimental Q values) to be less than 50nm, which is less than 2.5% of the 2μm electrode-to-resonator gap. Therefore, at small vibrations nonlinearity is not observed even though electrostatic force is increased with larger V_P bias. Beyond this critical point, an increase in v_{ac} results in larger Duffing nonlinearity indicated by much larger DF. This dependence of DF on v_{ac} follows a linear relationship that can be experimentally approximated as

$$DF \approx \left(v_{ac} \cdot 0.125\right) dB/mV\,, \tag{5.16}$$

where DF is in dB scale, and v_{ac} in AC drive voltage peak-to-peak, which means 8mVpp rise in AC voltage is required for 1 dB rise in DF.

For large AC drive beyond 120mVpp, as shown in Figure 5.5, the Duffing behavior is largely mechanical-based. For example, for a fixed v_{ac} of 150mVpp in Figure 5.5, different V_P values cause significant change in DF, indicating nonlinear behavior is dependent on the DC bias voltage. However for low v_{ac} values, it is possible that both softening due to electrical and hardening due to mechanical compensating one another, resulting in DF almost constant for increasing V_P bias as long as AC drive is below the critical value of 120mVpp. This result can be useful in applications where DC-bias voltage tuning is needed without introducing nonlinearity.

For the combined effect of V_P and v_{ac} conditions, the points at which hysteresis begins to occur are recorded for different V_P and v_{ac} values, as shown in Figure 5.6. The 'hysteretic point' corresponds to the point below which S_{21} transmission curve is almost identical for upward and downward frequency sweeps. Above hysteretic point the response is no longer single-valued and jumps occur for both upward and downward.

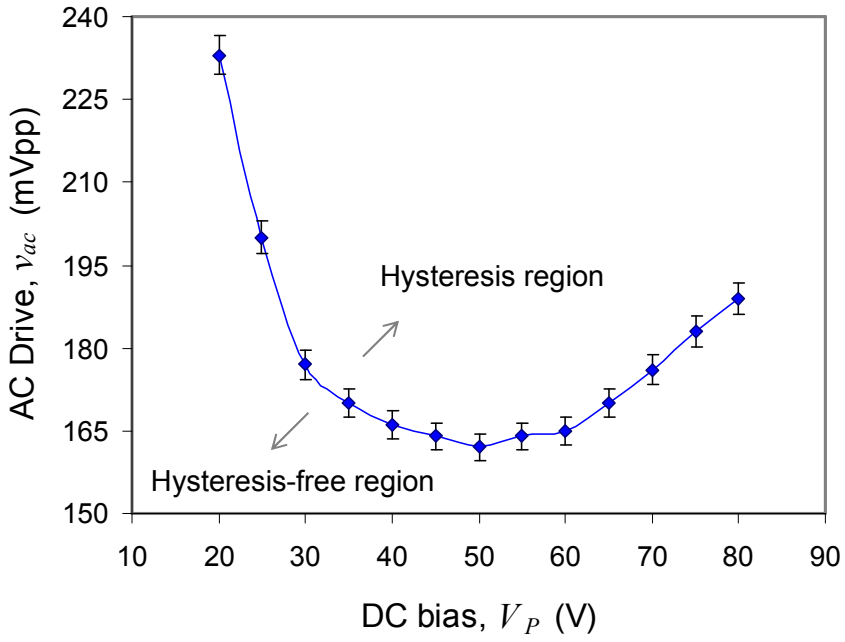

Figure 5.6: A plot of measured V_P and v_{ac} combinations at which nonlinear hysteresis begins to develop. Below this curve is hysteresis-free region, where the frequency response is almost identical for upward and downward sweeps.

The curve in Figure 5.6 is produced by connecting such hysteretic points, and it defines a boundary line that divides the hysteresis region and hysteresis-free region. In Figure 5.6, smaller v_{ac} is needed for hysteresis to develop as V_P is increased because the electrostatic force is proportional to ($V_P \cdot v_{ac}$). However, beyond V_P = 50V the spring softening effect due to electrical nonlinearity partly cancels the hardening due to mechanical, so that more v_{ac} drive is required to induce the hysteresis.

It is usually difficult to predict using FEM tools whether cancellation of mechanical nonlinearity and electrical nonlinearity would happen for a given resonator. Moreover, the electrode gap of the resonator used in our study is large at 2μm and it is difficult to experimentally show the electrical nonlinearity dominance over the mechanical nonlinearity. Nonetheless, the cancellation phenomenon can be shown for 2μm-gap resonator having low mechanical stiffness, as reported by Shao, *et al*. [101] for a 193kHz Clamped-Clamped beam resonator where the first-order cancellation between the mechanical and electrical nonlinearities is observed experimentally. Nonlinearity cancellation is also reported in [96] to improve the overall maximum output current. Therefore, nonlinearity cancellation boosts the critical vibration amplitude of the resonator, which leads to better power handling capability.

5.4 Nonlinearity of bulk-mode resonators

In this section, nonlinear behaviors of Lamé-mode square resonators and wine glass mode disk resonators are presented. The study of nonlinearity in bulk-mode resonators has been reported previously in [90, 91, 102], however, the study is in early stage of

development and more work is needed to fully understand their nonlinear response. Nonlinear behavior of length-extensional and square-extensional bulk-mode resonators are reported to be of spring softening type [90, 102]. Spring softening nonlinear response is also observed for bulk-mode resonators of this work.

Measured transmission curves for 6.35MHz Lamé-mode resonator with straight-beam anchors driven at fixed V_P =60V and different v_{ac} is shown in Figure 5.7. The frequency is swept downward and shows the spring softening nonlinearity. More detailed plots of upward and downward frequency sweeps are shown in Figure 5.8.

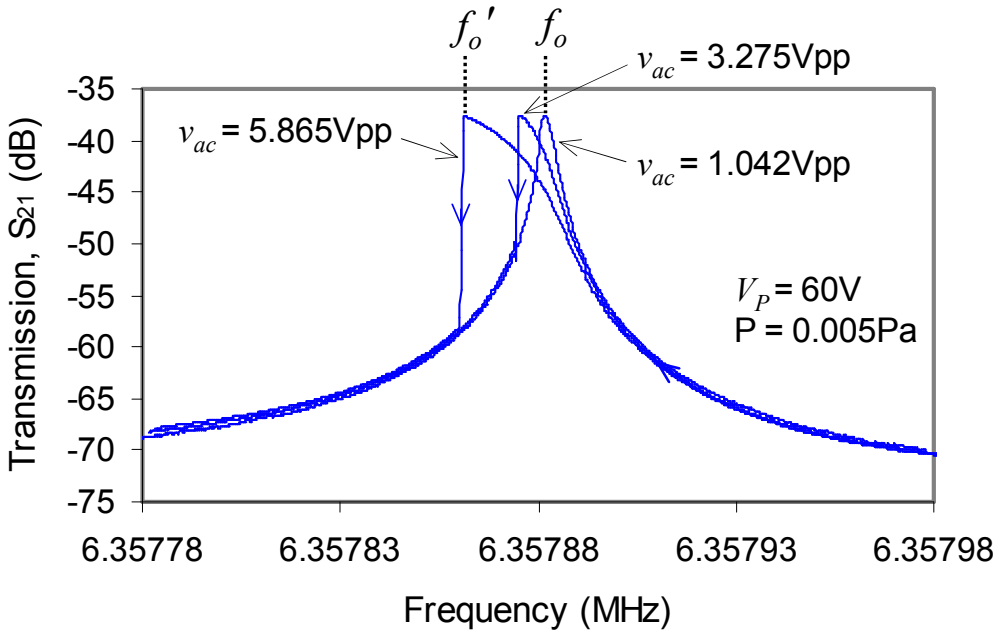

Figure 5.7: Measured S_{21} transmission curves for different v_{ac} at fixed V_P = 60V. The frequency is swept downward and shows the *spring softening* nonlinearity of Lamé-mode square resonator. As to compare the frequencies at 1.042Vpp and 5.865Vpp, the difference $(f_o - f_o')$ = 20Hz.

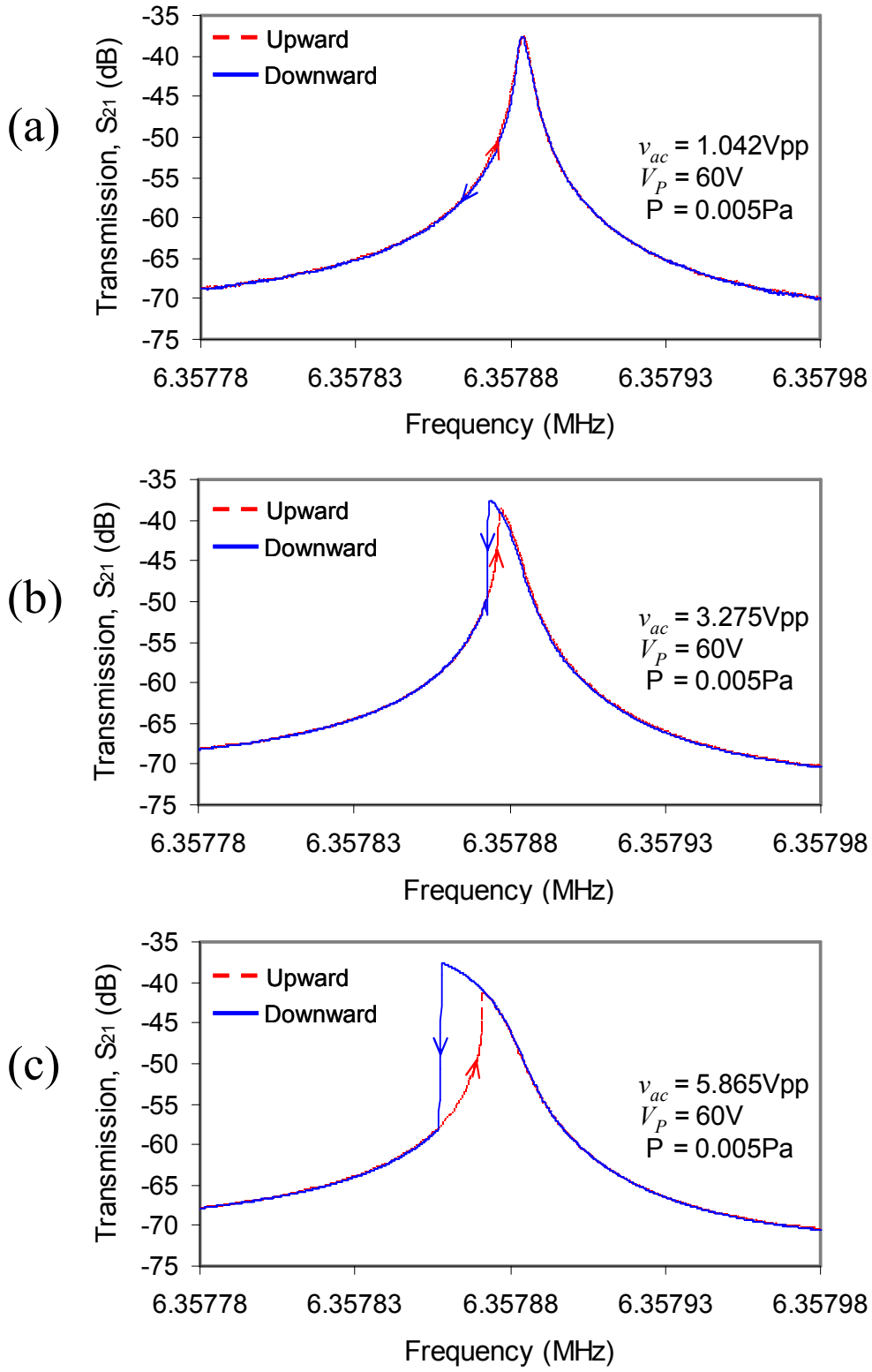

Figure 5.8: Nonlinear response of Lamé-mode square resonator at various v_{ac}: (a) = 1.042Vpp, (b) 3.275Vpp, and (c) 5.865Vpp, all at V_P = 60V. Both upward and downward frequency sweeps are shown.

The transmission response in Figure 5.8(a) is a single-valued function for v_{ac}=1.042Vpp. As the v_{ac} is increased to higher levels, the frequency response bends toward lower values and eventually causes a jump with frequency hysteresis. Using the semi-analytic method described in [99] the cubic mechanical spring constant (k_{m3}) is extracted as -2.40×10^{15} N/m^3, which also corresponds to large negative value of the nonlinear parameter κ from equation (5.8).

The spring softening nonlinearity is observed for wine glass disk resonators as well, and a micrograph of tested resonator can be seen in Figure 3.10(b). Measured transmission curves for 6.8MHz wine glass mode disk resonator is shown in Figure 5.9, driven at several v_{ac} and fixed $V_P = 100$V.

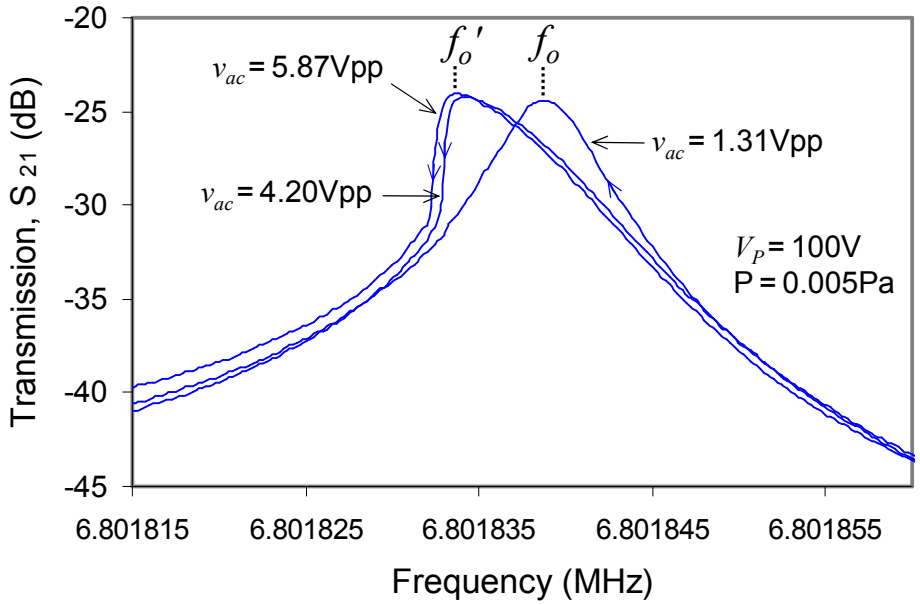

Figure 5.9: S_{21} transmission curves for 6.8MHz wine glass disk resonator at different v_{ac} and fixed $V_P = 100$V. The frequency is swept downward showing spring softening nonlinearity. The difference ($f_o - f_o'$) of the resonant frequencies at 1.31Vpp and 5.87Vpp is only about 5Hz.

At 100V and 5.87Vpp drive, the new resonant frequency f_o' is only about 5Hz away from the resonant frequency f_o without nonlinearity at lower AC drive. In

comparison, for Lamé-mode square resonator at the same v_{ac} level of 5.87Vpp and at 60V, the difference $(f_o - f_o')$ is about 20Hz as shown in Figure 5.7. Therefore, this particular disk resonator is able to take more power with very little nonlinear hysteresis compared to the Lamé-mode square resonator design. This better power handling of the disk resonator can be explained partly by 1.8× higher linear mechanical spring constant k_{m1}, as listed in Table 3.3, than that of the square resonator. The amount of resonant frequency shift $(f_o - f_o')$ due to Duffing is directly related to the nonlinear parameter κ, and κ is inversely proportion to k_1.

One observation regarding Lamé-mode square resonators is that longer and flexible anchor beams give rise to nonlinear vibrations more easily at lower DC bias and AC drives than shorter anchor beams. From nonlinear response of square resonators with straight-beam anchor designs 4A ($L_a \times W_a$ = 60μm ×10μm), 4B (120μm ×10μm), and 4C (320μm×10μm), a set of v_{ac} and V_P values are obtained at the point of hysteresis. These points are at drive conditions just before upward and downward frequency sweeps of S_{21} response are no longer the same with hysteresis loop. In Figure 5.10, AC-DC hysteresis points that form a boundary line for the three designs 4A, 4B, and 4E are plotted. Above this boundary line, square resonator is in nonlinear region with hysteresis, below which resonator is in linear region. The results show that square resonators with longer anchor beams go into nonlinear region at lower v_{ac} for the same V_P bias. However, the advantage of square resonator with long anchor beams over the one with short anchors is that it is easier to excite to give strong signal-to-noise performance at a lower V_P bias. This is due to the bulk of the square resonator able to vibrate more freely with longer anchor beams attached at the four corners. It depends on the type of application whether short or long anchor beam is more suitable.

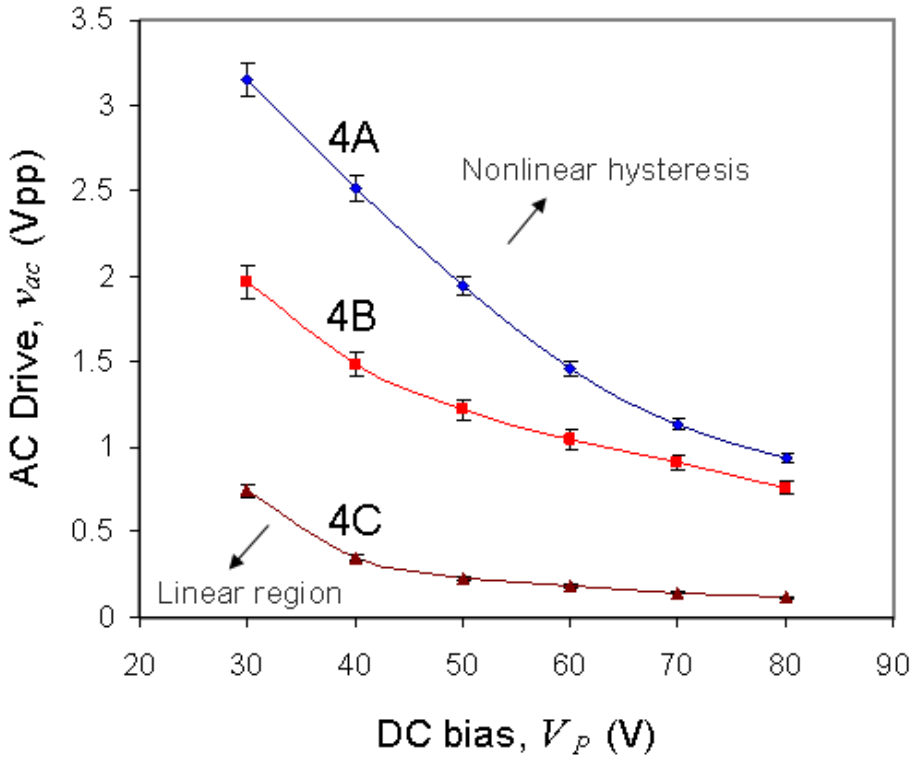

Figure 5.10: A plot of AC - DC hysteresis points that form a boundary line, above which square resonator is in nonlinear region with hysteresis, below which it is in linear region. Comparison of designs 4A (60μm×10μm), 4B (120μm×10μm), and 4C (320μm×10μm) shows that squares with longer anchor beams go into nonlinear more easily at lower drive conditions.

Therefore, square resonator with very short anchor beams will have high Q and hardly exhibit nonlinear behaviour, but require larger drive conditions for a good signal-to-noise performance. Very long anchor beams on the other hand, results in slightly lower Q, easier to be driven into nonlinear region, but provides large vibration amplitude at lower V_P bias. Experimental results reveal that for different combination of L_a and W_a of the anchor beam, there are design trade-offs between Q, R_m, and power handling. Depending on whether quality factor, motional resistance, or power handling is the priority for a certain application, a set of optimal anchor beam length and width combination can be chosen.

5.5 Comparison of flexural-mode and bulk-mode resonators

In this section, power handling capability of flexural beam resonators will be compared to that of bulk-mode square resonators. The dimensions of the flexural beam resonators need to be reduced to scale for higher operating frequency range. Hence, the signal-to-noise ratio (SNR) of much smaller flexural resonators is also decreased. However, within a given layout area for the device, bulk-mode resonators with much higher mechanical stiffness can operate at higher resonant frequency and achieve ultra-high Q compared to flexural-type resonators.

From nonlinear response of fundamental-mode Free-Free beam from Section 5.3, the hysteresis loop is much larger compared to bulk-mode square and disk resonators under the same drive conditions. For the second-mode Free-Free beam shown earlier in Figure 2.3, there are only one support beam at each of the three nodal points, thus leading to lower axial stiffening force along the beam compared to the fundamental-mode version. Therefore, measured results of second-mode Free-Free beam display spring softening nonlinearity, unlike the hardening type of the fundamental-mode Free-Free beam resonator.

The second-mode Free-Free beam resonator (in Figure 2.3) and Lamé-mode square resonator (in Figure 3.8) both display spring softening nonlinearity. The linear mechanical spring constant k_{m1} of second-mode Free-Free beam resonator is 6702 N/m and that of the Lamé-mode square resonator is 2.155×10^7 N/m [99]. Since the k_{m1} of the softer Free-Free beam resonator is significantly lower than the Lamé-mode square resonator, the vibration amplitude of the beam is much larger under the same drive conditions, leading to much more pronounced nonlinear behavior.

Figure 5.11 shows the S_{21} transmission response of Lamé-mode resonator and second-mode Free-Free beam resonator tested under the same drive of v_{ac} = 1.322Vpp and V_P = 60V. The transmission curve of Lamé-mode resonator is still single-valued plot without hysteresis, whereas the resonant frequency of Free-Free beam resonator is shifted by -1000ppm with large hysteresis loop. Hence, the Free-Free beam resonator is much easier to be driven into nonlinear region while the Lamé-mode resonator can take more power before showing signs of nonlinearity.

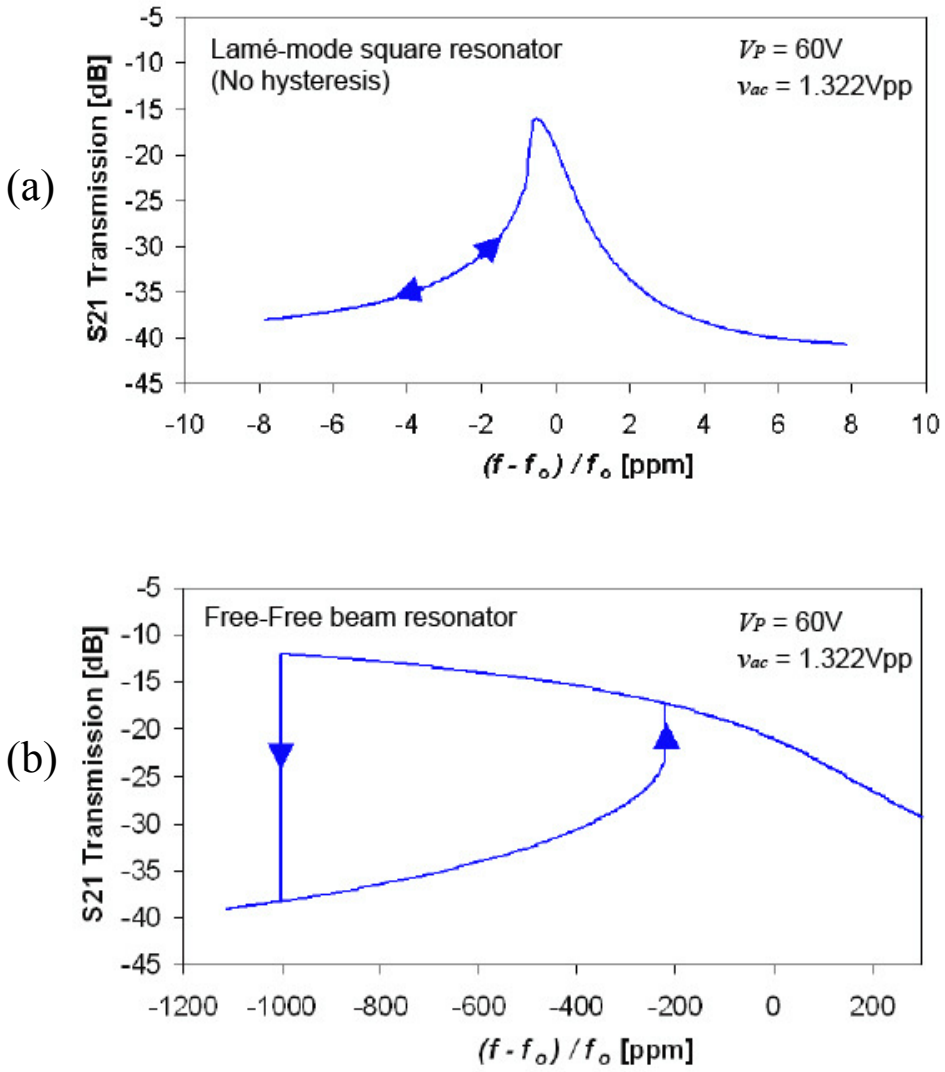

Figure 5.11: S_{21} transmission curves measured at v_{ac} = 1.322Vpp and V_P = 60V for the (a) Lamé-mode square resonator and (b) second-mode Free-Free beam resonator. [Source: 99]

With regard to the maximum stored energy, $E_{stored}^{\max}$, the Lamé-mode square resonator has three orders of magnitude larger energy storage capacity compared to the second-mode Free-Free beam resonator [91]. Better power handling (or higher energy storage) along with ultra-high quality factor of the Lamé-mode square resonator could provide superior phase noise performance, according to Leeson's formula in equation (5.4), if the square resonator is used in oscillator application.

When a flexural beam resonator is implemented into a closed-loop oscillator, vibration amplitude control circuit is usually required to limit the distorted time-domain oscillation. Automatic-level control methods reported in [21] that limit the vibration amplitude of the 10MHz Clamped-Clamped beam oscillator are shown to improve the close-to-carrier phase noise. Comparison of time-domain oscillations from Lamé-mode square oscillator and Free-Free beam oscillator, both without any amplitude limiting circuit, shows that the output of Free-Free beam oscillator is distorted by higher order harmonics arising from nonlinear vibration, whereas the Lamé-mode oscillator is able to generate a clean sinusoidal wave [103]. Therefore, Lamé-mode square oscillator is much less susceptible to nonlinearity and produces no significant signs of nonlinear vibration.

Closed-loop circuit for oscillator and phase noise measurement setup is shown in Figure 5.12(a), reported by our group in [104]. From phase noise performance of both square and beam oscillators shown in Figure 5.12(b), the close-to-carrier phase noise of the Lamé-mode oscillator performs much better than that of the Free-Free beam oscillator. At 10Hz offset from the carrier frequency, phase noise of the Lamé-mode oscillator is 42dB lower than that of the Free-Free beam oscillator [104]. Moreover, the Free-Free beam oscillator exhibits the $1/f^6$ phase noise component while the Lamé-mode oscillator has $1/f^2$ phase noise. A sudden increase in the close-to-carrier phase noise, the

$1/f^6$ component in this case, is believed to be caused by the hysteretic instability arising from the vibration amplitude of the resonator that is increased beyond the critical Duffing point (X_C) [21, 105]. Hence, large nonlinear vibrations of the Free-Free beam have severely degraded the close-to-carrier phase noise.

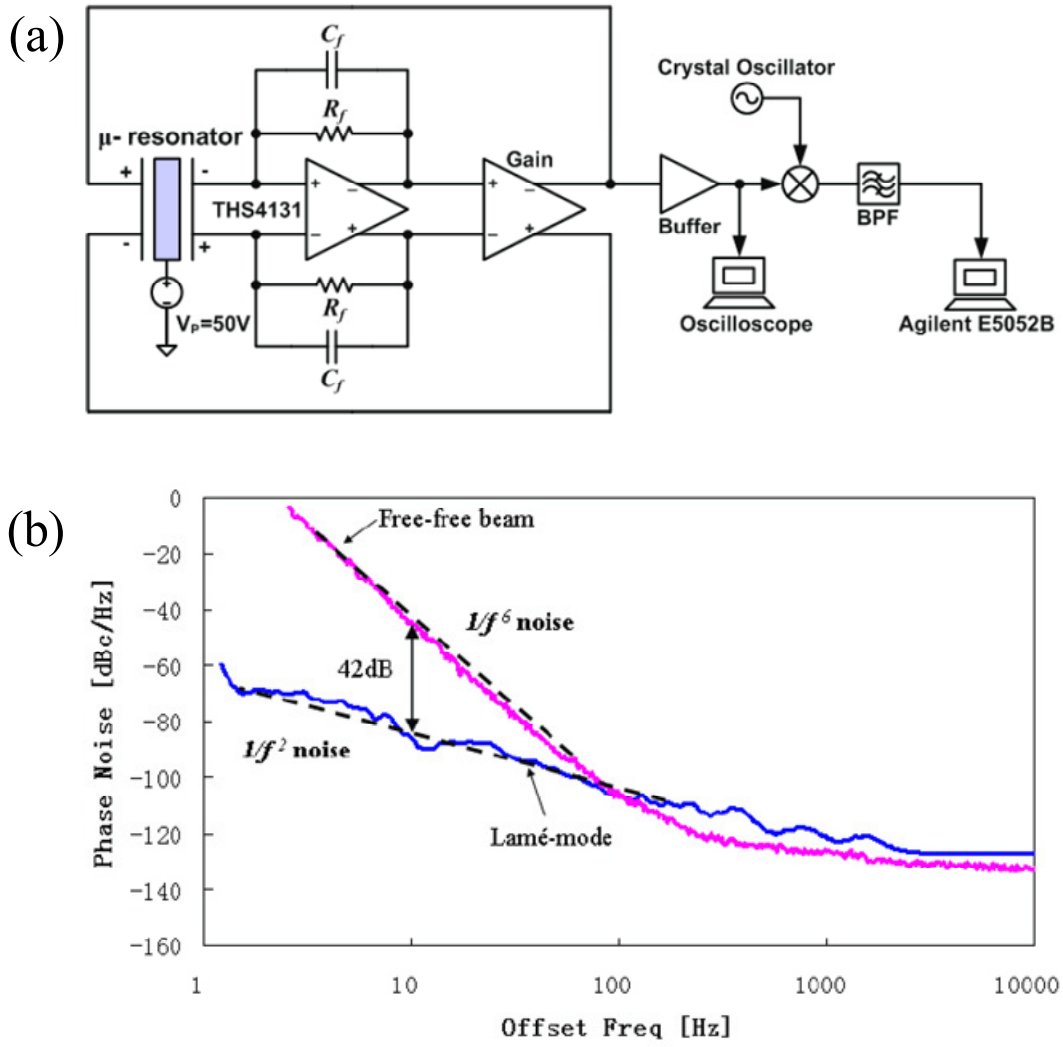

Figure 5.12: (a) Schematic of closed-loop circuit for oscillator and phase noise measurement setup, (b) Phase noise performance of Lamé-mode square oscillator and Free-Free beam oscillator. [Source: 104]

The expected $1/f^2$ phase noise component from theoretical prediction, according to the second term of equation (5.4), is observed for the Lamé-mode oscillator indicating

that the effect of nonlinearities is minimal for the Lamé-mode resonator. Therefore, Lamé-mode resonator and other bulk-mode resonators having similar nonlinear behavior could be implemented as oscillator without amplitude-level control circuitry, and still perform well with low phase noise. Such characteristic would simplify the circuit design and bulk-mode resonators have great potential in reference oscillator applications.

5.6 Summary

In summary, both mechanical nonlinearity and electrical nonlinearity of micro-mechanical resonators have been presented in this section. The effect of nonlinearities on the performance of Free-Free beam, Lamé-mode square, and wine glass disk resonators were investigated. The results show that nonlinearities not only destabilize the resonant frequency, but also limit the vibration energy storage and hence place a limitation on the power handling capability of the resonator. The nonlinearity of fundamental-mode Free-Free beam resonator presented in this section had spring hardening behavior, which shifts the resonant frequency to higher value. However depending on the support beam and resonator design, a flexural beam resonator can exhibit spring softening or hardening nonlinear behavior. Appropriately designed beam resonator could provide with a cancellation between the mechanical and electrical nonlinearities, which could improve the overall maximum output current and therefore better power handling of the resonator.

The nonlinearities of bulk-mode 6.35MHz Lamé-mode square resonator and 6.8MHz wine glass disk resonator are of spring softening type. The wine glass disk

resonator presented here had higher mechanical stiffness than the Lamé-mode resonator and observed to have better power handling capability. The length of anchor beams could also contribute to nonlinearity of bulk-mode resonators. Lamé-mode square resonator with long anchor beams exhibited nonlinear behavior at lower drive power compared to the results of square resonators with short anchors.

When comparing the power handling of flexural beam resonator and Lamé-mode resonator, the Lamé-mode resonator is much less susceptible to nonlinear effects and can store three orders of magnitude larger vibration energy before the frequency hysteresis occurs. Therefore, better power handling along with ultra-high quality factor of the bulk-mode resonators could provide superior phase noise performance in oscillator applications. The closed-loop feedback response further demonstrates that the Lamé-mode square based oscillator is able to achieve 42dB lower phase noise at 10Hz offset from the carrier frequency than the flexural-mode beam oscillator [104].

Besides the quality factor and power handling as important parameters for reference oscillator applications, the stability of oscillating frequency under various temperatures is also just as important. The shift in frequency with temperature is unavoidable for micromechanical resonators, which is caused by the thermal expansion of structural material and the temperature dependence of Young's Modulus. The following chapter discusses the stability of resonant frequency under various temperatures in more detail.

Chapter 6

Temperature Stability and Compensation of Resonator Oscillator

When gauging the performance of micromechanical resonators for a particular application, the quality factor, power handling and pressure stability presented in previous chapters should be carefully assessed. Another important parameter is the temperature coefficient of frequency (TC_f), which is a measure of changes in the resonant frequency with temperature. Changes in temperature result in corresponding changes in the mechanical elastic properties of the structure that eventually leads to resonant frequency drift. Large amount of resonant frequency drift with temperature is useful for some applications such as temperature sensors, but it is undesirable for timing reference applications. Therefore, a method of temperature compensation is necessary for reference oscillators. This chapter highlights the temperature dependence of resonant frequency and we propose a new method of temperature compensation for oscillators.

6.1 Temperature coefficient of resonant frequency

Silicon and polysilicon micromechanical resonators have large TC_f values mainly due to the thermal dependence of Young's modulus. Large TC_f value could also be due to the

differences in the thermal expansion of the structural material and the substrate [106-108]. The TC_f values of reported silicon resonators, which are not under heavy compressive or tensile stresses, are usually in the range of –20ppm/°C to –30ppm/°C regardless of the resonators are flexural-mode or bulk-mode type. However, differences in the thermal expansion of structural material and the substrate could enhance the temperature sensitivity of the resonator, which can lead to large TC_f around –90ppm/°C for Clamped-Clamped beam resonator [107] or even higher to –170ppm/°C for doubly-clamped tuning fork resonator [108].

Therefore, the uncompensated TC_f for silicon resonators are usually 15–20 times larger than that of quartz crystals. Quartz crystals can be cut in such a way to minimize frequency drift due to temperature, such as AT-cut quartz resonators that have uncompensated temperature coefficients (TC_f's) on the order of ±100 parts per million (ppm) for –55°C to 125°C temperature range [109].

For applications where stable frequency is desired over a large temperature range such as for reference oscillators, large negative TC_f of micromechanical resonators pose a challenge and some form of temperature compensation is required. One common temperature compensation method is the digital compensation using a temperature sensor and external CMOS circuits. For example, in a fully programmable oscillator SiT8002 from SiTime, such digital compensation can provide less than ±50 ppm frequency variation over –40°C to +85°C range [110].

Depending on the size, geometry and the type of resonator, fractional changes in resonant frequency could be either *linear*, *quadratic* or even *cubic* function of temperature over a large temperature range. Frequency response of some of the AT-cut quartz crystal resonators are shown to exhibit cubic dependence on temperature [109].

Whereas for watch-grade tuning fork quartz resonators and micromechanical double-ended tuning fork resonators of the work by [111], frequency-temperature relationship is of quadratic type. The clamped-clamped beam, free-free beam and bulk-mode silicon resonators usually have linear f_o–temperature relationship. The frequency changes with respect to reference frequency f_o can be expressed generally in Taylor expansion form as

$$\frac{\left(f(T)-f_o\right)}{f_o}=\sum_{n=1}^{\infty}TC_{f(n)}\cdot\left(T-T_o\right)^n, \tag{6.1}$$

where T_o is the reference temperature, $f(T)$ is the frequency at some temperature T, and $TC_{f(n)}$ is the nth order temperature coefficient of frequency. The term $TC_{f(n)}$ is

$$TC_{f(n)}=\frac{1}{n!*f_o}\left(\frac{\partial^n f(T)}{\partial T^n}\right)\Bigg|_{T=T_o} \tag{6.2}$$

In fact, the equation (6.2) can be used to express temperature dependence of any geometric or material parameter by replacing the term "f" with appropriate symbol. Figure 6.1 shows the resonant frequency changes with temperature reported in [107] for clamped-clamped beam resonators driven by comb electrodes fabricated in SOIMUMPs.

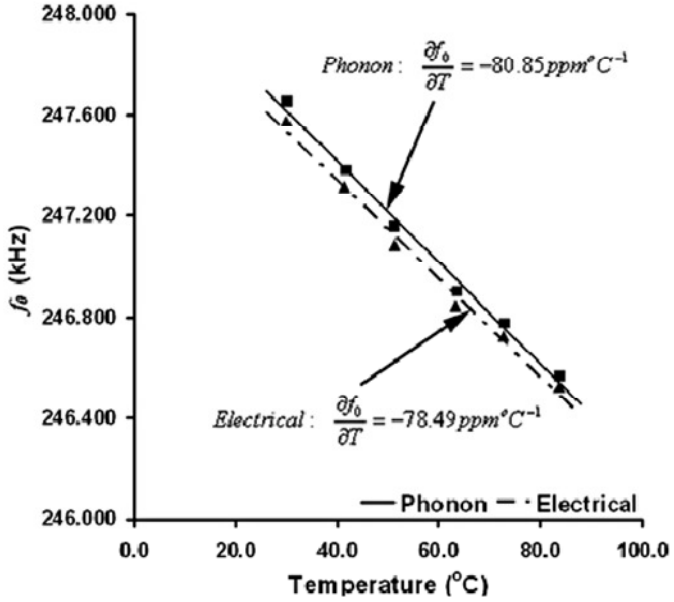

Figure 6.1: Resonance frequency f_o shift with temperature for clamped-clamped beam resonator measured by both acoustic phonon detection and electrical characterization methods [107].

Both methods of acoustic phonon detection and electrical characterization confirm that resonant frequency changes linearly with temperature. The TC_f values are in the range of –80ppm/°C to –90ppm/°C for these types of beam resonators that are under axial stress at both fixed ends.

For bulk-mode Lamé square resonators that have been discussed in Chapter 3, the resonant frequency is also linearly dependent on temperature. Figure 6.2 shows measured TC_f of three 6.35MHz square resonators that have different geometric design.

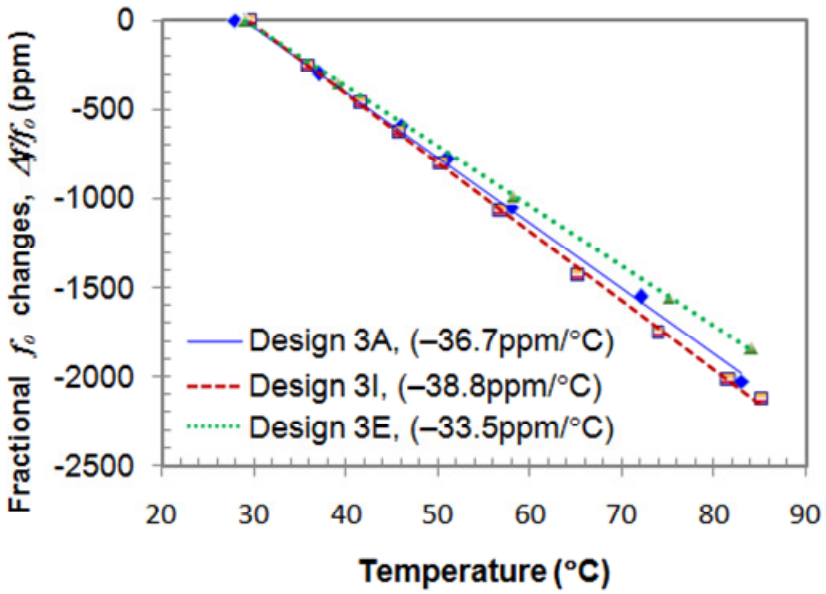

Figure 6.2: Changes in resonant frequency with temperature for 6.35MHz Lamé-mode square resonators: design **3A** (60µm ×10µm anchors) with –36.7ppm/°C, design **3I** (320µm ×10µm anchors) with –38.8ppm/°C, and design **3E** (release etch-holes all over) with –33.5ppm/°C.

The TC_f of Lamé-mode square resonators were observed to be roughly the same value regardless of the differences in the resonator design. Therefore, for silicon resonator to be implemented as oscillators, a good method of compensation is required to offset the resonant frequency drift with temperature. The following section reviews existing methods of temperature compensation reported in literature.

6.2 Review of different compensation techniques

Some of the other reported temperature compensation techniques in literature include mechanical means of stress compensation with specially designed geometry [106, 112], localized heating of the resonator [108], or compensations based on electrostatic tuning of the bias voltage (V_P) to the resonator [113, 114]. Some of these methods compensate frequency changes by using materials having mismatched coefficient of thermal expansion to axial stresses induced within the resonator. Furthermore, another approach is to offset the large negative temperature coefficient of silicon by coating the resonator with a material that has positive temperature coefficient of Young's modulus such as SiO_2 [111]. For some type of resonators whose quality factor (Q) is dependent on temperature, the Q itself could be used as a thermometer for compensation [115].

Each of the compensation techniques has its own benefits and drawbacks. For example, due to variations in the thickness, thin film coating with SiO_2 could lead to unpredictable TC_f values that vary from device to device. For electronically compensated resonators, an external precise temperature sensor is typically required at a different location away from the resonator, which could lead to inaccurate compensation due to temperature gradient between the sensor and resonator. Nevertheless, a careful resonator design that is temperature compensated with a combination of two or more of the methods described above, the TC_f value of micromechanical oscillator could potentially be very low in the order of several parts per billion (ppb).

High performance temperature sensor is an important component of the digital temperature compensation. The sensor must be located in close proximity to the resonator such that there is little thermal gradient between sensor and resonator. The

most accurate temperature sensor of course is the resonator itself. Resonator self-temperature-sensing has previously been proposed for quartz crystal oscillators using the "beat frequency method" of mixing the two signals from dual harmonic mode excitation [116, 117]. This result in nearly linear dependence of beat frequency on temperature, and the obtained information can be used in compensation of either one of the dual-mode signals.

For micromechanical resonators, the beat frequency method has been used for two independent oscillators based on Double Ended Tuning Fork (DETF) resonators [118]. The two resonant frequencies of the DETF resonators are set roughly the same, while their temperature coefficients are designed to be different through addition or removal of stresses at the ends of tuning fork tines. The end result is higher sensitivity to temperature for the beat frequency signal after mixing, which serves as a temperature sensing mechanism. For bulk-mode micromechanical resonators, a temperature sensing method is also reported recently in [119] utilizing the two bulk acoustic modes of square resonator (namely, square-extensional mode and Lamé mode). This method is rather promising; however, its main disadvantage is that the resonant frequencies of the two modes are close to each other, which would require an accurate frequency measurement. As presented previously in Chapter 3, the resonant frequency hardly changes with DC bias V_P for bulk-mode resonators unlike the flexural beam resonators. Hence, compensation that uses the electrostatic tuning of V_P is not very effective for bulk-mode.

We present a method of temperature compensation in the following section. No external temperature sensor is required with this compensation approach. Our method could be used for any type of resonator including bulk-mode resonators. Our method is based on *difference frequency mixing* of two oscillations to generate a beat frequency

that is used as the reference oscillation. One of the two oscillations comes from two Lamé-mode square resonators in one positive feedback closed-loop, and the other oscillation comes from a beam resonator in another feedback loop. The beam is placed at the middle and joins the two square resonators. As to verify our compensation concept, the composite structure is tested with system-level circuit implementation. After frequency mixing, the TC_f of final reference oscillation improved without using any special compensation electronics.

6.3 Composite resonator design for compensation

Micrograph of the composite resonator is shown in Figure 6.3. It is made up of two square resonators designed to vibrate in Lamé mode and a bridging beam is placed in between the squares. We have reported the preliminary test results of this design in [120]. The side length L_s of the squares is 650μm, and the beam length (L_b) and width (W_b) are 720μm and 25μm, respectively. The electrode-to-resonator gap is 2μm.

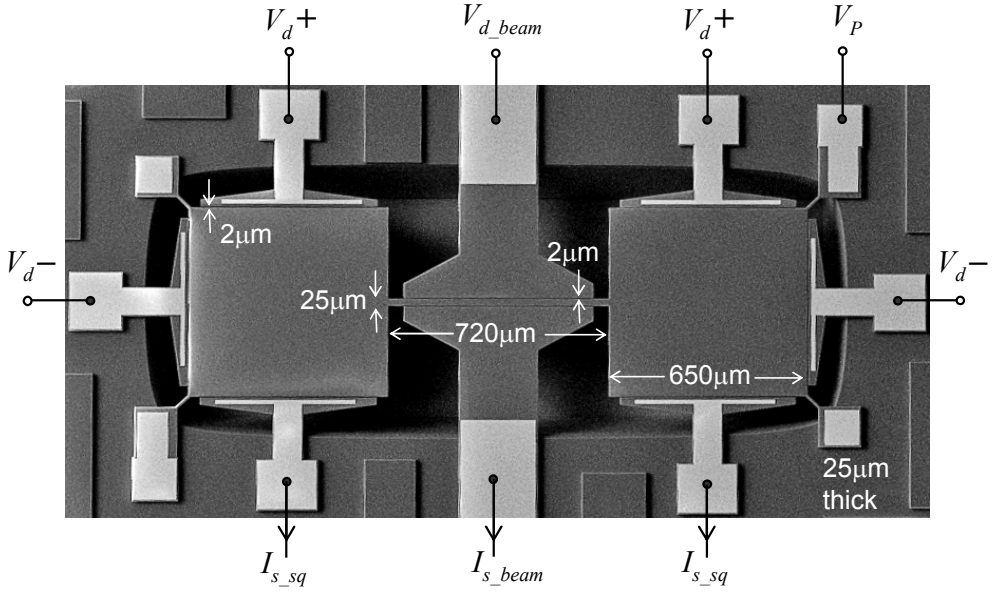

Figure 6.3: SEM micrograph of the composite resonator and its geometric dimensions.

Finite element simulation in ANSYS for the beam resonator and square resonators is shown in Figure 6.4. The middle beam is bounded by large square plates at both ends and the beam vibrates almost as a Clamped-Clamped beam shown in Figure 6.4(a). Lamé-mode vibration of the square resonators is in sync shown in Figure 6.4(b).

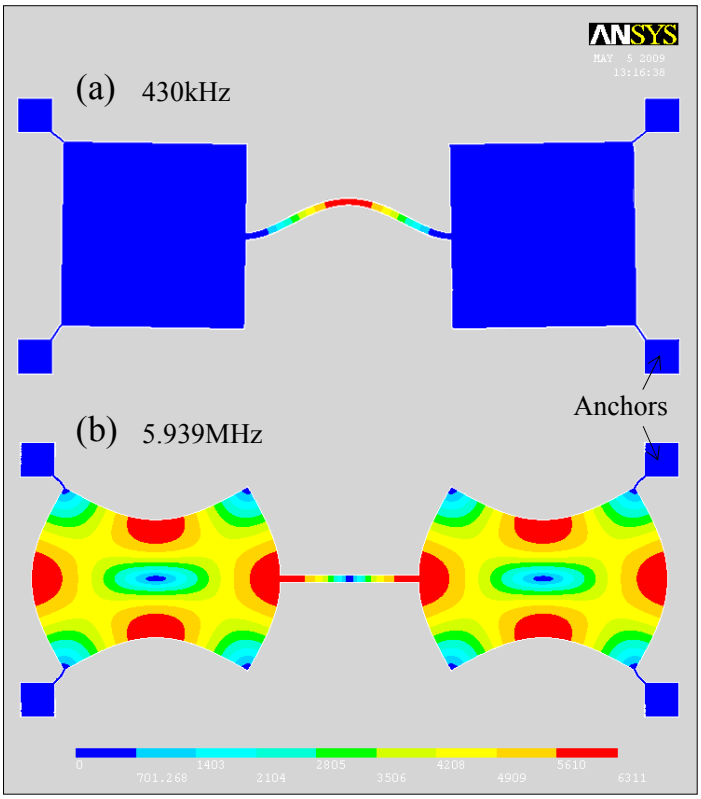

Figure 6.4: Simulation results of mode shape in ANSYS, (a) for the middle beam with Clamped-Clamped vibration, and (b) the square resonators in Lamé-mode resonance.

From analytical model for a free-standing square plate, the resonant frequency (f_s) of square resonators in Lamé mode according to equation (2.7) is

$$f_s = \frac{1}{\sqrt{2}L_s} \cdot \sqrt{\frac{C_{44}}{\rho}}, \tag{6.3}$$

where C_{44} term is the shear modulus and ρ is the density. C_{44} measured for silicon is 79.6GPa. If the middle beam with end-to-end length (L_b) vibrates in length-extensional mode, its resonant frequency (f_{ext}) can be calculated by equation (2.6) as

$$f_{ext} = \frac{1}{2L_b} \cdot \sqrt{\frac{E}{\rho}}, \tag{6.4}$$

where E is the Young's modulus. For silicon structural layer of SOIMUMPs, estimated values are E=179GPa and ρ=2330 kg/m^3. Then the value of f_{ext} calculated is 6.1MHz.

If the middle beam is driven into lateral motion perpendicular to its length-extensional mode, its movement can be regarded as that of a Clamped-Clamped beam. Then, the expression for the beam's resonant frequency (f_b) can be approximated using the Euler-Bernoulli theory [106],

$$f_b = 1.027 \frac{W_b}{L_b^2} \sqrt{\frac{E}{\rho}}. \tag{6.5}$$

Equation (6.5) is an estimate for f_b without taking into consideration of the stresses the beam experiences due to the length-extensional vibration mode. The calculated value for f_b according to equation (6.5) is 435.3kHz. Since the two ends of the middle beam is loosely clamped, measured frequency of the beam while squares are vibrating simultaneously is expected to be less than the calculated f_b value. ANSYS-simulated resonant frequency for the Clamped-Clamped beam mode of Figure 6.4(a) and the two squares in Lamé-mode of Figure 6.4(b) are 430kHz and 5.939MHz, respectively.

In Lamé mode, the squares can be driven differentially at the sides indicated by V_d+ and V_d– in Figure 6.3. When the two square resonators are simultaneously vibrating in-sync, the middle beam will experience longitudinal stresses along its length. If the beam had been designed to join the two squares at their corners instead of at the middle, another mode with the squares in out-of-sync vibration would show up. Symmetry along both axes of the 2-D plane for the composite design shown in Figure 6.4 is important for suppressing the unwanted vibration modes while having minimal energy losses.

6.4 Proposed temperature compensation method

The beat frequency method of mixing signals from two oscillators was initially used for quartz crystal "dual-mode oscillators" as a mean to measure the temperature [116, 117]. The frequencies of two harmonic modes of the quartz crystal are mixed to give a beat frequency that is linearly dependent with temperature. This linear dependence with temperature enables compensation with external electronics more efficiently. Figure 6.5 shows a schematic of beat frequency method for the case of our composite resonator with two independent oscillation setups. The product of the mixer is subsequently filtered with a band-pass filter. Then, the beat frequency (f_{beat}) is derived as

$$f_{beat} = f_s - Nf_b \,. \tag{6.6}$$

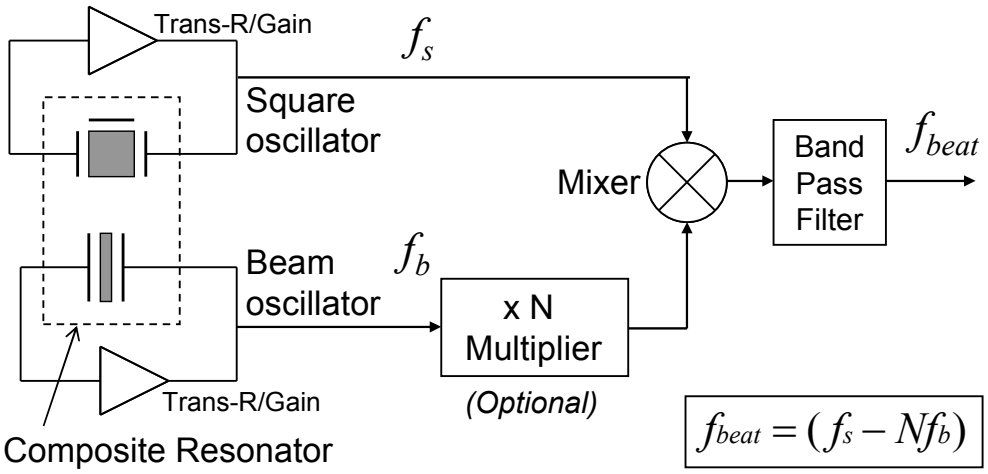

Figure 6.5: Schematic diagram for frequency mixing of the square and beam oscillators to generate the beat frequency.

Since the resonant frequency of a resonator depends on the geometry, the designer must set the initial frequencies of the device. If the frequencies of the two oscillators are designed to be close to each other and the devices have different TC_f values, then the mixed product f_{beat} is much smaller frequency and also becomes more

sensitive to temperature changes. Then, the system can be used as a temperature sensor [119, 18]. In this case, the ×N multiplier block shown in Figure 6.5 is not required.

However, if the oscillation frequencies are farther apart, f_{beat} itself could be used as the reference frequency for the oscillator. The expression for f_{beat} using the ×N multiplier can be further derived, using only the first-order temperature coefficients as

$$f_{beat} = (f_s - Nf_b) = (f_{so} - Nf_{bo}) + (\alpha_s f_s - N\alpha_b f_b)\Delta T\,, \tag{6.7}$$

where f_{so} and f_{bo} are initial frequencies at room temperature, and α_s and α_b are TC_f values of square and beam resonators, respectively. Since the temperature coefficient of f_{beat} is desired to be as low as possible, the objective is to set the following condition,

$$\alpha_s f_s = N\alpha_b f_b \tag{6.8}$$

from equation (6.7), so that the magnitude of TC_f for the f_{beat} is very low. Initially, the TC_f values α_s and α_b are unknown. Once the TC_f values are obtained from initial measurements, appropriate value for N can be calculated to satisfy the equation (6.8). However, some arbitrary value for N may not be attainable in a practical multiplier circuit. Therefore, a better approach would be to make adjustments in resonant frequency by re-designing the resonator through modifications in device geometry.

6.5 Measurement setup and implementation

At first, the composite resonator is characterized for its open-loop response, with the square resonators differentially driven and tested for the Lamé-mode frequency, while the beam resonator is independently tested with a two-port network setup. A dc-bias voltage V_P is applied directly to the resonator proof-mass. In order to verify the

temperature compensation concept presented in this chapter, two independent oscillation circuits are implemented around the composite structure. The overall circuit schematic is shown in Figure 6.6 for both oscillation loops. There are two basic requirements in order to start up the oscillation: a) the gain of the positive feedback in series connection must be higher than one and b) the total phase shift through the loop must be zero degree. Both of the requirements must be met at the same time to achieve sustained oscillation.

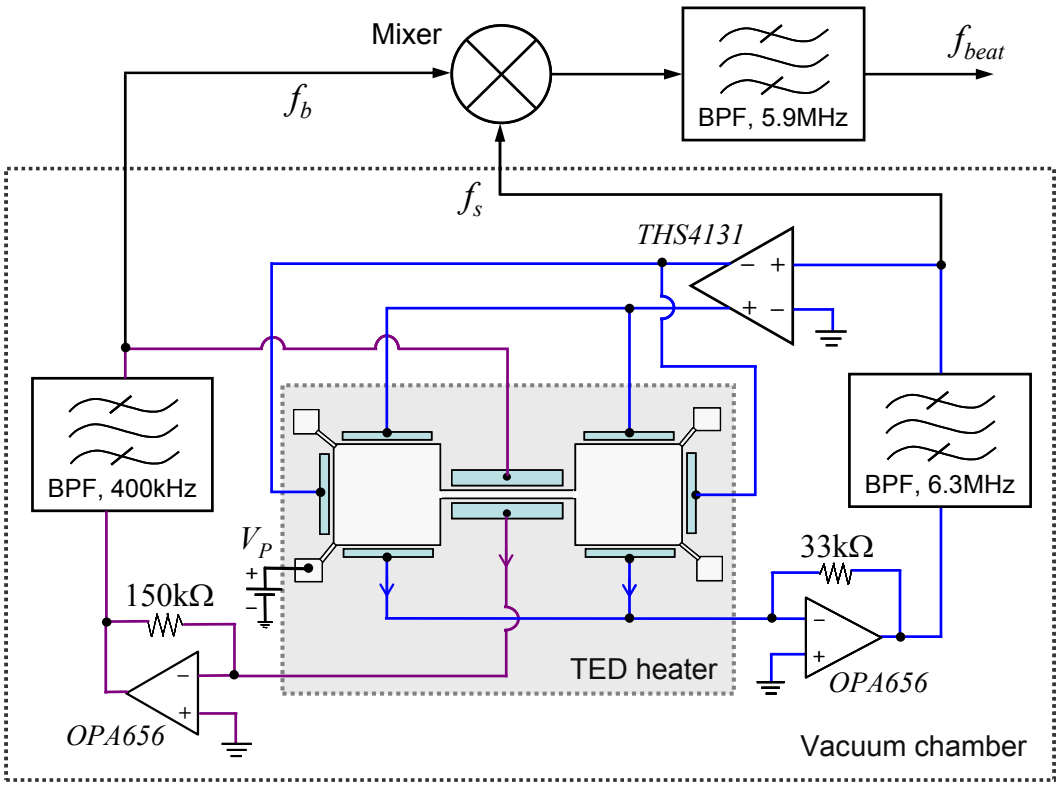

Figure 6.6: Circuit schematic for implementing square and beam oscillators from one composite structure, along with frequency mixing to generate temperature-compensated oscillating signal.

The oscillation amplitude is either limited by the closed-loop circuit or the nonlinearities of the micromechanical resonator. The individual closed-loop setup for the beam and square oscillators are shown in Figure 6.7. A closed-loop for two-port setup of the middle beam is realized with transresistance amplifier and band-pass filter in series connection as shown in Figure 6.7(a). For simplicity, no extra amplitude-level

control circuitry was added in the feedback loops so the oscillation was limited by the nonlinearity of the beam resonator. Including an automatic amplitude-level control circuit would actually improve the overall oscillation with the beam resonator in linear vibration, providing lower phase noise [21].

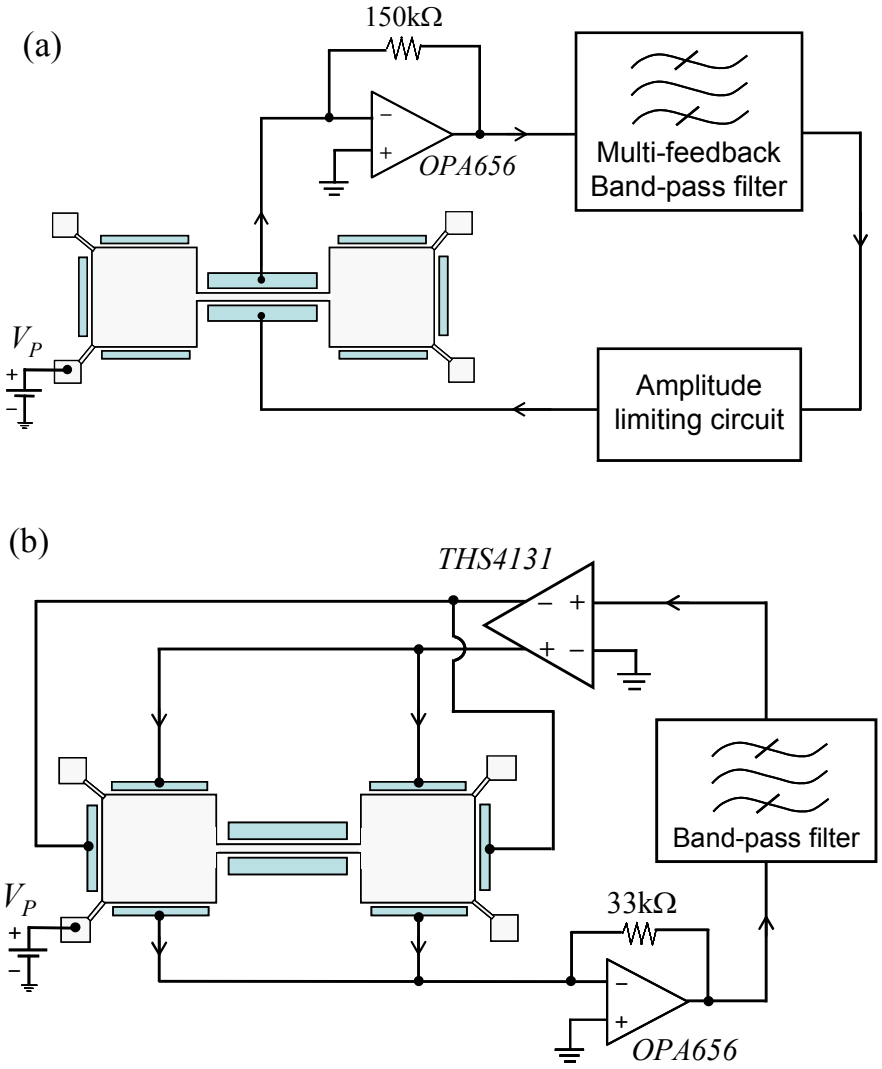

Figure 6.7: Schematic diagrams of closed-loop feedback circuits for (a) beam oscillator and (b) square oscillator.

In Figure 6.7(b), two square resonators are placed in a positive feedback loop with transresistance amplifier, band-pass filter and single-to-differential conversion amplifier setup. The positive and negative drive signals from single-to-differential

circuit block are connected to the corresponding adjacent electrodes of square resonators. Output current from sense electrodes is sent to a transresistance amplifier with 33kΩ feedback resistance. Once the oscillation requirements are met and the amplifiers are given proper power supplies, bias voltage V_P is increased to a certain DC value when both squares and beam are in sustained oscillation. Even without amplitude-level control or gain limiting circuit, Lamé-mode square resonators can still oscillate with undistorted sinusoidal output with low phase noise [104]. However, the time-domain oscillation output of the middle beam is distorted due to nonlinear vibrations, and hence amplitude-level control is necessary for the beam to achieve low phase noise.

For temperature measurements, the composite resonator is heated with a Thermoelectric device (TED) placed underneath the resonator die. A schematic of TED setup is shown in Figure 6.8, with a DC source supplying current to TED, and a 51Ω power resistor is used to limit the amount of current that also serves as a heat sink.

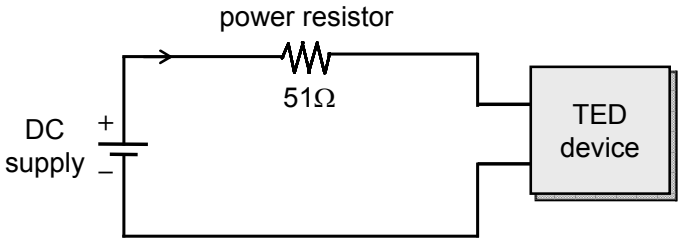

Figure 6.8: Schematic of setup for thermoelectric device used to heat the composite resonator.

Accurate temperature readings are obtained by probing the die itself with wires from thermocouple module, and readings are taken from a multimeter. Double balanced mixer model TUF-3LH+ from Mini-Circuits is used as the frequency mixer. The difference-frequency output of the mixer is filtered by a narrow band-pass filter with high enough quality factor so that the sum-frequency output is suppressed. The pressure of vacuum chamber is maintained at about 36μTorr (0.005 Pa).

6.6 Experimental results and discussion

Measurement results for open-loop characterization of the composite resonator and verification of our temperature compensation method with close-loop oscillation setup will be presented in this section.

6.6.1 Open-loop characterization of the device

Initially, the composite device is tested for the resonant frequency of beam and square resonators in open-loop. The two square resonators are driven simultaneously and at room temperature measured resonant frequency f_s is 6.347MHz with Q of about 1.3million, driven with AC of 0.42Vpp and V_P is biased at 60V. When the beam is tested while squares are "off" and not excited, its clamped-clamped resonance is 402.6kHz with Q of 4,392, driven at the same conditions as that of the square resonators.

When the square resonators are driven to be highly nonlinear with AC levels above 5Vpp, S_{21} response of the beam shows that it is still vibrating in normal resonance without nonlinearities. Even though the beam is experiencing length-extensional excitations from the two squares at both clamped ends, the lateral vibrations of the beam is not affected significantly. Vice versa, the resonance plot of square resonators is not affected by highly nonlinear beam vibrations.

Resonant frequency vs. V_P plots for the beam and square resonators are shown in Figure 6.9. The electrostatic spring softening has much larger effect on the beam resonator than that it has on the square resonators. Resonant frequency shift for the square resonators is only 6Hz, whereas the shift is 2584Hz for the beam resonator over the same V_P range. This low sensitivity of the square resonators is due to high

mechanical stiffness of bulk acoustic mode. Mechanical spring constant (k_m) extracted from Figure 6.9 is 1.04×10^8 N/m for the square resonators that is much higher than 1.67×10^4N/m for the beam resonator.

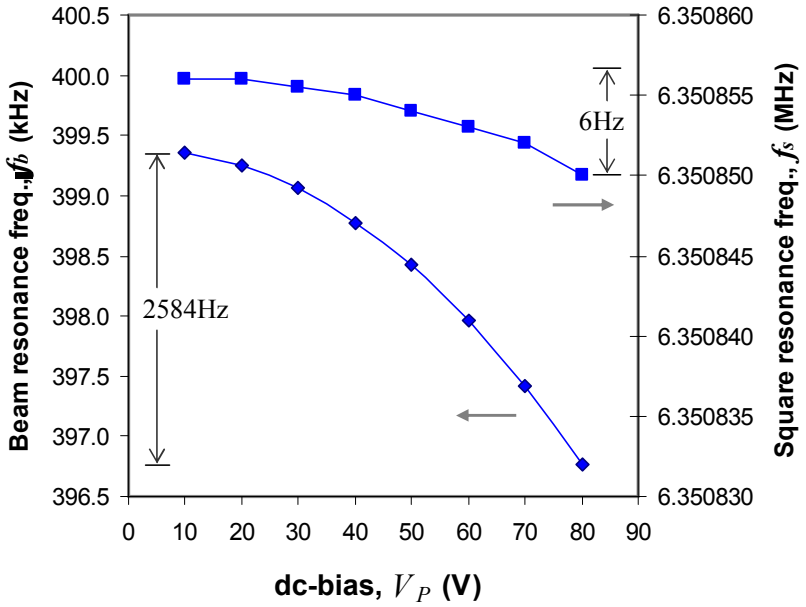

Figure 6.9: Resonant frequency shift of square resonators and beam resonator of the composite device due to electrostatic spring softening with increasing dc-bias V_P.

6.6.2 Verification of temperature compensation concept

The system-level verification of the proposed compensation method with two independent feedback loops was realized for the beam oscillator and square oscillator. Time-domain oscillations along with the corresponding frequency spectrums are recorded with Tektronix's TDS5034B digital oscilloscope. Both oscillation frequencies decreased as expected as the temperature is increased from 29°C to 70°C at fixed V_P of 90V. Each of the frequency values in Table 6.1 for f_b, f_s and f_{beat} is obtained from peak of frequency spectrum given by oscilloscope for corresponding time-domain response.

Table 6.1: Measured frequency of oscillation for the beam and square oscillators, as well as the final oscillation f_{beat} over the measured temperature range at fixed V_P of 90V.

Temperature (°C)	Beam, f_b (kHz)	Square, f_s (MHz)	f_{beat} (MHz)
29	394.32	6.3503	5.9559
31	394.28	6.3497	5.9556
33	394.02	6.3492	5.9552
36	393.50	6.3484	5.9550
39	392.88	6.3478	5.9549
43	392.12	6.3470	5.9548
46	391.52	6.3461	5.9546
51	390.86	6.3450	5.9542
54	390.52	6.3440	5.9537
60	389.69	6.3428	5.9533
70	387.60	6.3409	5.9531

Taking the frequency at 29°C as the reference, changes in frequency with temperature ($\Delta f / f_o$) are extracted from the measured data as shown in Figure 6.10. Hence, the temperature coefficient TC_f value α_s of the square oscillator is –36.8ppm/°C and α_b of the beam oscillator is –418.3ppm/°C. Both resonant frequencies, f_s and f_b, are linearly dependent on temperature over the tested temperature range. In order to satisfy the condition in equation (6.8), $\alpha_s f_s = N\alpha_b f_b$, the value of multiplier N should be around 1.42. Since multiplier circuit is usually implemented based on integer multiples of resonant frequency, the exact requirement of N=1.42 may not be attainable with a real circuit. A better approach is to re-design the device so that new frequencies of the two oscillators satisfy the equation (6.8) with N = 1 and the multiplier is no longer required. The results presented here are based on initial resonator design.

Once the oscillating signals are sent to mixer, it produces difference-frequency and sum-frequency outputs. At this point, sinusoidal difference-frequency signals around 5.95MHz are filtered using narrow band-pass filter to suppress the sum-frequency signal and other harmonics. Figure 6.11 shows a time-domain oscillation f_{beat}

of 5.955MHz at 36°C with ~213mV of amplitude. Figure 6.11 also shows the frequency spectrum of f_{beat} at 36°C, and similar responses are observed at other temperatures.

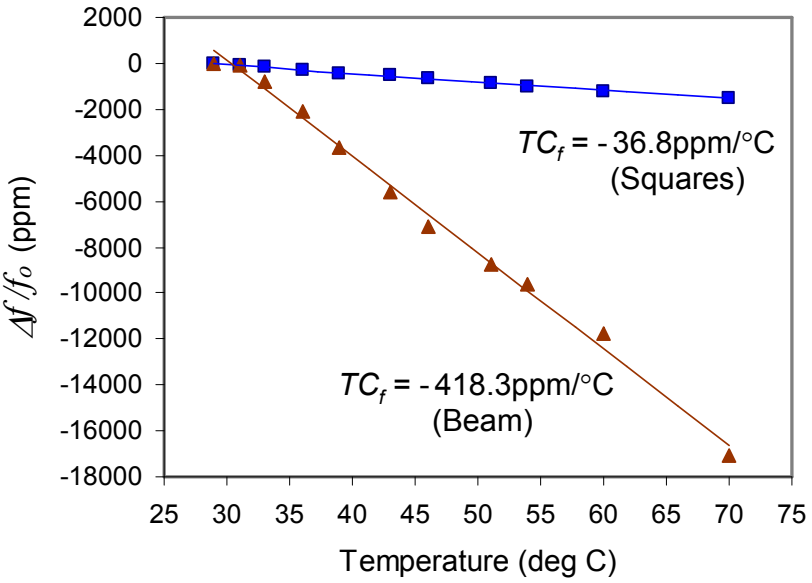

Figure 6.10: Measured temperature coefficients of square oscillator (–36.8ppm/°C) and the middle beam oscillator (–418.3ppm/°C), while both oscillators are operating simultaneously.

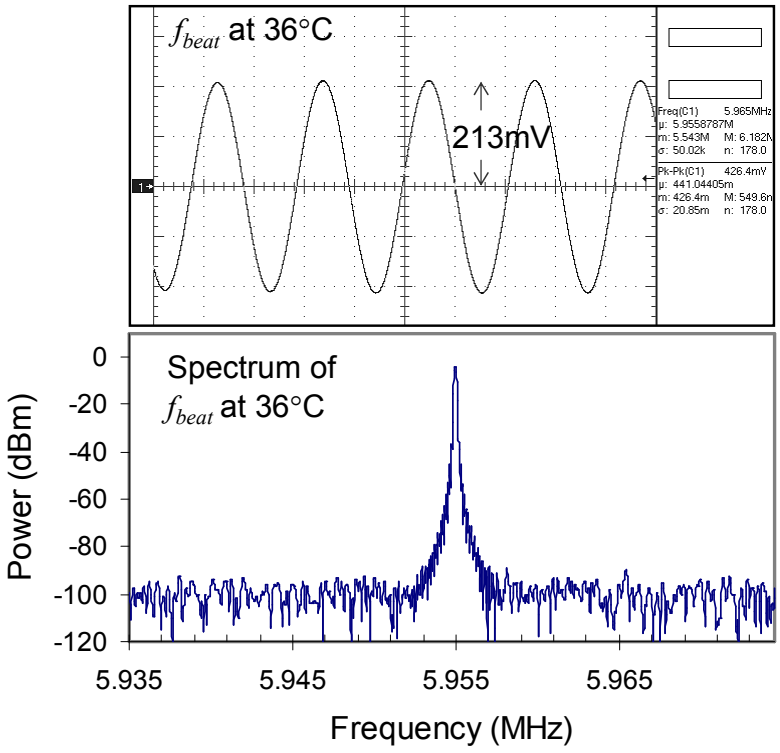

Figure 6.11: Time-domain oscillation and the corresponding frequency spectrum of f_{beat} at 36°C.

Figure 6.12 shows a plot of fractional changes in f_{beat} with respect to the f_{beat} value at 29°C and the temperature coefficient for f_{beat} is about –11.5ppm/°C.

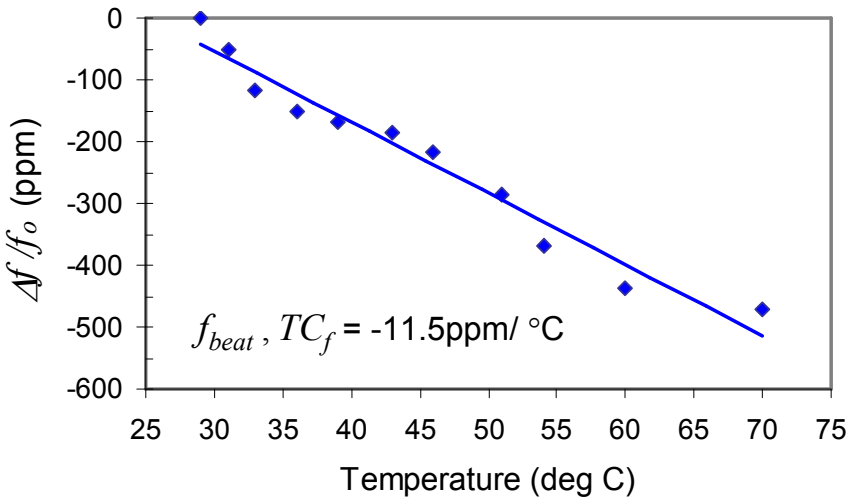

Figure 6.12: Frequency changes in f_{beat} with temperature and the TC_f is about –11.5ppm/°C.

Clamped-Clamped beam resonators in SOIMUMPs process have been measured to have large temperature coefficients of about –80ppm/°C to –90ppm/°C [107]. Hence, observed larger negative TC_f of our middle beam oscillator is likely due to the longitudinal stresses the beam experiences from length-extensional vibrations.

The compensation demonstrated with our unique composite resonator design is just one of the possibilities. This method can be extended to two oscillating signals from any other types of resonators. For example, two bulk-mode resonators having different TC_f values could also be used to implement the compensation. Bulk-mode resonators have been known to have very high Q with stable oscillation. Therefore, the beat frequency after mixing two bulk-mode oscillators should be even more stable than that obtained from mixing flexural beam and bulk-mode square oscillators. The two resonators could also be physically attached at the anchor support rather than at moving mechanical parts to further reduce interference from each other.

6.6.3 Benefits and drawbacks of our method

Although the presented method is a viable compensation approach, it comes with benefits and drawbacks. The main advantage of this method is that it requires no external temperature sensor. If the two resonators are designed properly there is actually no need for complex digital temperature compensation electronics that would otherwise consume more power. Low TC_f values in several parts per million could already be achieved with our compensation method. Therefore, combination of external digital compensation electronics with our method could yield even better results with TC_f values in parts per billion.

However, our method requires two independent oscillator setups instead of one. The design of the composite structure is more complex than an oscillator based on just one resonator. It requires a good frequency mixer and high quality band-pass filter such that their contributions to phase noise are minimal. The Q values of the beam and square resonators do not degrade over the entire tested temperature range; however, the degradation of Q is uncertain after the two oscillations go through the mixer. Ideally, the mixer should produce only a scaled version of the product of the two input signals. Nevertheless in reality, mixers will add spurious signals and random noise to the desired beat frequency signal. The TC_f values of the two resonators are unknown at first so the device must be re-designed to adjust the resonant frequencies of the beam and square resonators after initial test results. Such further improvements could provide even better TC_f value for the reference oscillation.

6.7 Summary

Silicon micromechanical resonators have negative TC_f value that is mainly dependent on material softening due to changes in Young's modulus with temperature. Hence, a temperature compensation method is needed for resonator oscillators. A new method of compensation for micromechanical oscillators has been presented in this chapter. One of the two oscillations comes from two Lamé-mode square resonators in one positive feedback loop, and the other oscillation comes from a beam resonator bridging the two square resonators in another closed-loop. Our compensation method makes use of the high temperature sensitivity of flexural beam resonator under longitudinal stress, along with the bulk-mode square resonators that can provide more stable frequency response.

Temperature coefficient of the square oscillator is –36.8ppm/°C, and that of the beam oscillator is –418.3ppm/°C, the TC_f of final beat frequency is –11.5ppm/°C. Resonant frequency and TC_f value are the key parameters for our compensation method. Therefore, device geometry should be appropriately redesigned after the initial measurement results such that TC_f values could be in several ppm/°C. For the 2μm gap, the resonant frequency tuning with V_P is quite good for the beam resonator although it is less effective for the bulk-mode resonators. Therefore, combining our method with another compensation technique such as tuning the V_P bias could further improve the TC_f of reference oscillation. Our method can also be extended to two oscillating signals from other types of resonators, such as two bulk-mode resonators having different TC_f values. Bulk-mode resonators have been shown in earlier chapters to provide very high quality factor. Therefore, the beat frequency after mixing two independent bulk-mode oscillators could provide stable oscillation with low TC_f value.

Chapter 7

Conclusion and Future Works

This thesis presented the performance of flexural-mode resonators and bulk-mode resonators with regard to following parameters: quality factor, pressure stability, power handling, nonlinearity and temperature stability. A method of temperature compensation is essential for reference oscillator applications based on silicon micromechanical resonators. One attempt for temperature compensation is presented in this work that utilizes both flexural beam resonator and bulk-mode square resonators as part of one composite resonator. The proposed compensation method has high potential to complement the existing compensation methods reported in literature. The devices reported in this thesis have been fabricated using a commercial foundry process (SOIMUMPs); however their performance can be generalized to other processes, and not limited by a special application specific MEMS process.

7.1 Conclusion

Different types of resonator designs: Clamped-Clamped beam, fundamental-mode and second-mode Free-Free beams, length-extensional rectangular resonators, Lamé-mode square resonators, and wine-glass mode disk resonators have been presented in this

thesis. Various electrical characterization techniques presented in Chapter 2 have been used to enhance the signal-to-noise ration (SNR) of the frequency response as well as suppress the effect of parasitic feedthrough capacitances.

Based on the comparison of quality factor parameter for various resonators in Chapter 3, the bulk-mode resonators can provide Q on the order of $\sim 10^6$ and the Q of flexural beam resonators are only in thousands range. High mechanical spring constant of bulk-mode resonators is roughly four orders of magnitude above that of flexural beam resonators. The drawback of high stiffness is that dc-bias V_P tuning for bulk-mode resonators becomes more difficult compared to beam resonators since the electrostatic spring softening effect must overcome much larger mechanical stiffness.

The structural geometry of Lamé-mode square resonators, such as the number of anchors, structural layer thickness and release etch holes all contribute to the quality factor. Anchor losses have been found to be the dominant loss mechanism affecting the Q of bulk-mode resonators. The T-shaped anchor designs for bulk-mode square and rectangular resonators can provide higher Q with minimal energy losses. However, anchor geometry needs to be carefully designed, since long flexible anchors are tested to lower the power handling of square resonators.

As presented in Chapter 4, the Q will inevitably come down as the surrounding pressure is increased due to squeeze-film/air damping. The resonant frequency of resonator has been tested to shift with pressure changes depending on the type of damping force. However, changes in Q with pressure are much more significant for capacitive resonators of this work. Bulk-mode resonators with much higher mechanical stiffness outperform the beam resonators, and able to maintain the maximum quality factor under high pressure levels.

The performance of a resonator depends on whether it is operating in linear or nonlinear region. A brief summary of mechanical nonlinearity and electrical nonlinearity has been presented in Chapter 5. The results show that nonlinearities not only destabilize the resonant frequency, but also limit the vibration energy storage and hence place a limitation on the power handling capability of the resonator. The wine glass disk resonator with slightly higher mechanical stiffness than the Lamé-mode resonator is observed to have somewhat better power handling. The Lamé-mode square and disk resonators are less susceptible to nonlinear effects, that is, they can store orders of magnitude larger vibration energy, and thus can handle much more power than the flexural resonators. Better power handling along with ultra-high quality factor of bulk-mode resonators could provide superior phase noise performance in oscillators.

The variation in frequency with temperature is unavoidable for silicon micromechanical resonators. Therefore, a method of compensation is necessary for oscillators. In Chapter 6, we propose an idea for temperature compensation based on difference-frequency mixing of flexural beam oscillator and bulk-mode square oscillator. Our compensation method makes use of high temperature sensitivity of flexural beam resonator under longitudinal stresses along with the stable oscillation provided by bulk-mode square resonators.

7.2 Future directions for MEMS resonators

In today's MEMS technology large demand is placed on miniaturization of high-performance devices, with the potential for CMOS integration and low-cost batch fabrication. The studies on performance parameters presented in this thesis show that bulk-mode resonators can provide high Q under high pressure levels and are able to handle large input power. Main application areas for bulk-mode micromechanical resonators are mass sensors, RF switches, filters, and reference oscillators.

The acquired signal should be enhanced with good transduction mechanism such as improved negative-capacitive feedthrough cancellation as outlined in Section 2.3.4 or piezoresistive detection method [121-123]. The piezoresistive sensing works by letting a current through the resonator mass and detecting the variation in the resistance of the vibrating resonator due to piezoresistive effect. The piezoresistive sensing rejects the feedthrough currents fairly well, improves the SNR of motional signal, and eliminates the need for large DC bias voltage. But the main drawback is that it needs a constant DC current passing through the resonator, which increases the overall power consumption. Another approach to completely avoid the DC bias is to use piezoelectric transduction mechanism while at the same time utilize the low-acoustic-loss property of single-crystal silicon SOI substrate.

Several reports on bulk-mode mass sensors have shown that resonator with ultra-high Q are very useful and highly sensitive for mass sensing application [12-14]. Using bulk-mode resonator as mass sensing platform provides larger capture area to a given mass density, with enhanced electrical interface [14]. Therefore, highly sensitive mass sensors could be realized with electrostatic or even piezoelectric bulk-mode resonators.

A recently reported micromechanical RF switch, termed “resoswitch”, is based on the bulk-mode wine glass disk resonator [124, 125], which harnesses the resonance and nonlinear dynamical properties of micromechanical resonators. This device is driven at 2.5V amplitude AC voltage at its 61-MHz resonant frequency that corresponds to a switching period of 16ns with an effective rise time of < 4ns, which is more than 200 times faster than the μs-range switching speeds of the fastest conventional RF MEMS switches [124]. The operation of resonant switches is analogous to that of a traditional transistor. Therefore, further studies on bulk-mode resonant switches could provide very useful results in power amplifier and power converter applications.

Since quality factor is very high, filters based on bulk-mode resonator can be very challenging. With innovative and improved coupling mechanisms, bulk-mode filters could provide very narrow bandwidth and ultra-low power consumption. Given an array of filters can be fabricated in small size and easy integration with CMOS, piezoelectric bulk-mode RF filters would be very useful in wireless communications.

The bulk-mode resonators are very suitable for reference oscillator applications because the combined effect of ultra-high Q and superior power handling could provide very low phase noise even without an amplitude-level control circuit. The follow-up work on oscillator [126], based on the Lamé-mode resonators of this thesis, achieved low phase noise of -132dBc/Hz @1kHz away from carrier that meets the GSM requirement while the resonator is operating in nonlinear region. The oscillation frequency of bulk-mode oscillator can be pushed to high value mainly due to their high mechanical stiffness. Moreover, bulk-mode resonators could also operate in air with Q in thousands range.

References

[1] F. Watanabe and T. Watanabe, "Convex quartz crystal resonator of extremely high Q in 10MHz-50MHz," *Proc. of IEEE Ultrasonics Symposium*, vol. 1, 2002, pp. 1007-1010.

[2] M. Palaniapan and L. Khine, "Micromechanical resonator with ultra-high quality factor," *Electronics Letters*, vol. 43, no. 20, 2007, pp. 1090-1092.

[3] J. E.-Y. Lee and A. A. Seshia, "Square wine glass mode resonator with quality factor of 4 million," *IEEE Sensors Conf.*, Oct. 26-29, 2008.

[4] T. A. Roessig, R. T. Howe, A. P. Pisano and J. H. Smith, "Surface-micromachined resonant accelerometer," *Inter. Conf. on Solid States Sensors and Actuators*, (*Transducers'97*), vol. 2, 1997, pp. 859-862.

[5] A. A. Seshia, M. Palaniapan, T. A. Roessig, R. T. Howe, R. W. Gooch, T. R. Schimert and S. Montague, "A vacuum packaged surface micromachined resonant accelerometer," *J. of Microelectromechanical Systems*, vol. 11, no. 6, 2002, pp. 784-793.

[6] L. He, Y. P. Xu and M. Palaniapan, "A CMOS readout circuit for SOI resonant accelerometer with 4-μg bias stability and 20-μg/$\sqrt{Hz}$ resolution," *IEEE J. of Solid-State Circuits*, vol. 43, no. 6, 2008, pp. 1480-1490.

[7] F. Ayazi and K. Najafi, "Design and fabrication of a high-performance polysilicon vibrating ring gyroscope," *Proc. of Inter. Workshop on Micro Electro Mechanical Systems*, Jan. 25-29, 1998, pp. 621-626.

[8] N. Yazdi, F. Ayazi, and K. Najafi, "Micromachined inertial sensors," *Proceedings of the IEEE*, vol. 86, no. 8, Aug. 1998, pp. 1640-1659.

[9] M. Palaniapan, R. T. Howe and J. Yasaitis, "Performance comparison of integrated z-axis frame microgyroscopes," *Inter. Conf. on Micro Electro Mechanical Systems*, Jan. 19-23, 2003, pp. 482-485.

[10] A. S. Phani, A. A. Seshia, M. Palaniapan, R. T. Howe and J. A. Yasaitis, "Modal coupling in micromechanical vibratory rate gyroscopes," *IEEE Sensors Journal*, vol. 6, no. 5, 2006, pp. 1144-1152.

[11] M. F. Zaman, A. Sharma, Z. Hao and F. Ayazi, "A mode-matched Silicon-Yaw tuning-fork gyroscope with subdegree-per-hour Allan deviation bias instability," *J. of Microelectromechanical Systems*, vol. 17, no. 6, 2008, pp. 1526-1536.

[12] Hao Zhang and Eun Sok Kim, "Micromachined acoustic resonant mass sensor," *J. of Microelectromechanical Systems*, vol. 14, no. 4, 2005, pp. 699-706.

[13] R. Abdolvand, Z. Hao and F. Ayazi, "Temperature-compensated ZnO-on-Diamond resonant mass sensor," *IEEE Sensors Conf.*, Oct. 22-25, 2006, pp. 1297-1300.

[14] J. E.-Y. Lee, B. Bahreyni and A. A. Seshia, "Thin film monitoring with silicon bulk acoustic resonators," *IEEE Sensors Conf.*, Oct. 26-29, 2008, pp. 581-584.

[15] B. Ilic, D. Czaplewski, M. Zalalutdinov, H. G. Craighead, P. Neuzil, C. Campagnolo and C. Batt, "Single cell detection with micromechanical oscillators," *J. of Vacuum Science and Technology B*, vol. 19, no. 6, 2001, pp. 2825-2828.

[16] T. P. Burg, A. R. Mirza, N. Milovic, C. H. Tsau, G. A. Popescu, J. S. Foster and S. R. Manalis, "Vacuum-packaged suspended microchannel resonant mass sensor for biomolecular detection," *J. of Microelectromechanical Systems*, vol. 15, no. 6, 2006, pp. 1466-1476.

[17] F. M. Battiston, J.-P. Ramseyer, H. P. Lang, M. K. Baller, Ch. Gerber, J. K. Gimzewski, E. Meyer and H.-J. Güntherodt, "A chemical sensor based on a microfabricated cantilever array with simultaneous resonant-frequency and bending readout," *Sensors and Actuators B: Chemical*, vol. 77, 2001, pp. 122-131.

[18] C. M. Jha, G. Bahl, R. Melamud, S. A. Chandorkar, M. A. Hopcroft, B. Kim, M. Agarwal, J. Salvia, H. Mehta and T. W. Kenny, "CMOS-compatible dual-resonator MEMS temperature sensor with milli-degree accuracy," *Inter. Conf. on Solid-State Sensors, Actuators and Microsystems* (*Transducers'07*), 2007, pp. 229-232.

[19] Y.-W. Lin, S. Lee, S.-S. Li, Y. Xie, Z. Ren and C. T.-C. Nguyen, "Series-resonant VHF micromechanical resonator reference oscillators," *IEEE J. of Solid-State Circuits*, vol. 39, no. 12, 2004, pp. 2477-2491.

[20] V. Kaajakari, T. Mattila, A. Oja, J. Kiihamäki and H. Seppä, "Square-extensional mode single-crystal silicon micromechanical resonator for low phase noise oscillator applications," *IEEE Elect. Device Lett.*, vol. 25, no. 4, 2004, pp. 173-175.

[21] S. Lee and C. T.-C. Nguyen, "Influence of automatic level control on micromechanical resonator oscillator phase noise," *Proc. of IEEE Inter. Frequency Control Symp.*, 2003, pp. 341-349.

[22] R. Aigner, S. Marksteiner, L. Elbrecht and W. Nessler, "RF-filters in mobile phone applications," *Inter. Conf. on Solid-State Sensors, Actuators, and Microsystems* (*Transducers'03*), 2003, pp. 891-894.

[23] C. T.-C. Nguyen, "Vibrating RF MEMS for next generation wireless applications," *IEEE Custom Integrated Circuits Conf.*, 2004, pp. 257-264.

[24] H. Baltes, et al., *Enabling Technology for MEMS and Nanodevices*, Wiley-VCH, Weinheim, 2004, pp. 178-192.

[25] G. Zhou and P. Dowd, "A method to include micromechanical components into the system level simulation," *Sensors and Actuators A: Physical*, 2002, vol. 97-98, pp. 386-397.

[26] C. Mandelbaum, S. Cases, D. Bensaude, L. Basteres and P. Nachtergaele, "Behavioral modeling and simulation of micromechanical resonator for communications applications," *DTIP of MEMS/MOEMS*, 2003, pp. 21-26.

[27] S. Lee, M. U. Demirci and C. T.-C. Nguyen, "A 10-MHz micromechanical resonator Pierce reference oscillator for communications," *Inter. Conf. Solid-State Sensors, Actuators, and Microsystems* (*Transducers'01*), 2001, pp. 1094-1097.

[28] L. Khine and M. Palaniapan, "Behavioural modelling and system-level simulation of micromechanical beam resonators," *Journal of Physics: Conference Series 34, International MEMS Conference 2006*, May 9-12, 2006, pp. 1053-1058.

[29] J. R. Clark, W.-T. Hsu, M. A. Abdelmoneum and C. T.-C. Nguyen, "High-Q UHF micromechanical radial-contour mode disk resonators," *J. of Microelectromechanical Systems*, vol. 14, no. 6, 2005, pp. 1298-1310.

[30] J. Wang, J. E. Butler, T. Feygelson and C. T.-C. Nguyen, "1.51-GHz nanocrystalline diamond micromechanical disk resonator with material-mismatched isolating support," *IEEE Int. Conf. Micro-Electro-Mechanical Systems*, 2004, pp. 641-644.

[31] S.-S. Li, Y.-W. Lin, Y. Xie, Z. Ren and C. T.-C. Nguyen, "Micromechanical 'hollow-disk' ring resonator," *IEEE Int. Conf. Micro-Electro-Mechanical Systems*, 2004, pp. 821-824.

[32] T. Mattila, J. Kiihamaki, T. Lamminmaki, O. Jaakkola, P. Rantakari, A. Oja, H. Seppa, H. Kattelus, I. Tittonen, "A 12 MHz Micromechanical Bulk Acoustic Mode Oscillator," *Sensors and Actuators A: Physical*, vol. 101, 2002, pp. 1-9.

[33] H. Majjad, J.-R.Coudevylle, S. Basrour and M. de Labachelerie, "Modeling and characterization of Lamé-mode microresonators realized by UV-LIGA," *Inter. Conf. Solid-State Sensors, Actuators, and Microsystems* (*Transducers'01*), 2001, pp. 300-303.

[34] S. A. Bhave, D. Gao, R. Maboudian and R. T. Howe, "Fully-differential poly-SiC Lamé-mode resonator and checkerboard filter," *IEEE Int. Conf. Micro-Electro-Mechanical Systems*, 2005, pp. 223-226.

[35] Holmgren, K. Kokkonen, V. Kaajakari, A. Oja and J. V. Knuuttila, "Direct optical measurement of the Q values of RF-MEMS resonators," *IEEE Ultrasonics Symposium*, 2005, vol. 4, pp. 2112-2115.

[36] F. D. Bannon, III, J. R. Clark and C. T.-C. Nguyen, "High-Q HF microelectromechanical filters," *IEEE J. of Solid-State Circuits*, vol. 35, no. 4, 2000, pp. 512-526.

[37] W.-T. Hsu, J. R. Clark and C. T.-C. Nguyen, "Q-Optimized Lateral Free-Free Beam Micromechanical Resonators," *Inter. Conf. Solid-State Sensors, Actuators, and Microsystems* (*Transducers'01*), 2001, pp. 1110-1113.

[38] K. Wang, A.-C. Wong and C. T.-C. Nguyen, "VHF Free-Free Beam High-Q Micromechanical Resonators," *J. of Microelectromechanical Systems*, vol.9, no. 3, 2000, pp. 347-360.

[39] M. U. Demirci and C. T.-C. Nguyen, Higher-mode free-free beam micromech-anical resonators, *IEEE Inter. Frequency Control Symp.*, 2003, pp. 810-818.

[40] S. Timoshenko, *Vibration Problems in Engineering*, 4th Edition, New York, Wiley, 1974.

[41] T. Mattila, A. Oja, H. Seppa, O. Jaakkola, J. Kiihamaki, H. Kattelus, M. Koskenvuori, P. Rantakari and I. Tittonen, "Micromechanical bulk acoustic wave resonator," *IEEE Ultrasonics Symposium*, vol. 1, 2002, pp. 945-948.

[42] M. A. Abdelmoneum, M. U. Demirci and C. T.-C. Nguyen, "Stemless wine glass-mode disk micromechanical resonators," *IEEE Inter. Conf. Micro-Electro-Mechanical Systems*, Kyoto, Japan, 2003, pp. 698-701.

[43] M. Onoe, "Contour vibrations of isotropic circular plates," *J. Acoustical Society of America*, vol. 28, no. 6, 1956, pp. 1158-1162.

[44] Z. Hao, S. Pourkamali and F. Ayazi, "VHF single-crystal silicon elliptic bulk-mode capacitive disk resonators – part I: Design and modeling," *J. of Microelectromechanical Systems*, vol. 13, no. 6, 2004, pp. 1043-1053.

[45] K. E. Petersen and C. R. Guarnieri, "Young's modulus measurements of thin films using micromechanics," *J. Applied Physics*, vol. 50, no. 11, 1979, pp. 6761-6766.

[46] D. W. Carr, S. Evoy, L. Sekaric, H. G. Craighead and J. M. Parpia, "Measurement of mechanical resonance and losses in nanometer scale silicon wires," *Applied Physics Letters*, vol.75, no. 7, 1999, pp. 920-922.

[47] W.-K. Wong and M. Palaniapan, "Phonon-mediated characterization of micro-electromechanical resonators," *Applied Physics Letters* 89, 064102, 2006.

[48] C.-L. Wong and W.-K. Wong, "In-plane motion characterization of MEMS resonators using stroboscopic scanning electron microscopy," *Sensors and Actuators A: Physical*, 138, 2007, pp. 167-178.

[49] J. R. Clark, W.-T. Hsu and C. T.-C. Nguyen, "Measurement techniques for capacitively-transduced VHF-to-UHF micromechanical resonators," *Inter. Conf. Solid-State Sensors, Actuators, and Microsystems* (*Transducers'01*), vol.2, 2001, pp. 1118-1121.

[50] A.-C. Wong, D. Hao and C. T.-C. Nguyen, "Micromechanical mixer and filters," *Inter. Electron Devices Meeting* (*IEDM*), Dec. 6-9, 1998, pp. 471-474.

[51] Y. Xie, S.-S. Li, Y.-W. Lin, Z. Ren and C. T.-C. Nguyen, "Spurious mode suppression in UHF micromechanical extensional wine-glass ring resonators," *IEEE Int. Conf. Micro-Electro-Mechanical Systems*, 2005, pp. 219-222.

[52] J. E.-Y. Lee, Y. Zhu and A. A. Seshia, "A bulk acoustic mode single-crystal silicon microresonator with a high-quality factor," *J. of Micromechanics and Micro-engineering*, 18, 2008, 064001, pp. 1-6.

[53] J. E.-Y. Lee and A. A. Seshia, "Enhanced electrical characterization of MEMS resonators using on-chip parasitic feedthrough self-cancellation," *European Conf. on Solid-State Transducers* (*Eurosensors XXII*), Sept. 7-10, 2008, pp. 1349-1352.

[54] A. Cowen, G. Hames, D.Monk, S. Wilcenski and B. Hardy, *SOIMUMPs Design Handbook*, revision 5.0, copyright 2002-2008 published by MEMSCAP Inc.

[55] H. A. C. Tilmans, M. Elwebspoek and J. H. J. Fluitman, "Micro resonant force gauges," *Sensors and Actuators A: Physical*, 30, 1992, pp. 35–53.

[56] T. Koyama, D. S. Bindel, W. He and E. P. Quevy, "Simulation tools for damping in high frequency resonators," *IEEE Sensors Conf.*, 2005, pp. 349-352.

[57] J. E.-Y. Lee and A. A. Seshia, "5.4-MHz single crystal silicon wine glass mode disk resonator with quality factor of 2 million," *Sensors and Actuators A: Physical* (in press).

[58] A. C. Wong, J. R. Clark and C. T.-C. Nguyen, "Anneal-activated, tunable 68 MHz micromechanical filters," *Proc. Inter. Conf. Solid-State Sensors and Actuators*, Sendai, Japan, 1999, pp. 1390-1393.

[59] M. U. Demirci and C. T.-C. Nguyen, "Mechanically corner-coupled square microresonator array for reduced series motional resistance," *J. Microelectromechanical Systems*, vol. 15, no. 6, 2006, pp. 1419-1436.

[60] S. A. Chandorkar, M. Agarwal, R. Melamud, R. N. Candler, K. E. Goodson and Kenny, "Limits of quality factor in bulk-mode micromechanical resonators," *IEEE Inter. Conf. Micro-Electro-Mechanical Systems*, 2008, pp. 74-77.

[61] A. Akhieser, J. Phys. (Moscow, U.S.S.R.), vol. 1, 1939, pp. 277-287.

[62] T. O. Woodruff and H. Ehrenreich, "Absorption of sound in insulators," *Physical Review*, vol. 123, no. 5, 1961, pp. 1553-1559.

[63] W. P. Mason, in *Physical Acoustics*, Volume III B, edited by W. P. Mason and R. N. Thurston, *Chapter 6*, Academic, New York, 1964.

[64] S. D. Lambade, G.G. Sahasrabudhe and S. Rajagopalan, "Temperature dependence of acoustic attenuation in silicon," *Physical Review B*, vol. 51, no. 22, 1995, pp. 861-866.

[65] S. Pourkamali, Z. Hao and F. Ayazi, "VHF single crystal silicon capacitive elliptic bulk-mode disk resonators – Part II: Implementation and characterization," *J. of Microelectro-mechanical Systems*, vol. 13, no. 6, 2004, pp.1054-1062.

[66] K. Sundaresan, G. K. Ho, S. Pourkamali and F. Ayazi, "A low phase noise 100MHz silicon BAW reference oscillator," *IEEE Custom Integ. Circuits Conf.*, 2006, pp. 841-844.

[67] L. Khine, M. Palaniapan, and W.K. Wong, "12.9MHz Lamé-mode differential SOI bulk resonators," *Inter. Conf. on Solid-State Sensors, Actuators and Microsystems* (*Transducers'07*), June 10-14, 2007, pp. 1753-1756.

[68] L. Khine and M. Palaniapan, "High-Q bulk-mode SOI square resonators with straight-beam anchors," *J. of Micromechanics and Microengineering*, vol. 19, no. 1, Jan. 2009, p 015017.

[69] Z. Hao and F. Ayazi, "Support loss in micromechanical disk resonators," *IEEE Inter. Conf. Micro-Electro-Mechanical Systems*, 2005, pp. 137-141.

[70] B. Kim, C. M. Jha, T. White, R. N. Candler, M. Hopcroft, M. Agarwal, K. K. Park, R. Melamud, S. Chandorkar and T. W. Kenny, "Temperature dependence of quality factor in MEMS resonators," *IEEE Inter. Conf. Micro-Electro-Mechanical Systems*, 2006, pp. 590-593.

[71] A. Duwel, R. N. Candler, T. W. Kenny and M. Varghese, "Engineering MEMS resonators with low thermoelastic damping," *J. Microelectromechanical Systems*, vol. 15, no. 6, 2006, pp. 1437-1445.

[72] B. A. Auld, *Acoustic Fields and Waves in Solids*, Volume I, copyright by John Wiley & Sons, Inc., 1973.

[73] J. J. Wortman and R. A. Evans, "Young's modulus, shear modulus, and Poisson's ratio in silicon and germanium," *J. of Applied Physics*, vol. 36, no. 1, 1965, pp. 153-156.

[74] W. A. Brantley, "Calculated elastic constants for stress problems associated with semiconductor devices," *J. of Applied Physics*, vol. 44, no. 1, 1973, pp. 534-535.

[75] D. N. Joharapurkar, "Temperature variation of silicon's nonlinearity constant and acoustic attenuation," *J. Applied Physics*, vol. 64, no. 4, 1988, pp. 1726-1729.

[76] S. Rajagopalan, D. N. Joharapurkar and P. R. Shende, "Ultrasonic attenuation and nonlinearity constant in silicon in the temperature range 73-293 K," *J. Applied Physics*, vol. 55, no. 1, 1984, pp. 275-277.

[77] S. K. Kor, P. K. Mishra and N. D. Tripathi, "Ultrasonic attenuation in pure and doped n-type silicon," *Physical Review B*, vol. 10, no. 2, 1974, pp. 775-778.

[78] L.C. Shao, M. Palaniapan, L. Khine and W.W. Tan, "Micromechanical resonators with submicron capacitive gaps in 2 μm process," *Electronics Letters*, vol. 43, no. 25, 2007, pp. 1427-1428.

[79] S. Pourkamali, G. K. Ho and F. Ayazi, "Low-impedance VHF and UHF capacitive silicon bulk acoustic wave resonators – Part I: Concept and fabrication," *IEEE Trans. on Electron Devices*, vol. 54. no. 8, 2007, pp. 2017-2023.

[80] V. L. Rabinovich, R. K. Gupta and S. D. Senturia, "The effect of release-etch holes on the electromechanical behavior of MEMS structures," *Inter. Conf. on Solid-State Sensors, Actuators and Microsystems* (*Transducers'97*), 1997, pp.1125-1128.

[81] W. N. Sharpe Jr., R. Vaidyanathan, B. Yuan, G. Bao and R. L. Edwards, "Effect of etch holes on the mechanical properties of polysilicon," *J. of Vacuum Science & Technology B*, vol. 15, no. 5, 1997, pp. 1599-1603.

[82] L. Shao and M. Palaniapan, "Effect of etch holes on quality factor of bulk-mode micromechanical resonators," *Electronics Letters*, vol. 44, no. 15, 2008, pp. 938-940.

[83] L. Khine and M. Palaniapan, "7MHz length-extensional SOI resonators with T-shaped anchors," *Inter. Conf. Solid-State Sensors, Actuators and Microsystems* (*Transducers'09*), June 21-25, 2009.

[84] K. Najafi, "Micropackaging technologies for integrated microsystems: applications to MEMS and MOEMS," *Proc. of the SPIE*, vol. 4979, 2003, pp. 1-19.

[85] S. Pourkamali and F. Ayazi, "Wafer-level encapsulation and sealing of electrostatic HARPSS transducers," *Proc. of the 6th IEEE Sensors Conference*, 2007, pp. 49-52.

[86] B. Kim, R. N. Candler, M. A. Hopcroft, M. Agarwal, W.-T. Park and T. W. Kenny, "Frequency stability of wafer-scale film encapsulated silicon based MEMS resonators," *Sensors and Actuators A: Physical*, vol. 136, no. 1, 2007, pp. 125-131.

[87] T. Veijola, "Quality factor and resonant frequency shift due to air in RF MEMS radial disk resonators," *Inter. Conf. on Solid-State Sensors, Actuators and Microsystems* (*Transducers'07*), 2007, pp. 643-646.

[88] M. Bao and H. Yang, "Squeeze film air damping in MEMS," *Sensors and Actuators A: Physical*, vol. 136, no. 1, 2007, pp. 3-27.

[89] F. R. Blom, S. Bouwstra, M. Elwenspoek and J. H. J. Fluitman, "Dependence of the quality factor of micromachined silicon beam resonators on pressure and geometry," *J. of Vacuum Science & Technology B*, vol. 10, no. 1, 1992, pp. 19-26.

[90] V. Kaajakari, T. Mattila, A. Oja and H. Seppa, "Nonlinear limits for single-crystal silicon microresonators," *J. Microelectromechanical Systems*, vol. 13, no. 5, 2004, pp. 715-724.

[91] L. C. Shao, M. Palaniapan, L. Khine and W.W. Tan, "Nonlinear behavior of Lamé-mode SOI bulk resonator," *IEEE Inter. Frequency Control Symposium*, 2008, pp. 646-650.

[92] D. B. Leeson, "A simple model of feedback oscillator noise spectrum," *Proc. of IEEE*, vol. 54, no. 2, 1966, pp. 329-330.

[93] T. H. Lee, *The Design of CMOS Radio-Frequency Integrated Circuits*, Cambridge, U.K., Cambridge University Press, 1998.

[94] V. Kaajakari, T. Mattila, J. Kiihamaki, H. Kattelus, A. Oja and H. Seppa, "Nonlinearities in single-crystal silicon micromechanical resonators," *Inter. Conf. on Solid-State Sensors, Actuators and Microsystems* (*Transducers'03*), 2003, pp. 1754-1577.

[95] L. D. Landau and E. M. Lifshitz, *Mechanics*, 3rd Ed., Oxford, UK: Butterworth-Heinemann, 1999.

[96] M. Agarwal, K. Park, R. Candler, M. Hopcroft, C. Jha, R. Melamud, B. Kim, B. Murmann and T. W. Kenny, "Non-linearity cancellation in MEMS resonators for improved power-handling," *IEEE Inter. Electron Devices Meeting* (*IEDM*), 2005, pp. 286-289.

[97] M. Agarwal, S. A. Chandorkar, R. N. Candler, B. Kim, M. A. Hopcroft, R. Melamud, C.M. Jha, T. W. Kenny and B. Murmann, "Optimal drive condition for nonlinearity reduction in electrostatic microresonators," *Applied Physics Letters* 89, 214105, 2006.

[98] H. Nayfeh and Dean T. Mook, *Nonlinear Oscillations*, John Wiley & Sons, Inc., Printed in USA, 1979.

[99] L. Shao, "Nonlinear Vibration of Micromechanical Resonators," *Ph.D. Dissertation*, National University of Singapore, Singapore.

[100] M. I. Younis and A. H. Nayfeh, "A study of the nonlinear response of a resonant microbeam to an electric actuation," *Nonlinear Dynamics*, vol. 31, 2003, pp. 91-117.

[101] L. C. Shao, M. Palaniapan and W. W. Tan, "The nonlinearity cancellation phenomenon in micromechanical resonators," *J. of Micromechanics and Microengineering*, vol. 18, 2008, 065014 (9pp).

[102] V. Kaajakari, T. Mattila, A. Lipsanen and A. Oja, "Nonlinear mechanical effects in silicon longitudinal mode beam resonators," *Sensors and Actuators A: Physical*, vol. 120, no. 1, 2005, pp. 64-70.

[103] T. Niu, M. Palaniapan, L. Khine and L.C. Shao, "MEMS oscillators using bulk-mode resonators," *European Conf. on Solid-State Transducers* (*Eurosensors XXII*), 2008.

[104] L. C. Shao, T. Niu and M. Palaniapan, "Nonlinearities in a high-Q SOI Lamé-mode bulk resonator," *J. of Micromechanics and Microengineering*, vol.19, no.7, 2009, 075002 (8pp).

[105] S. Lee and C. T.-C. Nguyen, "Mechanically-coupled micromechanical arrays for improved phase noise," *IEEE Inter.Ultrasonics, Ferroelectrics, and Freq.Control*, 2004, pp.280-286.

[106] W.-T. Hsu, J. R. Clark and C. T.-C. Nguyen, "Mechanically temperature-compensated flexural-mode micromechanical resonators," *Inter. Elect. Dev. Meeting*, 2000, pp.399-402.

[107] C.L. Wong, L.C. Shao, L. Khine, M. Palaniapan and W.K. Wong, "Novel acoustic phonon detection technique to determine temperature coefficient of frequency in MEMS resonators," *European Conf. on Solid-State Transducers* (*Eurosensors XXII*), 2008.

[108] M. Hopcroft, R. Melamud, R. N. Candler, W.-T. Park, B. Kim, G. Yama, A. Partridge, M. Lutz and T. W. Kenny, "Active temperature compensation for micromachined resonators," *Solid-State Sensor, Actuator and Microsystems Workshop*, 2004, pp. 364-367.

[109] R. Bechmann, "Frequency-temperature-angle characteristics of AT-type resonators made of natural and synthetic quartz," *Proc. of the IRE*, 1956, pp. 1600-1607.

[110] M. Lutz, A. Partridge, P. Gupta, N. Buchan, E. Klaassen, J. McDonald and K. Petersen, "MEMS oscillators for high volume commercial applications," *Inter. Conf. on Solid-State Sensors, Actuators and Microsystems* (*Transducers'07*), 2007, pp. 49-52.

[111] R. Melamud, B. Kim, M. A. Hopcroft, S. Chandorkar, M. Agarwal, C. M. Jha and T. W. Kenny, "Composite flexural-mode resonator with controllable turnover temperature," *IEEE Inter. Conf. Micro-Electro-Mechanical Systems*, 2007, pp. 199-202.

[112] W.-T. Hsu and C. T.-C. Nguyen, "Stiffness-compensated temperature-insensitive micromechanical resonators," *IEEE Inter. Conf. Micro-Electro-Mechanical Systems*, 2002, pp. 731-734.

[113] W.-T. Hsu, A. R. Brown and K. R. Cioffi, "A programmable MEMS FSK transmitter," *IEEE Inter. Solid-State Circuits Conference*, 2006, pp. 1111-1120.

[114] K. Sundaresan, G. K. Ho, S. Pourkamali and F. Ayazi, "Electronically temperature compensated silicon bulk acoustic resonator reference oscillators," *IEEE J. Solid-State Circuits*, vol. 42, no. 6, 2007, pp. 1425-1434.

[115] M. A. Hopcroft, M. Agarwal, K. K. Park, B. Kim, C. M. Jha, R. N. Candler, G. Yama, B. Murmann and T. W. Kenny, "Temperature compensation of a MEMS resonator using

quality factor as a thermometer," *IEEE Inter. Conf. Micro-Electro-Mechanical Systems*, 2006, pp. 222-225.

[116] S. S. Schodowski, "Resonator self-temperature-sensing using a dual-harmonic-mode crystal oscillator," *Proc. 43rd Sym. on Frequency Control*, 1989, pp. 2-7.

[117] J. R. Vig, "Temperature-insensitive dual-mode resonant sensors–A review," *IEEE Sensors Journal*, vol. 1, no. 1, 2001, pp. 62-68.

[118] E. P. Quévy and R. T. Howe, "Redundant MEMS resonators for precise reference oscillators," *IEEE Radio Frequency Integrated Circuits Symposium*, 2005, pp. 113-116.

[119] M. Koskenvuori, V. Kaajakari, T. Mattila and I. Tittonen, "Temperature measurement and compensation based on two vibrating modes of a bulk acoustic mode microresonator," *IEEE Inter. Conf. Micro-Electro-Mechanical Systems*, 2008, pp. 78-81.

[120] L. Khine, M. Palaniapan, L. C. Shao, C. L. Wong and W.-K. Wong, "Temperature compensation of MEMS oscillator composed of two adjoining square and beam resonators," *European Conf. on Solid-State Transducers* (*Eurosensors XXII*), 2008, pp. 1345-1348.

[121] J. T. M. Van Beek, P. G. Steeneken and B. Giesbers, "A 10MHz piezoresistive MEMS resonator with high Q," *IEEE Inter. Frequency Control Symposium*, 2006, pp. 475-480.

[122] D. Weinstein and S. A. Bhave, "Piezoresistive sensing of a dielectrically actuated silicon bar resonator," *Solid-State Sensors, Actuators, and Microsys.Workshop*, 2008, pp.368-371.

[123] A. T.-H. Lin, J. E.-Y. Lee, J. Yan and A. A. Seshia, "Enhanced transduction methods for electrostatically driven MEMS resonators," *Inter. Conf. on Solid-State Sensors, Actuators and Microsystems* (*Transducers'09*), 2009, pp. 561-564.

[124] Y. Lin, W.-C. Li, Z. Ren and C. T.-C. Nguyen, "A resonance dynamical approach to faster, more reliable micromechanical switches," *IEEE Inter. Frequency Control Symp.*, 2008, pp.640-645.

[125] Y. Lin, *et al*., "The micromechanical resonant switch ("Resoswitch")," *Solid-State Sensor, Actuator, and Microsystems Workshop*, 2008, pp. 40-43.

[126] T. Niu and M. Palaniapan, "A low phase noise 10MHz micromechanical Lamé-mode bulk oscillator operating in nonlinear region," *IEEE Inter. Frequency Control Symp.*, 2010, pp. 189-194.

List of Publications

Journal Papers

1. L. Khine and M. Palaniapan, "Temperature compensation of MEMS oscillator based on frequency mixing of two oscillations," *Journal of Micromechanics and Microengineering*. (In submission process)

2. L. Khine and M. Palaniapan, "Effect of structural thickness, anchor length and number of anchors on performance of micromechanical bulk-mode resonators," *Electronics Letters*, vol. 45, no. 1, Jan. 2009.

3. L. Khine and M. Palaniapan, "High-Q bulk-mode SOI square resonators with straight-beam anchors," *Journal of Micromechanics and Microengineering*, vol. 19, no. 1, Jan. 2009, p 015017.

4. L.C. Shao, M. Palaniapan, W.W. Tan, and L. Khine, "Nonlinearity in micromechanical Free-Free beam resonators: modeling and experimental verification," *Journal of Micromechanics and Microengineering*, vol. 18, no. 2, Feb. 2008, p 025017.

5. L.C. Shao, M. Palaniapan, L. Khine, and W.W. Tan, "Micromechanical resonators with submicron capacitive gaps in 2 μm process," *Electronics Letters*, vol. 43, no. 25, Dec. 2007, pp. 1427-1428.

6. M. Palaniapan and L. Khine, "Micromechanical resonator with ultra-high quality factor," *Electronics Letters*, vol. 43, no. 20, Sept. 2007, pp. 1090-1092.

7. M. Palaniapan and L. Khine, "Nonlinear behavior of SOI Free-Free micromechanical beam resonator," *Sensors & Actuators A: Physical*, vol. 142, no. 1, 2008, pp. 203-210.

Conference Proceedings

1. L. Khine and M. Palaniapan, "7MHz length-extensional SOI resonators with T-shaped anchors," *15th International Conference on Solid-State Sensors, Actuators and Microsystems (Transducers'09)*, Denver, Colorado, USA, June 21-25, 2009.

2. L. Khine, M. Palaniapan, L.C. Shao, C.L. Wong, and W.K. Wong, "Temperature compensation of MEMS oscillator composed of two adjoining square and beam resonators," *22nd European Conference on Solid-State Transducers (Eurosensors XXII)*, Dresden, Germany, Sept. 7-10, 2008, pp. 1345-1348.

3. L.C. Shao, C.L. Wong, L. Khine, M. Palaniapan, and W.K. Wong, "Study of various characterization techniques for MEMS devices," *22nd European Conference on Solid-State Transducers (Eurosensors XXII)*, Dresden, Germany, Sept. 7-10, 2008, pp. 1470-1473.

4. C.L. Wong, L.C. Shao, L. Khine, M. Palaniapan, and W.K. Wong, "Novel acoustic phonon detection technique to determine temperature coefficient of frequency in MEMS resonators," *22nd European Conference on Solid-State Transducers (Eurosensors XXII)*, Dresden, Germany, Sept. 7-10, 2008, pp. 429-432.

5. T. Niu, M. Palaniapan, L. Khine, and L.C. Shao, "MEMS oscillators using bulk-mode resonators," *22nd European Conference on Solid-State Transducers (Eurosensors XXII)*, Dresden, Germany, Sept. 7-10, 2008, pp. 197-200.

6. L. Khine, M. Palaniapan, L. Shao, and W.K. Wong, "Characterization of SOI Lamé-mode square resonators," *IEEE Inter. Frequency Control Symposium*, May 19-21, 2008, pp. 625-628.

7. L.C. Shao, M. Palaniapan, L. Khine, and W.W. Tan, "Nonlinear behavior of Lamé-mode SOI bulk resonator," *IEEE Inter. Frequency Control Symposium*, May 19-21, 2008, pp. 646-650.

8. L. Khine, M. Palaniapan, and W.K. Wong, "6MHz bulk-mode resonator with Q values exceeding one million," *14th International Conference on Solid-State Sensors, Actuators and Microsystems (Transducers'07 / Eurosensors XXI)*, Lyon, France, June 10-14, 2007, pp. 2445-2448.

9. L. Khine, M. Palaniapan, and W.K. Wong, "12.9MHz Lamé-mode differential SOI bulk resonators," *14th International Conference on Solid-State Sensors, Actuators and Microsystems (Transducers'07 / Eurosensors XXI)*, Lyon, France, June 10-14, 2007, pp. 1753-1756.

10. M. Palaniapan and L. Khine, "Nonlinear behavior of SOI Free-Free micromechanical beam resonator," *20th European Conference on Solid-State Transducers (Eurosensors XX)*, Göteborg, Sweden, Sept. 17-20, 2006.

11. L. Khine and M. Palaniapan, "Behavioural modelling and system-level simulation of micromechanical beam resonators," *Journal of Physics: Conference Series 34, International MEMS Conference 2006*, May 9-12, 2006, pp. 1053-1058.